LA-11721-T
Thesis

UC-414
Issued: January 1990

LA--11721-T

DE90 005833

A Search for $\bar{\nu}_e$ Appearance from Stopped π^+ and μ^+ Decay at LAMPF

*Brian Kurt Fujikawa**

---

*Guest Scientist at Los Alamos. Department of Physics, California Institute of Technology, Pasadena, CA 91125

MASTER

DISTRIBUTION OF THIS DOCUMENT IS UNLIMITED

Los Alamos
Los Alamos National Laboratory
Los Alamos, New Mexico 87545

Acknowledgments

The search for $\bar{\nu}_e$ appearance was performed by the members of the E645 collaboration with the assistance of the technical staff at LAMPF. They deserve my appreciation for making this experiment possible. Special thanks goes to Bob McKeown and Stuart Freedman for many useful discussions. I would also like to thank the students, staff, and faculty at Kellogg for their support during my stay at CalTech.

I would like to thank all of my teachers, past and present, for the education they have given me. I am especially grateful to my advisor, Bob McKeown, for his friendship, support, and guidance.

Abstract

We report on a recent search for $\bar{\nu}_e$ appearance from stopped $\pi^+ \rightarrow \mu^+\nu_\mu$ and $\mu^+ \rightarrow e^+\nu_e\bar{\nu}_\mu$ decay made by the LAMPF experiment E645. The appearance of $\bar{\nu}_e$ may occur from $\bar{\nu}_\mu \rightarrow \bar{\nu}_e$, $\nu_e \rightarrow \bar{\nu}_{eL}$, or $\nu_\mu \rightarrow \bar{\nu}_{eL}$ oscillations. Appearance may also occur from rare $\mu^+ \rightarrow e^+\bar{\nu}_e\nu_\mu$ decay, which is allowed by a multiplicative lepton charge conservation law. The neutrino energies range from $E_\nu = 0$ to 52.8MeV. The neutrino detector, which is located 26.1 meters from the neutrino source, consists of a segmented liquid scintillator and proportional drift tube central detector surrounded by both active and passive shielding. The central detector detects $\bar{\nu}_e$ through the $\bar{\nu}_e$p $\rightarrow$ ne$^+$ Charge Current (CC) reaction, which is signaled by the direct detection of the final state positron and neutron. The hydrogen-rich liquid scintillators act as free proton targets for the $\bar{\nu}_e$p CC reaction. The neutrons are detected through radiative neutron capture on gadolinium. We find no evidence for $\bar{\nu}_e$ appearance in the first year of running. New limits on the $\bar{\nu}_\mu, \nu_e, \nu_\mu \rightarrow \bar{\nu}_e$ oscillation parameters and the rare $\mu^+ \rightarrow e^+\bar{\nu}_e\nu_\mu$ decay branching ratio are presented.

Contents

List of Figures

List of Tables

Chapter 1

Introduction

We report on a recent search for neutrino oscillations and the rare $\mu^+ \rightarrow e^+\bar{\nu}_e\bar{\nu}_\mu$ decay performed at the Los Alamos Meson Physics Facility (LAMPF). The experiment, LAMPF E645, is a collaboration between Argonne National Laboratory, California Institute of Technology, Lawrence Berkeley Laboratory, Los Alamos Meson Physics Facility, Louisiana State University, and the Ohio State University [1]. The E645 neutrino detector is located in a low background environment 26.1m from the LAMPF A-6 beam stop where the neutrinos, ν_μ, ν_e, and $\bar{\nu}_\mu$, are copiously produced in equal admixture from stopped $\pi^+ \rightarrow \mu^+\nu_\mu$ and $\mu^+ \rightarrow e^+\nu_e\bar{\nu}_\mu$ decay. These neutrinos are isotropically distributed and have energies in the range $E_\nu = 0$ to 52.8MeV. The 20 tons of material in the detector provide an abundant source of targets for both Charged-Current (CC) and Neutral-Current (NC) neutrino reactions, which may be identified through the direct detection of the final state particles. The detector has the capability of detecting medium energy (15-100 MeV) electrons (both e^+ and e^-), which makes the detector sensitive to $\bar{\nu}_e$ through the CC $\bar{\nu}_e$ reaction on the proton

$$\bar{\nu}_e + \mathrm{p} \rightarrow \mathrm{n} + e^+ \tag{1.1}$$

where the targets are free protons in the form of hydrogen. Because the neutrino beam contains ν_μ, ν_e, and $\bar{\nu}_\mu$, but very little $\bar{\nu}_e$, a positive $\bar{\nu}_e$ signal would indicate possible $\bar{\nu}_\mu \rightarrow \bar{\nu}_e$ oscillations, $\nu_e \rightarrow \bar{\nu}_{eL}$ oscillations, $\nu_\mu \rightarrow \bar{\nu}_{eL}$ oscillations, or rare $\mu^+ \rightarrow e^+\bar{\nu}_e\bar{\nu}_\mu$ decay. Active and passive shielding suppresses both cosmic ray and non-neutrino beam associated backgrounds to the reaction 1.1. Backgrounds are further suppressed by the particle identification capabilities of the neutrino detector. Unfortunately the detector is not capable of identifying e^+ from e^-, and neutrino backgrounds to the $\bar{\nu}_e$ signal will be introduced from the CC ν_e reactions on the bound neutron:

$$\nu_e + \mathrm{n} \rightarrow \mathrm{p} + \mathrm{e}^- \tag{1.2}$$

and from neutrino-electron elastic scattering:

$$\begin{aligned} \nu_\mu + e^- &\rightarrow \nu_\mu + e^- \\ \nu_e + e^- &\rightarrow \nu_e + e^- \\ \bar{\nu}_\mu + e^- &\rightarrow \bar{\nu}_\mu + e^- \end{aligned} \tag{1.3}$$

To suppress this neutrino background, the detector contains small amounts of gadolinium, which makes the detector sensitive to low energy (thermal - 10 MeV) neutrons. This is signaled by the detection of the gamma rays from neutron radiative capture on gadolinium. The detection of both the positron and the neutron in coincidence provides a clean signature for the $\bar{\nu}_e$ detection reaction 1.1 over a background of ν_μ, ν_e, and $\bar{\nu}_\mu$ induced events.

This report is organized as follows. Chapter 2 discusses the physics of neutrino oscillations. Chapter 3 describes the neutrino source, the neutrino detector, and the data acquisition system. Chapter 4 describes the software tools used for the offline data analysis and Chapter 5 describes the analysis of the 1987 data. Chapter 6 discusses the results of this analysis. Chapter 7 concludes this report with a summary.

Chapter 2

Physics

2.1 Standard Electroweak Theory

We present the elements of the Standard Electroweak Theory of Glashow [2], Weinberg [3], and Salam [4], which are relevant to the phenomena of neutrino oscillations. This discussion is based primarily on Commins and Bucksbaum [5].

The six known leptons (e^-, ν_e, μ^-, ν_μ, τ^-, and ν_τ) appear to fall naturally into three generations

$$\Psi_e = \begin{pmatrix} \nu_e \\ e^- \end{pmatrix} \quad \Psi_\mu = \begin{pmatrix} \nu_\mu \\ \mu^- \end{pmatrix} \quad \Psi_\tau = \begin{pmatrix} \nu_\tau \\ \tau^- \end{pmatrix} \tag{2.1}$$

Each lepton generation: Ψ_e, Ψ_μ, and Ψ_e, is associated with a respective lepton charge: L_e, L_μ, and L_τ. The lepton charges have values given in Table 2.1. Experiments are consistent with a law of lepton charge conservation, which reads

$$\begin{aligned} \sum_i L_e^i &= \text{const}, \\ \sum_i L_\mu^i &= \text{const}, \\ \sum_i L_\tau^i &= \text{const}. \end{aligned} \tag{2.2}$$

The electron lepton charge L_e, the muon lepton charge L_μ, and the tauon lepton charge L_τ are separately conserved in all processes. An alternative multiplicative

Particle	L_e	L_μ	L_τ
e^-,ν_e	1	0	0
μ^-,ν_μ	0	1	0
τ^-,ν_τ	0	0	1
other particles	0	0	0

Table 2.1: The lepton charges. The anti-leptons (e^+, $\bar{\nu}_e$, μ^+, $\bar{\nu}_\mu$, τ^+, and $\bar{\nu}_\tau$) have opposite charges.

law is discussed below. The law of lepton charge conservation was introduced to explain the absence of neutrinoless $\mu^\pm \rightleftharpoons e^\pm$ transitions such as $\mu^+ \to e^+\gamma$. The experimental upper limit on the branching ratio of the muon decay $\mu^+ \to e^+\gamma$ is [6]

$$\frac{\Gamma(\mu^+ \to e^+\gamma)}{\Gamma(\mu^+ \to \text{all})} < 4.9 \times 10^{-11} \tag{2.3}$$

This decay does not violate charge conservation, is allowed kinematically, and requires some form of lepton charge conservation law in order to be suppressed.

In the Standard Electroweak Theory, massless gauge fields arise from the requirement of local gauge invariance to transformations under the group SU(2) × U(1). Experiments are consistent with the V-A hypothesis that only the left-handed components of the lepton field participate in weak charged currents. Therefore the leptons couple to the gauge fields as left-handed SU(2) isodoublets: Ψ_{eL}, $\Psi_{\mu L}$, and $\Psi_{\tau L}$; and right-handed SU(2) isosinglets: e_R, ν_{eR}, μ_R, $\nu_{\mu R}$, τ_R, and $\nu_{\tau R}$. The SU(2) × U(1) symmetry is spontaneously broken by the Higgs mechanism, which gives masses to the gauge fields. This results in the massive charged vector fields W_μ^+ and W_μ^-, which are interpreted as the mediator of weak charged current interactions, the massive neutral vector field Z_μ^0, which is interpreted as the mediator of weak neutral current interactions, and the massless neutral vector field A_μ, which is interpreted as the photon – the mediator of electromagnetic interactions.

Lepton masses are generated through the coupling of the lepton field to a SU(2) isodoublet of scalar fields Φ

$$\Phi = \begin{pmatrix} \phi^{+} \\ \phi^{0} \end{pmatrix} \tag{2.4}$$

Note that in the unitary gauge,

$$\Phi = \begin{pmatrix} 0 \\ v + \frac{H(x)}{\sqrt{2}} \end{pmatrix} \simeq \begin{pmatrix} 0 \\ v \end{pmatrix} \tag{2.5}$$

where v is the vacuum state and $H(x)$ is the massive Higgs field. In order to be invariant under SU(2) × U(1), the lepton-scalar field coupling must have one of the following forms:

$$\mathcal{L}_s^{(l)} = g_{ll'}(\bar{\Psi}_{lL}\Phi l'_R + \bar{l}'_R\Phi^\dagger\Psi_{lL}) \tag{2.6}$$

and

$$\mathcal{L}_s^{(\nu_l)} = h_{ll'}(\bar{\Psi}_{lL}\tilde{\Phi}\nu_{l'R} + \bar{\nu}_{l'R}\tilde{\Phi}^\dagger\Psi_{lL}) \tag{2.7}$$

where $l, l' = e, \mu, \tau$; $g_{ll'}$ and $h_{ll'}$ are real coupling constants; and

$$\tilde{\Phi} = (-i\Phi^\dagger\tau_2)^T = \begin{pmatrix} \phi^{0\dagger} \\ -\phi^{+\dagger} \end{pmatrix} \tag{2.8}$$

The lepton-scalar field couplings of the type given in Equation 2.6 generate the masses of the charged leptons and couplings of the type given in Equation 2.7 generate the neutrino masses.

For two lepton generations: Ψ_e and Ψ_μ, the lepton-scalar coupling, i.e., the lepton mass contribution to the Lagrangian is equal to

$$\begin{aligned}\mathcal{L}_m = {} & g_{ee}(\bar{\Psi}_{eL}\Phi e_R + \bar{e}_R\Phi^\dagger\Psi_{eL}) + g_{e\mu}(\bar{\Psi}_{eL}\Phi\mu_R + \bar{e}_R\Phi^\dagger\Psi_{\mu L}) + \\ & g_{\mu e}(\bar{\Psi}_{\mu L}\Phi e_R + \bar{\mu}_R\Phi^\dagger\Psi_{eL}) + g_{\mu\mu}(\bar{\Psi}_{\mu L}\Phi\mu_R + \bar{\mu}_R\Phi^\dagger\Psi_{\mu L}) + \\ & h_{ee}(\bar{\Psi}_{eL}\tilde{\Phi}\nu_{eR} + \bar{\nu}_{eR}\tilde{\Phi}^\dagger\Psi_{eL}) + h_{e\mu}(\bar{\Psi}_{eL}\tilde{\Phi}\nu_{\mu R} + \bar{\nu}_{eR}\tilde{\Phi}^\dagger\Psi_{\mu L}) + \\ & h_{\mu e}(\bar{\Psi}_{\mu L}\tilde{\Phi}\nu_{eR} + \bar{\nu}_{\mu R}\tilde{\Phi}^\dagger\Psi_{eL}) + h_{\mu\mu}(\bar{\Psi}_{\mu L}\tilde{\Phi}\nu_{\mu R} + \bar{\nu}_{\mu R}\tilde{\Phi}^\dagger\Psi_{\mu L})\end{aligned} \tag{2.9}$$

The eight coupling constants: g_{ee}, $g_{e\mu}$, $g_{\mu e}$, $g_{\mu\mu}$, h_{ee}, $h_{e\mu}$, $h_{\mu e}$, and $h_{\mu\mu}$ are not mutually independent. The leptonic Lagrangian is invariant to rotations of the form

$$\begin{pmatrix} E_L \\ M_L \end{pmatrix} \rightarrow \begin{pmatrix} \cos\theta_1 & -\sin\theta_1 \\ \sin\theta_1 & \cos\theta_1 \end{pmatrix} \begin{pmatrix} E_L \\ M_L \end{pmatrix} \tag{2.10}$$

$$\begin{pmatrix} e_R \\ \mu_R \end{pmatrix} \rightarrow \begin{pmatrix} \cos\theta_2 & -\sin\theta_2 \\ \sin\theta_2 & \cos\theta_2 \end{pmatrix} \begin{pmatrix} e_R \\ \mu_R \end{pmatrix} \tag{2.11}$$

$$\begin{pmatrix} \nu_{eR} \\ \nu_{\mu R} \end{pmatrix} \rightarrow \begin{pmatrix} \cos\theta_3 & -\sin\theta_3 \\ \sin\theta_3 & \cos\theta_3 \end{pmatrix} \begin{pmatrix} \nu_{eR} \\ \nu_{\mu R} \end{pmatrix} \tag{2.12}$$

Thus, we are free to choose θ_1, θ_2, and θ_3 so that $g_{e\mu} = g_{\mu e} = 0$ and $h_{e\mu} = h_{\mu e}$. Note that the choice of $g_{e\mu} = g_{\mu e} = 0$ is equivalent to the assumption that the charged lepton states that participate in weak interactions are also mass eigenstates. Therefore the lepton mass portion of the Lagrangian for two lepton generations in the unitary gauge is equal to

$$\begin{aligned} \mathcal{L}_m =& v[g_{ee}\bar{e}e + g_{\mu\mu}\bar{\mu}\mu + h_{ee}\bar{\nu}_e\nu_e + h_{\mu\mu}\bar{\nu}_\mu\nu_\mu + h_{e\mu}(\bar{\nu}_e\nu_\mu + \bar{\nu}_\mu\nu_e)] \\ =& m_e\bar{e}e + m_\mu\bar{\mu}\mu + m_{\nu_e}\bar{\nu}_e\nu_e + m_{\nu_\mu}\bar{\nu}_\mu\nu_\mu + m_{\nu_e\nu_\mu}(\bar{\nu}_e\nu_\mu + \bar{\nu}_\mu\nu_e) \end{aligned} \tag{2.13}$$

where $\bar{l}l = \bar{l}_L l_R + \bar{l}_R l_L$ and $\bar{\nu}_l\nu_l = \bar{\nu}_{lL}\nu_{lR} + \bar{\nu}_{lR}\nu_{lL}$. Equation 2.13 is analogous to the quark mass portion of the Lagrangian in the *Glashow-Iliopoulos-Maiani* (GIM) model [11]. Equation 2.13 contains terms proportional to $\bar{\nu}_\mu\nu_e$ and $\bar{\nu}_e\nu_\mu$ that violate the lepton charge conservation law. However, the lepton mass Lagrangian does not contain total lepton charge changing (majorana) terms of the form $\bar{\nu}_l^c\nu_l$ and $\bar{\nu}_l^c\nu_l$ (the superscript "c" designates a charge conjugate state). Therefore the Lagrangian is capable of describing ΔL = 0 (total lepton charge L is conserved) lepton flavor changing phenomena such as neutrino oscillations.

In the minimal Standard Electroweak Theory, all neutrinos are massless and the lepton mass portion of the Lagrangian is equal to

$$\mathcal{L}_m = m_e\bar{e}e + m_\mu\bar{\mu}\mu \tag{2.14}$$

where lepton charge is conserved. Therefore, the Lagrangian in the minimal Standard Electroweak Theory is consistent with the law of additive lepton charge conservation.

The minimal Standard Electroweak Theory is highly successful in describing all electroweak phenomena. There are no uncontroversial experimental results that are inconsistent with this theory. However, massive neutrinos and neutrino mixing have not been ruled out by experiments. Neutrino oscillation experiments provide a test of the Standard Electroweak Theory in the minimal form.

2.2 Neutrino Oscillations

Neutrino oscillations of the type $\nu_L \rightleftharpoons \bar{\nu}_L$ was first introduced by Pontecorvo [7]. The mixing of neutrino flavors were first introduced by Maki, Nakagawa, and Sakata [8] and Nakagawa, *et al.* [9]. Flavor oscillations of the type $\nu_e \rightleftharpoons \nu_\mu$ were later discussed by Pontecorvo [10].

We discuss the phenomena of neutrino oscillations. This discussion is based, initially, upon the above discussion of the Standard Electroweak Theory. We also follow the works of Boehm and Vogel [18] and of Bilenky and Petcov [19].

For simplicity, we shall restrict this discussion on neutrino oscillations to two lepton generations: Ψ_e and Ψ_μ. The lepton mass portion of the Lagrangian given in Equation 2.13 is capable of describing $\Delta \mathrm{L} = 0$ lepton flavor changing phenomena such as neutrino oscillations. For convenience, we shall express the neutrino mass portion of the Lagrangian from Equation 2.13 in matrix format

$$\mathcal{L}_m^{(\nu)} = \begin{pmatrix} \bar{\nu}_e & \bar{\nu}_\mu \end{pmatrix} \begin{pmatrix} m_{\nu_e} & m_{\nu_e\nu_\mu} \\ m_{\nu_e\nu_\mu} & m_{\nu_\mu} \end{pmatrix} \begin{pmatrix} \nu_e \\ \nu_\mu \end{pmatrix} \tag{2.15}$$

The neutrino mass matrix is symmetric and may be diagonalized. We introduce a new basis (ν_1, ν_2) with

$$\begin{pmatrix} \nu_e \\ \nu_\mu \end{pmatrix} = \begin{pmatrix} \cos\theta & \sin\theta \\ -\sin\theta & \cos\theta \end{pmatrix} \begin{pmatrix} \nu_1 \\ \nu_2 \end{pmatrix} \tag{2.16}$$

where

$$\tan 2\theta = \frac{2m_{\nu_e\nu_\mu}}{m_{\nu_\mu} - m_{\nu_e}} \tag{2.17}$$

In this new basis,

$$\mathcal{L}_m^{(\nu)} = \begin{pmatrix} \bar{\nu}_1 & \bar{\nu}_2 \end{pmatrix} \begin{pmatrix} m_1 & 0 \\ 0 & m_2 \end{pmatrix} \begin{pmatrix} \nu_1 \\ \nu_2 \end{pmatrix} \tag{2.18}$$

The states ν_1 and ν_2 are mass eigenstates with masses m_1 and m_2, respectively.

In an ideal neutrino oscillation experiment, we are provided with a neutrino beam of known flux, which consists exclusively of ν_μ with no ν_e. For example, such a neutrino beam could be produced from in-flight $\pi^+ \rightarrow \mu^+\nu_\mu$ decay. This beam is monitored by a detector located L meters from the neutrino source. It has been shown experimentally that this detector will observe mostly μ^- through the $\nu_\mu n \rightarrow p\mu^-$ reaction [12]. There are two classes of experiments that may be performed by this detector. The first, an appearance experiment, searches for the production of e^- instead of the expected μ^- in the detector. The second is the disappearance experiment where the measured μ^- production rate is compared to a prediction. The appearance experiment measures the probability $P(\nu_\mu \rightarrow \nu_e)$, whereas the disappearance experiment measures the probability $P(\nu_\mu \rightarrow \nu_\mu)$. Because we are considering only two lepton generations

$$P(\nu_\mu \rightarrow \nu_\mu) + P(\nu_\mu \rightarrow \nu_e) = 1 \tag{2.19}$$

The oscillation probability, $P(\nu_\mu \rightarrow \nu_e)$, may be expressed in terms of the mixing angle θ, the neutrino masses m_1 and m_2, the neutrino energy E_ν, and the distance L from the neutrino source to the detector. A time $t = 0$, the neutrino state $|\nu>$ is pure ν_μ

$$|\nu(t=0)>=|\nu_\mu>= -\sin\theta|\nu_1> + \cos\theta|\nu_2> \tag{2.20}$$

This neutrino state evolves with time as

$$|\nu(t)>= -\sin\theta e^{-iE_1t}|\nu_1> + \cos\theta e^{-iE_2t}|\nu_2> \tag{2.21}$$

where we have used the natural units ($\hbar = c = 1$). The oscillation probability at the detector is equal to

$$P(\nu_\mu \rightarrow \nu_e) = | < \nu_e | \nu(t = L) > |^2 = \sin^2(2\theta) \sin^2(\frac{1}{2}(E_2 - E_1)L) \tag{2.22}$$

For small neutrino masses $m_1 \ll E_\nu$ and $m_2 \ll E_\nu$,

$$\frac{1}{2}(E_2 - E_1)L \simeq 1.27 \frac{\delta m^2 L}{E_\nu} \tag{2.23}$$

where $\delta m^2 \equiv m_2^2 - m_1^2$ is in eV^2, L is in meters, and E_ν is in MeV. Therefore, the oscillation probability is equal to

$$P(\nu_\mu \rightarrow \nu_e) = \sin^2(2\theta) \sin^2(1.27 \frac{\delta m^2 L}{E_\nu}) \tag{2.24}$$

Note that in the minimal Standard Electroweak Theory all neutrinos are massless and $P(\nu_\mu \rightarrow \nu_e) = 0$.

The lepton mass term of the Lagrangian in Equation 2.13 is invariant under CP (Charge·Parity). While this is generally true for two lepton generations, this is not true for three lepton families where, in analogy to quark mixing in the Kobayashi-Maskawa model [14], the mass portion of the Lagrangian contains a CP violating phase. CP invariance implies that

$$P(\nu_\mu \rightarrow \nu_e) = P(\bar{\nu}_\mu \rightarrow \bar{\nu}_e) \tag{2.25}$$

In terms of the oscillation parameters,

$$\delta m^2_{\bar{\mu}\bar{e}} = \delta m^2_{\mu e} \tag{2.26}$$

$$sin^2(2\theta_{\bar{\mu}\bar{e}}) = \sin^2(2\theta_{\mu e}) \tag{2.27}$$

where the subscript "μe" represents the $\nu_\mu \rightarrow \nu_e$ oscillation parameters and the subscript "$\bar{\mu}\bar{e}$" represents the $\bar{\nu}_\mu \rightarrow \bar{\nu}_e$ oscillation parameters.

The lepton mass portion of the Lagrangian in Equation 2.13 may be generalized to include majorana terms $\bar{\nu}_{l'} \nu_l^c$ and $\bar{\nu}_{l'}^c \nu_l$, which in addition to changing lepton flavor, change the total lepton charge by two ($\Delta L = 2$). Such terms may arise in extended SU(2) × U(1) theories with several Higgs doublets [20] or with a Higgs triplet. This provides the phenomenological basis for $\Delta L = 2$ oscillations such as $\nu_\mu \to \bar{\nu}_{eL}$. The $\nu_\mu \to \bar{\nu}_{eL}$ oscillation probability, in analogy with Equation 2.24, is equal to

$$P(\nu_\mu \to \bar{\nu}_{eL}) = \sin^2(2\theta_{\mu\bar{e}})\sin^2(1.27\frac{\delta m^2_{\mu\bar{e}}L}{E_\nu}) \tag{2.28}$$

(the subscript "$\mu\bar{e}$" designates $\nu_\mu \to \bar{\nu}_{eL}$ oscillations). A disappearance experiment will measure

$$P(\nu_\mu \to \nu_\mu) = 1 - \sin^2(2\theta_{\mu\bar{e}})\sin^2(1.27\frac{\delta m^2_{\mu\bar{e}}L}{E_\nu}) \tag{2.29}$$

However, because the $\bar{\nu}_{eL}$ ("wrong" helicity anti-neutrino) is sterile to V-A (left-handed) charged current interactions, an appearance experiment would observe a shortage of e^+, even if $\nu_\mu \to \bar{\nu}_{eL}$ oscillations do in fact occur. In the absence of V+A (right-handed) charged currents, an appearance experiment will measure approximately [15]

$$(\frac{m_\nu}{E_\nu})^2 P(\nu_\mu \to \bar{\nu}_{eL}) = (\frac{m_\nu}{E_\nu})^2 \sin^2(2\theta_{\mu\bar{e}})\sin^2(1.27\frac{\delta m^2_{\mu\bar{e}}L}{E_\nu}) \tag{2.30}$$

where m_ν is a characteristic neutrino rest mass. At LAMPF neutrino energies ($\bar{\mathrm{E}}_\nu \sim 30\mathrm{MeV}$), the helicity suppression factor is $(\frac{\mathrm{m}_\nu}{\mathrm{E}_\nu})^2 < 3 \times 10^{-13}$ if $\mathrm{m}_\nu < 18\mathrm{eV}$ (upper limit on ν_e rest mass [16]) and $(\frac{\mathrm{m}_\nu}{\mathrm{E}_\nu})^2 < 7 \times 10^{-5}$ if $\mathrm{m}_\nu < 0.25\mathrm{MeV}$ (upper limit on ν_μ rest mass [17]).

In order for an appearance experiment to observe $\Delta L = 2$ oscillations at a level higher than $(\frac{\mathrm{m}_\nu}{\mathrm{E}_\nu})^2$, it is necessary to have some V+A charged current interactions. We define the parameter α^2 to be the ratio of the V+A $\bar{\nu}_e$p CC cross section $\sigma(\bar{\nu}_{eL}\mathrm{p})$ to the V-A $\bar{\nu}_e$p CC cross section $\sigma(\bar{\nu}_{eR}\mathrm{p})$,

$$\alpha^2 = \frac{\sigma(\bar{\nu}_{eL}\mathrm{p})}{\sigma(\bar{\nu}_{eR}\mathrm{p})} \tag{2.31}$$

In the presence of V+A charge currents, the appearance experiment will measure

$$\alpha^2 P(\nu_\mu \to \bar{\nu}_{eL}) = \alpha^2 \sin^2(2\theta_{\mu\bar{e}})\sin^2(1.27\frac{\delta m^2_{\mu\bar{e}}L}{E_\nu}) \tag{2.32}$$

V+A charge currents may arise in a left-right $\mathrm{SU(2)_L \times SU(2)_R \times U(1)}$ model where the V-A charge currents are mediated by massive left-handed vector bosons $\mathrm{W_L^\pm}$ and the V+A charged currents are mediated by massive right-handed vector bosons $\mathrm{W_R^\pm}$. The effective Langrangian [21] is equal to

$$-\mathcal{L}_{eff} = \frac{g}{2\sqrt{2}}[(V-A)W_L + (V+A)W_R] \tag{2.33}$$

where $\mathrm{W_L}$ and $\mathrm{W_R}$ are related to the mass eigenstates $\mathrm{W_1}$ and $\mathrm{W_2}$ (masses $\mathrm{M_1}$ and $\mathrm{M_2}$) by

$$W_1 = W_L \cos\zeta - W_R \sin\zeta \tag{2.34}$$

$$W_2 = W_L \sin\zeta + W_R \cos\zeta \tag{2.35}$$

and ζ is a mixing angle. In this model the parameter α, for small momentum transfers $\mathrm{q^2 \ll M_1^2, M_2^2}$, is equal to

$$\alpha \simeq \eta + \lambda \tag{2.36}$$

where $\eta = -\tan\zeta$ and $\lambda = (\frac{M_1}{M_2})$. Note that for pure V-A ($\zeta = 0$ and $\mathrm{M_2} \rightarrow \infty$), $\alpha = 0$. Muon decay experiments [22] constrain the V+A parameters ζ and λ to

$$-0.056 < \zeta < 0.040 \tag{2.37}$$

and

$$\lambda < 0.041 \tag{2.38}$$

at 90% confidence level. From these limits, α^2 may be as large as $\alpha^2 = 3 \times 10^{-3}$. However, it should be noted that in the case of $\nu_e \rightarrow \bar{\nu}_{eL}$ oscillations, neutrinoless double beta decay experiments [23,24] constrain the parameters, for a single neutrino field, $\alpha^2 \sin^2(2\theta_{e\bar{e}})$ to

$$\alpha^2 \sin^2(2\theta_{e\bar{e}}) < 3.6 \times 10^{-11} \tag{2.39}$$

at the 68% confidence level.

An alternative mechanism for a non-zero V+A parameter α^2 is through majoron neutrino couplings, where the majoron is a Nambu-Goldstone boson that results from symmetry breaking in the Higgs triplet model [25,26,27]. Strong limits on majoron coupling have been obtained from neutrinoless double beta decay experiments [23,24,28] that give the following constraint

$$\alpha^2 \sin^2(2\theta_{e\bar{e}}) < 5 \times 10^{-7} \tag{2.40}$$

in the case of majoron coupling to electron neutrinos. Less stringent, but mixing angle independent constraints have been obtained from e, μ universality in leptonic K decays [29] with

$$\alpha^2 < 4.5 \times 10^{-5} \tag{2.41}$$

It should be noted that majoron couplings to other neutrino families may be different.

Other phenomenological mechanisms for generating a non-zero V+A parameter α^2 are mentioned elsewhere [77].

2.3 Lepton Charge Conservation

Historically, lepton charge conservation laws were introduced to explain the absence of neutrinoless $\mu^\pm \rightleftharpoons e^\pm$ transitions. The additive law of lepton charge conservation, which is given in Equation 2.2, is present in the minimal Standard Electroweak Theory. An alternative form of lepton charge conservation is the multiplicative law of lepton charge conservation [30]. For two lepton generations, the multiplicative law requires that

$$\sum_i L_e^i + \sum_i L_\mu^i = \text{const.} \tag{2.42}$$

and

$$\prod_i (-1)^{L_\mu^i} = \text{const.} \tag{2.43}$$

in all processes. The relation of the multiplicative law to gauge theories is discussed elsewhere [31]. The additive law and the multiplicative law have equal consequences for processes that involve two leptons. Neutrinoless muon decay modes such as

$$\mu^+ \rightarrow e^+ + \gamma \tag{2.44}$$

violate both the additive law and the multiplicative law; where experimentally [6]

$$\frac{\Gamma(\mu^+ \rightarrow e^+\gamma)}{\Gamma(\mu^+ \rightarrow \text{all})} < 4.9 \times 10^{-11} \tag{2.45}$$

at 90% confidence level. However, the additive law and the multiplicative laws can have completely different consequences for interactions involving four leptons. Both laws allow the muon decay mode

$$\mu^+ \rightarrow e^+ + \nu_e + \bar{\nu}_\mu \tag{2.46}$$

that is observed experimentally [32]. However, the muon decay mode

$$\mu^+ \rightarrow e^+ + \bar{\nu}_e + \nu_\mu \tag{2.47}$$

and its inverse reaction

$$\bar{\nu}_\mu + e^- \rightarrow \mu^- + \bar{\nu}_e \tag{2.48}$$

are allowed by the multiplicative law, but are forbidden by the additive law. Experimental searches for the decay [32] $\mu^+ \rightarrow e^+\bar{\nu}_e\nu_\mu$ and the reaction [33] $\bar{\nu}_\mu e^- \rightarrow \mu^-\bar{\nu}_e$ have null results – in support of the additive law. The limits on the branching ratios obtained from these experiments are

$$\frac{\Gamma(\mu^+ \rightarrow e^+\bar{\nu}_e\nu_\mu)}{\Gamma(\mu^+ \rightarrow \text{all})} < 9 \times 10^{-2} \tag{2.49}$$

$$\frac{\Gamma(\bar{\nu}_\mu e^- \rightarrow \mu^-\bar{\nu}_e)}{\Gamma(\bar{\nu}_\mu e^- \rightarrow \text{all})} < 5 \times 10^{-2} \tag{2.50}$$

at 90% C.L. The multiplicative law does not predict the branching ratio of the muon decay $\mu^+ \rightarrow e^+\bar{\nu}_e\nu_\mu$. However, any finite branching ratio would support a multiplicative law.

2.4 LAMPF E645

The neutrino beam at LAMPF consists of medium energy ($E_\nu \leq 52.8$MeV) ν_μ, ν_e, and $\bar{\nu}_\mu$ from stopped $\pi^+ \rightarrow \mu^+\nu_\mu$ and $\mu^+ \rightarrow e^+\nu_e\bar{\nu}_\mu$ decay. The primary physics goal of LAMPF experiment E645 is to search for $\bar{\nu}_e$ appearance through the $\Delta L = 0$ flavor changing $\bar{\nu}_\mu \rightarrow \bar{\nu}_e$ oscillation mode; where we shall attempt to measure, or limit, the $\bar{\nu}_\mu \rightarrow \bar{\nu}_e$ oscillation parameters: $\sin^2(2\theta_{\bar{\mu}\bar{e}})$ and $\delta m^2_{\bar{\mu}\bar{e}}$.

The composition of the LAMPF neutrino beam provides us with the additional opportunity to investigate $\bar{\nu}_e$ appearance through the $\Delta L = 2$ $\nu_e \rightarrow \bar{\nu}_{eL}$ and $\nu_\mu \rightarrow \bar{\nu}_{eL}$ oscillation modes. Therefore, we shall attempt measure, or limit, the $\nu_e \rightarrow \bar{\nu}_{eL}$ oscillation parameters: $\alpha^2 \sin^2(2\theta_{e\bar{e}})$ and $\delta m^2_{e\bar{e}}$; and the $\nu_\mu \rightarrow \bar{\nu}_{eL}$ oscillation parameters: $\alpha^2 \sin^2(2\theta_{\mu\bar{e}})$ and $\delta m^2_{\mu\bar{e}}$.

We also have the opportunity to search for the rare muon decay mode $\mu^+ \rightarrow e^+\bar{\nu}_e\nu_\mu$, which is forbidden by the additive law of lepton charge conservation, but is allowed by the multiplicative law. Therefore, we shall attempt to measure, or limit, the branching ratio

$$R \equiv \frac{\Gamma(\mu^+ \rightarrow e^+\bar{\nu}_e\nu_\mu)}{\Gamma(\mu^+ \rightarrow \text{all})} \tag{2.51}$$

and test the additive law.

Chapter 3

The Experiment

3.1 LAMPF A-6 Neutrino Source

LAMPF produces a 780 MeV proton beam with a current of one mA. Approximately twenty percent of the beam intensity is used by production targets for other experiments. The remaining 800 μA of beam is degraded to 765 MeV and terminates at the A-6 beam stop, which is shown in Figure 3.1. The A-6 beam stop consists of multiple high purity, oxygen free, copper plates contained in a water cooled stainless steel jacket. The proton beam interacts with the copper nuclei in the beam stop, producing medium energy $(0 - 600\text{MeV})$ charged pions with an admixture of approximately 3.1 π^+ per π^- [34,35,36]. The pions quickly thermalize in the beam stop where they will either *decay in flight* (DIF), *decay at rest* (DAR), or be absorbed by the heavy beam stop material. Calculations made for the A-6 beam stop [37] show that only about 1.0% of the π^+ and π^- produced in the beam stop will decay in flight. Essentially all of the stopped π^+ decay; however almost none of the stopped π^- will decay. Upon stopping, the π^- are immediately bound to an atomic state of the copper nuclei by the attractive coulomb force, where the strongly interacting capture process completely dominates the weak decay process. Almost all stopped π^- are absorbed by the copper nuclei so that there are only

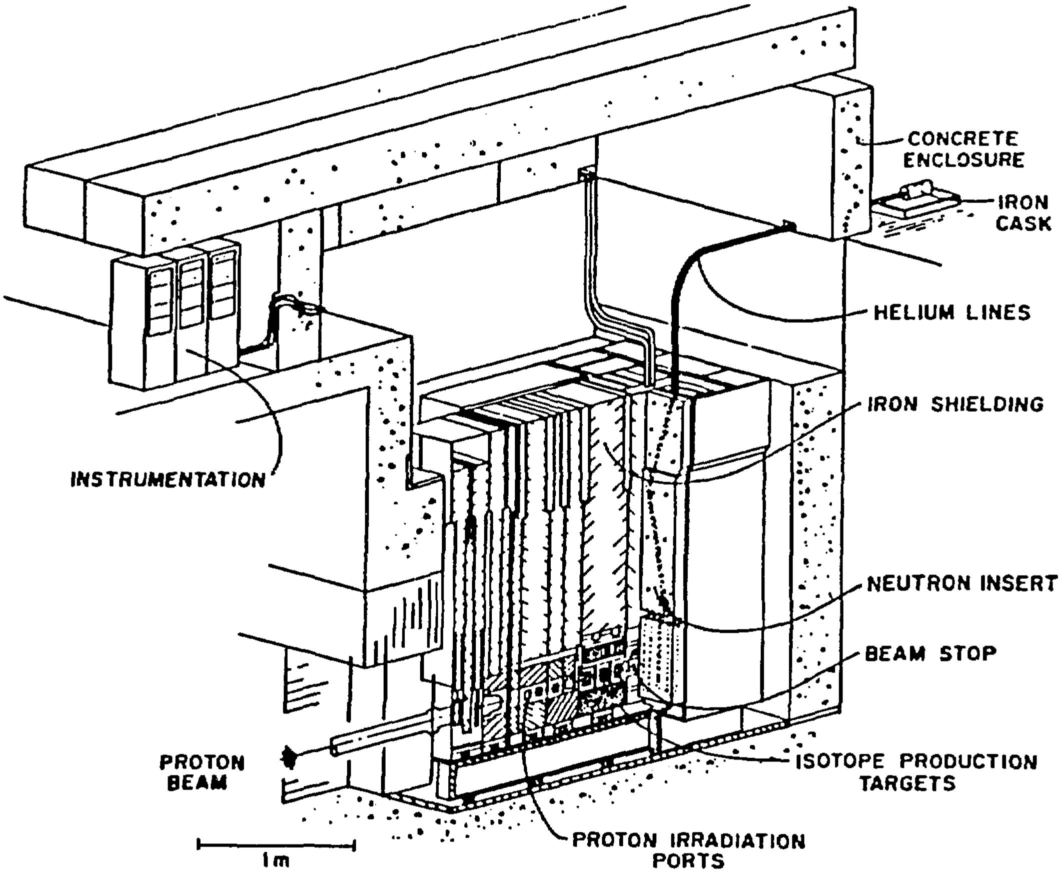

Figure 3.1: LAMPF A-6 Beam Stop.

3.2×10^{-3} π^- decays per π^+ decay.

The decay of the pions [1]

$$\pi^+ \rightarrow \mu^+ + \nu_\mu \tag{3.1}$$

$$\pi^- \rightarrow \mu^- + \bar{\nu}_\mu \tag{3.2}$$

and the subsequent decay of the resultant muons

$$\mu^+ \rightarrow e^+ + \nu_e + \bar{\nu}_\mu \tag{3.3}$$

$$\mu^- \rightarrow e^- + \bar{\nu}_e + \nu_\mu \tag{3.4}$$

drive the LAMPF A-6 neutrino source. Due to the relatively long muon lifetime, almost all muons (> 0.9999) from both DAR and DIF pions will stop. There is one μ^+ decay per π^+ decay. However, μ^- capture [2] competes with μ^- decay and only 7.4% of the μ^- will decay [38]; there are 2.4×10^{-4} μ^- decays per μ^+ decay. It is important that the relative intensity of the μ^- decay is small because this decay introduces a $\bar{\nu}_e$ contamination, which is an irreducible background to the $\bar{\nu}_e$ appearance experiment.

The neutrinos from the LAMPF A-6 beam stop and their relative intensities are given in Table 3.1. From the above discussion it is apparent that the neutrinos consist primarily of ν_μ, ν_e, and $\bar{\nu}_e$ from DAR π^+ and μ^+. The absolute number of neutrinos, N_{ν_μ}, N_{ν_e}, and $N_{\bar{\nu}_\mu}$, produced in the beam stop are given by

$$\left.\begin{array}{l} N_{\nu_\mu} \\ N_{\nu_e} \\ N_{\bar{\nu}_\mu} \end{array}\right\} = \frac{r_\pi \cdot Q}{1.602 \times 10^{-19}} \tag{3.5}$$

where r_π is the average number of π^+ decays per incident proton and Q is the proton charge in coulombs accumulated at the beam stop. Pion production cross sections for 730 MeV protons incident on various materials, including copper, have

---

[1] We ignore the $\pi^+ \rightarrow \nu_e e^+$ and $\pi^- \rightarrow \bar{\nu}_e e^-$ decay modes, which have very small branching ratios (1.2×10^{-4}) [39].

[2] The μ^- capture $\mu^- + \mathrm{Cu} \rightarrow X + \nu_\mu$ emits a ν_μ with an energy up to ~ 105MeV.

DAR Neutrinos

Neutrino	Source	Energy	Intensity
ν_μ	$\pi^+ \to \mu^+\nu_\mu$	27.8 MeV	1.0
ν_e	$\mu^+ \to e^+\nu_e\bar{\nu}_\mu$	0 – 52.8 MeV	1.0
$\bar{\nu}_\mu$	$\mu^+ \to e^+\nu_e\bar{\nu}_\mu$	0 – 52.8 MeV	1.0
ν_e	$\pi^+ \to e^+\nu_e$	69.8 MeV	1.2×10^{-4}

DIF and μ^- Capture Neutrinos

Neutrino	Source	Energy	Intensity
ν_μ	$\pi^+ \to \mu^+\nu_\mu$	10 – 275 MeV	1.0×10^{-2}
$\bar{\nu}_\mu$	$\pi^- \to \mu^-\bar{\nu}_\mu$	10 – 275 MeV	3.2×10^{-3}
ν_e	$\pi^+ \to e^+\nu_e$	20 – 550 MeV	1.2×10^{-6}
$\bar{\nu}_\mu$	$\mu^-\mathrm{Cu} \to X\nu_\mu$	0 – 105 MeV	3.0×10^{-3}

Contamination Neutrinos

Neutrino	Source	Energy	Intensity
$\bar{\nu}_e$	$\mu^- \to e^-\bar{\nu}_e\nu_\mu$	0 – 52.8 MeV	2.4×10^{-4}
$\bar{\nu}_e$	$\pi^- \to e^-\bar{\nu}_e$	20 – 550 MeV	4.0×10^{-7}

Exotic Neutrinos

Neutrino	Source	Energy	Intensity (90% C.L.)
$\bar{\nu}_e$	$\mu^+ \to e^+\bar{\nu}_e\nu_\mu$	0 – 52.8 MeV	$< 5.0 \times 10^{-2}$
$\bar{\nu}_e$	$\pi^+ \to \mu^+\bar{\nu}_e$	$\sim$ 27.8 MeV	$< 1.5 \times 10^{-3}$
$(\nu_e\ ,\ \bar{\nu}_e\ )$	$\pi^0 \to \nu_e\bar{\nu}_e$	20 – 625 MeV	$< 3.1 \times 10^{-6}$
$(\nu_\mu\ ,\ \bar{\nu}_\mu\ )$	$\pi^0 \to \nu_\mu\bar{\nu}_\mu$	20 – 625 MeV	$< 3.1 \times 10^{-6}$
$(\nu_\tau\ ,\ \bar{\nu}_\tau\ )$	$\pi^0 \to \nu_\tau\bar{\nu}_\tau$	20 – 625 MeV	$< 2.1 \times 10^{-6}$

Table 3.1: Tabulation of the neutrinos from the LAMPF A-6 beam stop. The intensities are relative to π^+ decay.

been measured [34]. A calculation, that extrapolates this measurement to 765 MeV protons incident on the beam stop, results in $r_\pi = 0.086 \pm 0.011$ [40]. The spatial distribution of these neutrinos is isotropic. The energy of the ν_μ from the two body π^+ decay is mono-energetic with $E_\nu = 27.8$MeV. The energy spectra of the ν_e and the $\bar{\nu}_\mu$ from μ^+ decay is predicted by the Standard Electroweak Theory [5], which gives the energy spectrum of the ν_e :

$$\frac{dN_{\nu_e}}{dE_\nu} = 12\frac{E_\nu^2}{E_{max}^3}\left(1 - \frac{E_\nu}{E_{max}}\right) \qquad 0 \leq E_\nu \leq E_{max} \qquad (3.6)$$

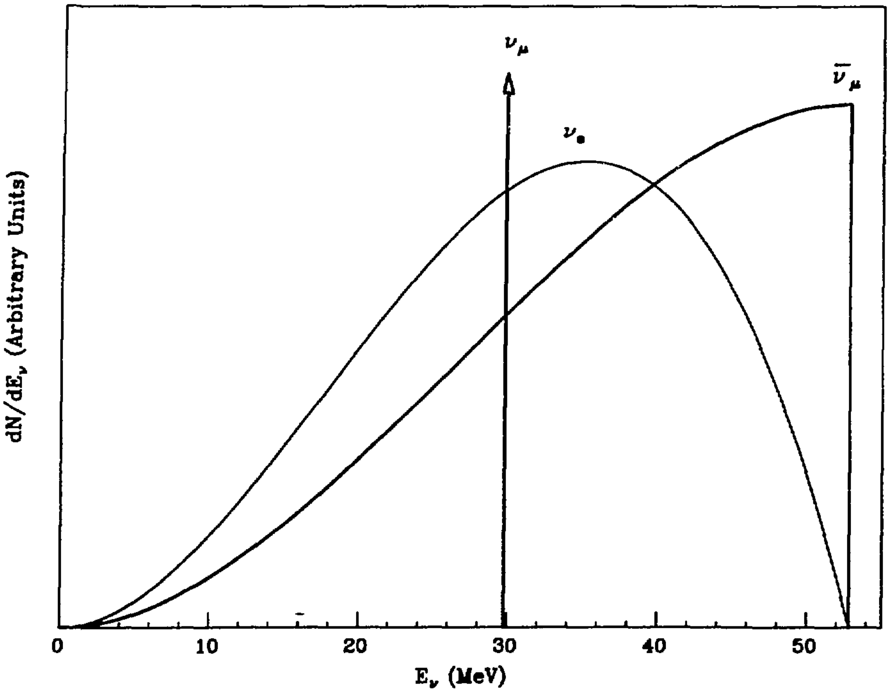

Figure 3.2: Neutrinos from the LAMPF A-6 beam stop. The mono-energetic ν_μ is from DAR $\pi^+ \rightarrow \mu^+\nu_\mu$ and the ν_e and $\bar{\nu}_\mu$ are from DAR $\mu^+ \rightarrow e^+\nu_e\bar{\nu}_\mu$.

and the $\bar{\nu}_\mu$:

$$\frac{dN_{\bar{\nu}_\mu}}{dE_\nu} = 2\frac{E_\nu^2}{E_{max}^3}\left(3 - 2\frac{E_\nu}{E_{max}}\right) \qquad 0 \leq E_\nu \leq E_{max} \tag{3.7}$$

where E_ν is the neutrino energy and $E_{max} = 52.8$MeV is the neutrino endpoint energy. The neutrino spectra from the LAMPF A-6 beam stop is shown in Figure 3.2.

Exotic neutrinos may also be produced in the A-6 beam stop from rare μ^+, π^+, and π^0 decay modes. The rare μ^+ decay mode $\mu^+ \rightarrow e^+\bar{\nu}_e\nu_\mu$ is forbidden by the additive lepton charge conservation law, but is allowed by a hypothetical multiplicative conservation law. The $\bar{\nu}_e$ from this decay has a similar energy spectrum to the energy spectrum of the $\bar{\nu}_e$ from possible $\bar{\nu}_\mu \rightarrow \bar{\nu}_e$ oscillations. Experimentally, the limit on the branching ratio for this decay is

$$\frac{\Gamma(\mu^+ \rightarrow e^+\bar{\nu}_e\nu_\mu)}{\Gamma(\mu^+ \rightarrow \text{all})} < 9.8 \times 10^{-2} \tag{3.8}$$

at 90% C.L. [41]. A more stringent limit of $< 5.0 \times 10^{-2}$ at 90% C.L. is obtained from limits on $\bar{\nu}_\mu e^- \rightarrow \mu^- \bar{\nu}_e$ [42]. This experiment is expected to be more sensitive and we shall consider neutrinos from the rare μ^+ decay mode $\mu^+ \rightarrow e^+ \bar{\nu}_e \nu_\mu$.

The rare π^+ decay mode $\pi^+ \rightarrow \mu^+ \bar{\nu}_e$ may proceed by majoron-neutrino coupling. The experimental branching ratio of this decay, $< 1.5 \times 10^{-3}$ at 90% C.L. [77], is below the sensitivity of this experiment. Therefore we shall disregard any contribution to the neutrino flux from the decay $\pi^+ \rightarrow \mu^+ \bar{\nu}_e$.

Along with the charged pions, neutral pions are copiously produced in the beam stop. The rare $\pi^0 \rightarrow 2\nu$ decay mode is allowed only if there exist neutrino states of both chiralities or if lepton charge is not conserved [43]. Neutrinos from possible $\pi^0 \rightarrow 2\nu$ decay are up to ten times more energetic than the neutrinos from DAR π^+ and μ^+. In addition, experimental limits on the branching ratios of these decays are very low:

$$\frac{\Gamma(\pi^0 \rightarrow \nu_e \bar{\nu}_e)}{\Gamma(\pi^0 \rightarrow \text{all})} < 3.1 \times 10^{-6} \tag{3.9}$$

$$\frac{\Gamma(\pi^0 \rightarrow \nu_\mu \bar{\nu}_\mu)}{\Gamma(\pi^0 \rightarrow \text{all})} < 3.1 \times 10^{-6} \tag{3.10}$$

$$\frac{\Gamma(\pi^0 \rightarrow \nu_\tau \bar{\nu}_\tau)}{\Gamma(\pi^0 \rightarrow \text{all})} < 2.1 \times 10^{-6} \tag{3.11}$$

at 90% C.L. [44]. Therefore we shall disregard any possible contribution to the neutrino flux from $\pi^0 \rightarrow 2\nu$.

3.2 $\bar{\nu}_e$ Detection

The neutrino detector, which is shown in Figure 3.3, consists of a modular central detector surrounded by a lead passive shield and a liquid scintillator active shield. The central detector is made up of 40 vertical modules, where each module consists of one plane of 45 horizontally oriented PDTs (proportional drift tubes), one plane of 45 vertically oriented PDTs, and one plane of 12 liquid scintillator panels. Each liquid scintillator plane is covered with mylar sheets coated with gadolinium-loaded

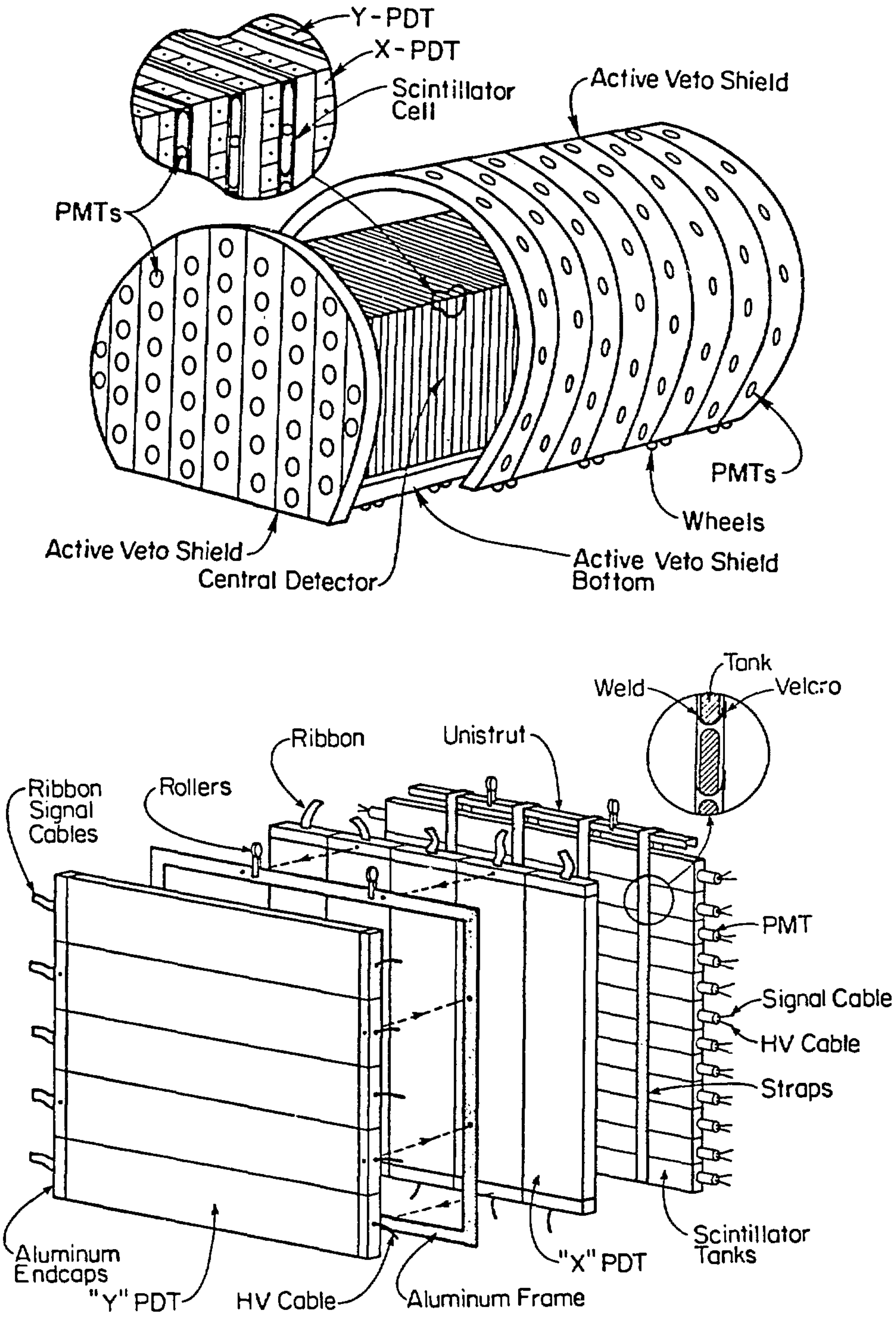

Figure 3.3: Neutrino Detector.

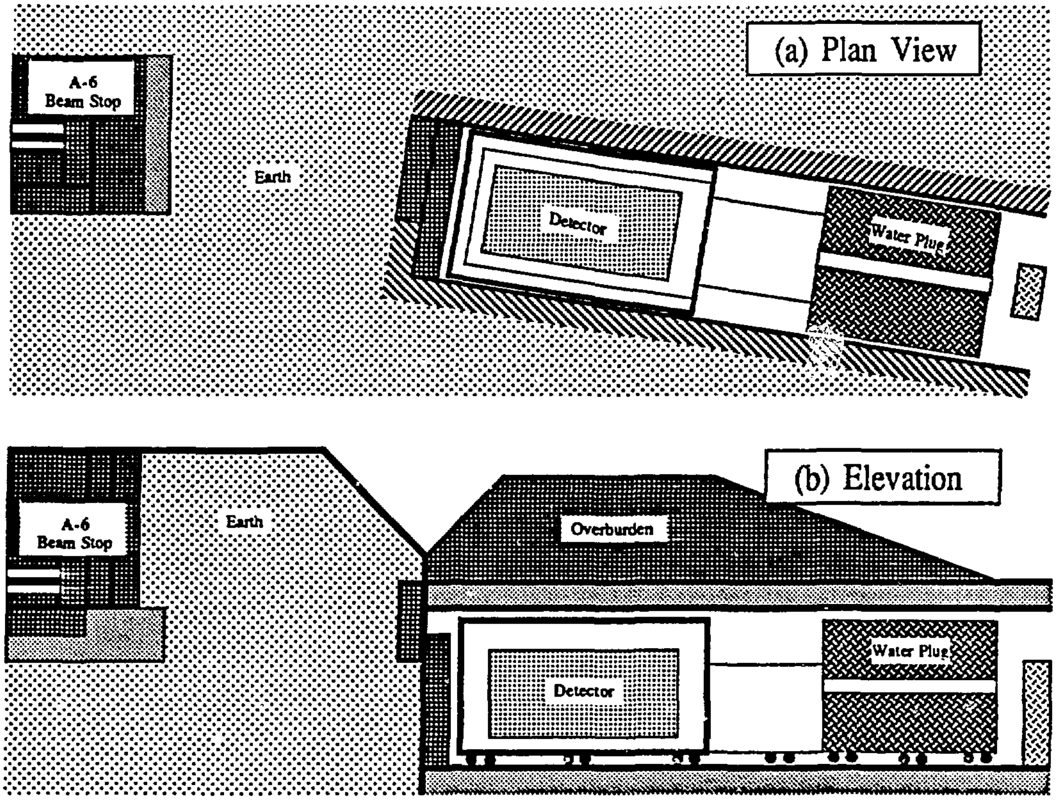

Figure 3.4: Views of LAMPF E645. (a) Plan view. (b) Elevation view.

paint. The detector is located in a tunnel 26.1m from the beam stop with the orientation given in Figure 3.4. The tunnel is covered with earth and steel overburden and the open end of the tunnel is plugged with a water filled tank.

The central detector is capable of observing $\bar{\nu}_e$ through the $\bar{\nu}_e$p CC reaction

$$\bar{\nu}_e + \mathrm{p} \rightarrow \mathrm{n} + e^+ \tag{3.12}$$

where the free proton targets are provided by the 1.54×10^{30} hydrogen atoms in the detector; 75% are contained in the hydrogen-rich liquid scintillator (CH_2). The central detector detects the positron with the PDTs and the liquid scintillator panels. The liquid scintillators measure the energy of the positron, that carries most of the energy of the incident $\bar{\nu}_e$. The PDTs provide both horizontal and vertical coordinates of the positron trajectory, which allow the reconstruction of the positron track in three dimensions. In addition, the PDTs and the liquid scintillators measure the differential energy loss (dE/dx) of reconstructed positron tracks which can be used for particle identification. The central detector also detects the final state neutron through the detection, by the liquid scintillator panels, of the gammas from the radiative neutron capture on gadolinium. The capture cross section is very small for neutrons above thermal energies, and the neutrons, which are produced with an initial energy of up to 5.2 MeV, must be moderated before capture can occur. The neutron moderation, which is made through elastic collisions with hydrogen and other nuclei in the central detector, delays the capture by up to $\sim 100\mu$s. The signature for the $\bar{\nu}_e$p CC event is the detection of the positron with the neutron capture in delayed ($\leq 100\mu$s) coincidence.

3.3 Backgrounds

Charged particles such as electrons ($e^+$and e^-), muons ($\mu^+$and μ^-), pions ($\pi^+$and π^-), and protons are all capable of giving false positron events. Backgrounds to the $\bar{\nu}_e$p CC signal will result when false positron events are in delayed coincidence with a correlated or an accidental neutron capture event. The sensitivity of the experiment in the search for $\bar{\nu}_e$ appearance is greatly limited by the ability to suppress such backgrounds. The major consideration in the design of the experiment and the analysis of the data is background suppression. We identify potential backgrounds, from both beam independent and beam associated sources, and discuss the techniques used for suppressing such backgrounds. Accidental slow neutron coincidences are also discussed.

3.3.1 Beam Independent Background

The beam independent background to the positron event is expected to have cosmic ray origins. Natural radioactivity as a possible source is unlikely due to the the positron detection threshold of 19 MeV. The surface cosmic ray flux consists of soft hadronic and electromagnetic components and a hard muonic component. The 2000g/cm^2 of overburden easily eliminates the electromagnetic component, which has an attenuation length of 50g/cm^2; and the neutron component, with an attenuation length of 300 g/cm^2, is reduced by 10^{-4}. The overburden reduces the highly penetrating muonic component by a factor of 1/3.5.

The 15.24cm thick liquid scintillator active shield is designed to reject all charged particles, especially muons, that would normally be incident upon the detector. The electronics for the active shield are designed so that the active shield can reject both prompt muon backgrounds, where the muon itself gives the false positron event; and delayed muon background, where an electron from the decay of the muon or from the decay of a spallation product gives the false positron event. The rejection of the delayed muon background is especially important, because muon decay results in electrons that have a similar energy spectrum as the energy spectrum of the positron from the $\bar{\nu}_e$p CC reaction. Additional rejection to the delayed muon background is given by the central detector by taking advantage of the tracking capability and rejecting events that are preceeded by a spatially correlated track.

Neutrons, which are part of the hadronic component that may have leaked through the overburden or been regenerated by the muonic component in the earth, may pass through the active shield without interacting. The primary interaction of the neutrons in the central detector is through elastic scattering from hydrogen, which can result in an energetic recoil proton. Inelastic processes with the production of photons and pions may also occur. It is important to reject neutron-induced false positron events, because these events may have a correlated delayed neutron coincidence. The rejection of the neutron-induced background comes primarily from particle identification. The central detector, which measures the total energy and dE/dx of single charged particle tracks, is capable of discriminating between electrons (both e^+ and e^-) and protons; also to a lesser degree, between electrons and photons, including those from $\pi^0 \rightarrow 2\gamma$ decay. Charged pions from inelastic neutron interactions can give prompt or delayed backgrounds. Prompt pion background events can be suppressed by particle identification and by identifying the pion decay products. Delayed pion background events, where the electron from $\pi^{\pm} - \mu^{\pm} - e^{\pm}$ decay fakes the positron, can be suppressed by rejecting events that are preceeded by a spatially correlated track in the central detector.

The regeneration of the electromagnetic component in the earth by the muonic component results in photons that can penetrate the active shield without interacting. The 142g/cm^2 thick passive lead shield reduces this photon background by more than a factor of 10^{-4}.

We would like to point out that the beam independent background rate will be measured and subtracted out from the data.

3.3.2 Beam Associated Background

Of the many particles produced in the LAMPF A-6 beam stop, only neutrons and neutrinos are capable of penetrating the 5.5m of steel and 14.5m of earth from the beam stop to the neutrino detector. Backgrounds caused by the beam associated neutrons are suppressed with the same methods used for rejecting the cosmic ray neutron background.

The ν_e for DAR μ^+ decay may have both NC and CC reactions with nuclei and electrons in the detector. The ν_μ from DAR π^+ decay and the $\bar{\nu}_\mu$ from DAR μ^+ decay may only have NC reactions, because the CC reactions are not kinematically allowed. The NC reactions by the DAR neutrinos on nuclei will result in a recoil nucleus that may be in an excited state. The visible energy of the recoil nucleus and the energy of the deexcitation gammas are below the positron detection threshold of 19 MeV. The neutrinos from DAR π^+ and μ^+ decay are not energetic enough to leave nuclei in excited states that deexcite with pion emission. The CC reactions with nuclei, and the NC and CC reactions with electrons, will result in electrons that have energies similar to the positron from the $\bar{\nu}_e$p signal. With the exception of the requirement of the delayed coincidence with a radiative neutron capture event, there is no way to discriminate the background neutrino reactions from the $\bar{\nu}_e$p signal. The rates of the background DAR neutrinos will be considered in the analysis.

Unlike the DAR neutrinos, the ν_μ and $\bar{\nu}_\mu$ from DIF π^+ and π^- have the necessary energy to engage in CC reactions. This results in the production of muons in the central detector. Like the cosmic ray muons, the CC reactions of the DIF neutrinos can give prompt backgrounds, where the muon fakes the false positron event; and delayed backgrounds, where the decay electron fakes the positron. The prompt backgrounds may be rejected by removing tracks that are followed by a decay signal within characteristic muon lifetimes. The delayed backgrounds may be removed by rejecting events that are preceeded by a spatially correlated track.

3.3.3 Accidental Neutron Coincidences

Gamma rays from the decay of naturally occurring radionuclides will mimic radiative neutron gadolinium capture and give accidental coincidences. In order to reduce the rate of accidental coincidences, it is necessary to make a unique signature for neutron capture. We take advantage of the high gamma ray multiplicity ($< n_\gamma > \sim 4.0$ [45] for $E_\gamma \geq 0.1$MeV) for neutron capture on gadolinium and require the detection of two or more gamma rays characterized by coincident signals in two or more scintillator panels.

There is also the possibility of accidental coincidences from stray neutrons. We reduce this accidental rate by requiring that the capture event is spatially correlated with the positron.

3.4 Detector Components

We will provide brief detail of the neutrino detector. Additional details on the detector and its performance are given elsewhere [46,47,48,49].

3.4.1 Proportional Drift Tubes

The PDTs are constructed from 1.5mm thick laminated paper formed into 3.7m long tubes with an outer rectangular cross section of 4.3cm by 8.128cm. The outer surface of each tube is coated with epoxy to seal against gas leaks and the inner surface is lined with overlapping layers of aluminumized mylar tape; the purpose of the aluminum is to shape the electric field. The thickness of the aluminum (33.0μm, including the overlap) is kept to a minimum to reduce the number of targets for the $\nu_e{}^{27}$Al CC reactions, which is a background for $\bar{\nu}_e$ appearance. A 50μm gold-coated tungsten anode wire, which runs down the center of the tube, is kept at positive high voltage (1950 V) and the aluminum surface is electrically grounded. The PDT gas (90% argon and 10% methane mixture) is continuously recirculated. Nine PDTs are glued together to form a 9-wire bank, with a fixed wire spacing of 8.128cm. The PDT contribution to a detector module consists of one plane of five horizontally oriented 9-wire banks and one plane of five vertically oriented 9-wire banks.

3.4.2 Liquid Scintillator Panels

The scintillator panels are constructed from pre-formed extruded plastic boxes with dimensions 3.66m long, 30.5cm high, and 3.64cm thick with a wall thickness of 3.2mm. A 2.92mm thick rib is glued to the center of each box to reduce hydrostatic bulging. Each panel is covered with a 3mil thick sheet of white paper that is covered with a 2mil thick sheet of tedlar (black mylar) to ensure optical isolation. The white paper insures that there is an air gap, between the panel and the tedlar, which traps much of the scintillation light in the panel through total internal reflection. The panels are filled with Bicron 517L liquid scintillator with a scintillator thickness of 3cm. The scintillation light in each panel is viewed by two Hamamatsu R878 photomultiplier tubes (PMT) that are mounted on the end caps of the panels. The scintillator plane consists of 12 vertically suspended panels.

3.4.3 Gadolinium Sheets

The gadolinium-loaded paint consists of a mixture of Gadolinium-Oxide (Gd_2O_3) and ordinary water-based latex house paint. We use a concentration that results in 350g of Gd_2O_3 (or 300g of natural Gd) per 1000g of dry Gd-loaded paint. Twelve feet long by 3 feet wide by 5mil thick mylar sheets are painted with three airless mechanical paint sprayers, each with a 1 foot wide spray. The mylar sheets are pulled vertically through the sprayers with a variable speed DC motor, at a speed such that the mylar sheets are coated with a minimum of $5\mathrm{mg/cm^2}$ of gadolinium. The average thickness of the gadolinium coating is determined by weighing the gadolinium-coated sheets after drying. This method of measuring the thickness is confirmed by taking samples of gadolinium coated sheets and inserting them into a prototype neutron detector, where the neutron detection efficiency is measured and compared to that of a standard sheet. One gadolinium-coated sheet is hung on each side of a liquid scintillator plane, providing a minimum of $10\mathrm{mg/cm^2}$ of gadolinium per module.

3.4.4 Active and Passive Shielding

The shield is basically a steel structure that has a cylindrical shape with a diameter of 6.75m and a length of 10.1m. Both ends of the cylinder are closed with vertical walls and the cylinder is truncated with an opening of 120°, which is closed with a flat bottom. The shield structure is divided into two concentric tanks. The 17.78cm thick inner tank contains the lead passive shielding, which is in the form of lead shot. The lead shot is loaded with a packing fraction of 70%, which gives an effective lead thickness of 12.45cm. The 15.24cm thick outer tank contains the liquid scintillator (Bicron BC 517P) active shield. The front wall (nearest to the beam stop) and the cylinder are structurally independent from the remainder of the shield and make one continuous sheet of scintillator. The remainder of the active shield is divided up into 8 optically-isolated sections with the back wall as one section and the remaining

7 on the bottom. A 1.27cm thick crescent-shaped plastic scintillator covers the dead region at the intersection of the cylinder and the back wall. A total of 360 EMI 9870B PMTs view the light from the liquid scintillator, with 45 PMTs mounted on each vertical wall, 200 PMTs mounted on the cylinder, and 70 PMTs mounted on the bottom. In addition, 16 AMPEREX 2230 PMTs view the light from the plastic scintillators.

3.4.5 Neutrino Tunnel

The detector is located in a 7.75m diameter tunnel that is covered by 2000g/cm^2 of earth and steel overburden. There is 3000g/cm^2 of overburden directly above the detector. The open end of the tunnel is plugged with a mobile 8m long water-filled cylindrical tank.

3.5 Electronics

The signals from the central detector PMTs and PDTs and the active shield PMTs are digitized. Upon receiving the sign of a "good" event, i.e., a trigger, the digitized signals are read out with a CAMAC based data acquisition system. We discuss the trigger and the signal digitization below.

3.5.1 Trigger

In the search for $\bar{\nu}_e$ appearance, we accept gated detector triggers and random triggers using the logic given in Figure 3.5. Details of the triggers and the gates are given below.

The detector trigger is generated by the signals from the central detector scintillator PMTs. These signals are sent to fast-logic FASTBUS cards where they are discriminated and latched in a register for 300ns. The discriminator threshold is

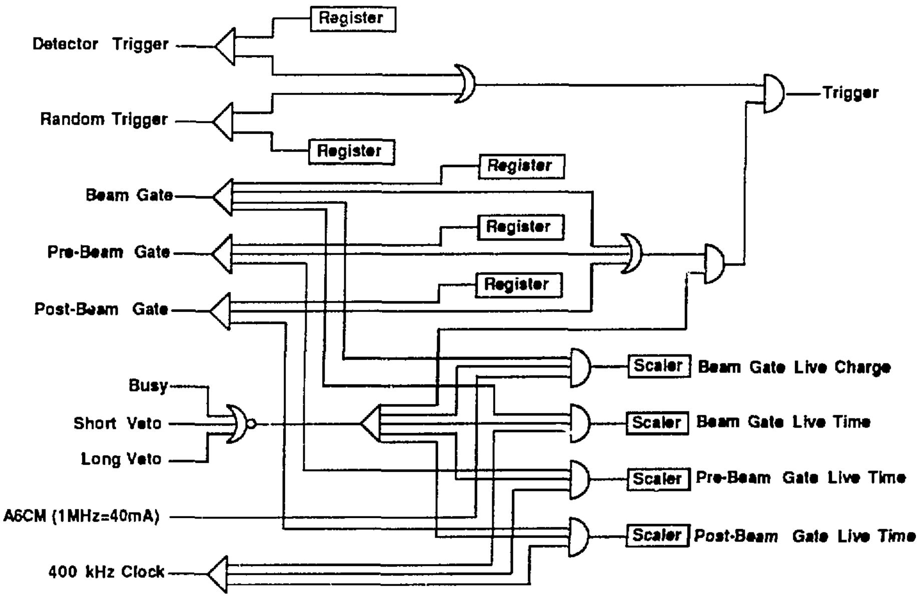

Figure 3.5: Trigger logic for the $\bar{\nu}_e$ appearance experiment.

equivalent to an energy deposition of 0.5 MeV for a minimum ionizing particle passing through the center of the panel. The fast-logic cards test, at 250ns intervals, each scintillator plane for ANDs and ORs. The plane will have an AND if both PMTs in any one of the 12 scintillator panels in the plane are latched and the plane will have an OR if any one of the plane's 24 PMTs are latched. The ANDs and ORs are loaded into the memory of the trigger processor, which issues a trigger if the pattern in the memory matches a pre-loaded pattern. In the $\bar{\nu}_e$ appearance experiment, we use a pattern that is equivalent to requiring 3 ANDs in any 4 contiguous planes.

The random trigger is generated by a 0.03 Hz pulser. This trigger is used to determine some offline neutrino detection efficiencies and to measure the rate of the accidental slow neutron coincidences.

Both the detector triggers and the random triggers are rejected if they occur when the data aquisition is busy reading the previous event or when an online veto condition is set. The veto conditions are generated by the active shield, which is divided into three logical sections: the cylinder including the front wall, the back wall, and the bottom. The active shield PMT signals are discriminated, and for each section, the number of PMTs with signals above threshold are counted at intervals set by the 250ns fast-logic clock. Each section is latched when a predetermined PMT multiplicity threshold is met. In the $\bar{\nu}_e$ appearance experiment, the multiplicity threshold for the cylinder is five PMTs, the back wall is four PMTs, and the bottom is three PMTs. A Short Veto condition (2.5μs in length) is set when two or more logical sections of the active shield are latched. The purpose of the Short Veto is to suppress triggers caused by cosmic ray muons that pass completely through the central detector and the shield. A Long Veto condition (11.0μs in length) is set when exactly one logical section of the active shield is latched. The purpose of the Long Veto is to suppress triggers caused by the decay electrons of cosmic ray muons that pass through one section of the shield and stop in the central detector.

LAMPF provides the experiment with three gate signals, the RF-Gate, the Beam Gate Permissive, and the Pre-T_0. We use these signals to make the Beam Gate, the Pre-Beam Gate, and the Post-Beam Gate. The RF-Gate runs at 120Hz and is always on regardless of whether LAMPF is producing a beam. The proton beam is allowed only when both the RF-Gate and the Beam Gate Permissive are on, so the Beam Gate is the logical "and" of the RF-Gate and the Beam Gate Permissive. The Pre-T_0, which also runs at 120Hz, precedes the RF-Gate by 1.7 ms. This is considered to be the period when the accelerator is the "quietest." The Pre-Beam Gate, which is set to have a length of 1ms and is initiated by the Pre-T_0, is used for measuring the beam independent background. The Post-Beam Gate has a length of 1ms and is initiated 100μs after the tailing edge of the Beam Gate. This gate is used for measuring the possible "long-lived" ($\sim$ 1 ms) beam associated backgrounds.

The live time in each gate is measured with a 400kHz clock. The clocks are scaled by 24-bit CAMAC scalers that are read-out and cleared with each trigger. In addition, the live proton charge in the Beam Gate, which is measured by the A-6 beam stop current monitor (A6CM), is also scaled.

3.5.2 Digitization

The digitizers for the central detector PMTs and PDTs, and the active shield PMTs are located in FASTBUS cards for increased density. The central detector PMTs and the PDTs use the same digitization system, which requires that the fast ($\sim$ 25ns) PMT pulse be stretched to 2μs in order to have a similar shape to the PDT pulse. Signals from the PMTs and PDTs are digitized with 6-bit RCA 3300D flash analog to digital converters (FADC). Two FADCs with overlapping gains are used to cover the wide dynamic range. For economical reasons, both the PMT and PDT pulse digitization are done in multiplex where the signals from 8 PMTs or a 9-wire PDT bank are combined into groups. In each group, the pulses are linearly summed resulting in a "group" pulse that is digitized. Nine discriminators are used to identify which members of the group contribute to the "group" pulse. The arrangements of the PMTs and PDTs into groups are such that an ideal single charged-particle track will give "group" pulses that have exactly one member. The FADCs and the discriminators are strobed by a 12.3 MHz clock, which gives typically 20-30 samples per pulse. For each group, a history of 2048 samples (166.7μs) is cyclicly stored in random access memory (RAM) where any "old" data is overwritten. Upon receiving a trigger, the clock is stopped after a delay of 110μs. At this point, the history of the entire central detector 56.7μs before the trigger, at the time of the trigger, and and 110μs after the trigger is frozen in the RAMs. The data stored in the RAMs is then compacted (only FADC data above threshold is retained) and transferred to CAMAC with a microcode programmable FASTBUS controller.

The active shield PMTs are served by a separate digitization system, which is similar to the central detector system in many respects. Pulses from the shield PMTs are also digitized with 6-bit RCA 3300D FADCs, which are strobed with a 6.67 MHz clock. There is no multiplexing and there is one FADC for each shield PMT. A history of 1024 samples (153.6 μs) is stored cyclicly in RAM until receiving a trigger when the clock is stopped after a delay of 100μs. The data stored in the RAMs is then compacted and transferred to CAMAC.

Chapter 4

Analysis Tools

4.1 Event Reconstruction

Raw events consist of time and pulse height information of the central detector scintillator PMTs, the PDTs, and the active shield scintillator PMTs. To optimize this information, raw events are reconstructed into "physical" events. The first step in the reconstruction process is to independently bin the 166.7μs of central detector history and 153.6μs of active shield history into time slices of temporally correlated signals. In the central detector, there are two basic types of events that we will be examining: charged particle tracks and radiative neutron capture on gadolinium. The search is made in the relevant time slices for these types of events. In the active shield, we examine the intersection of charged particles with the shield. Details of the event reconstruction are given below.

4.1.1 Time Slices

The binning of central detector history is somewhat complicated by the fact that, although the scintillator PMTs give prompt signals, the PDT signals are delayed due to the drift times. To handle this difficulty, time slices with a bin width of 0.205μs (2.5 clock ticks) are initially made using only the scintillator PMT signals.

The average of all the PMT signal times in the time slice defines the reference time. The PDTs are folded in by matching PDTs to the existing time slices if the PDT time is within the window $[-0.5, 2.0)$ μs relative to the reference time. This relatively long time window accounts for the PDT drift times. There will be events where more that one time slice will be within a 2.5μs window, which will introduce an ambiguity in terms of the PDT matching; it is possible for PDTs to be shared by multiple time slices. This ambiguity is resolved in the detector track search. The central detector time slice procedure is completed by binning the remaining unmatched PDTs into time slices with a bin width of 1.0μs. The time slice that occurs at the time of the trigger is of particular importance because this time slice contains the event that forced the trigger.

The shield PMTs pulses, which are prompt, are binned into time slices with a 0.15μs (1 clock tick) bin width.

4.1.2 Charged Particle Tracks

A typical charged-particle track in the central detector is shown in Figure 4.1. Each detector time slice is searched for such events. It is convenient at this point to introduce a cartesian coordinate system for the detector: the z-axis is normal to the detector planes and points away from A-6 beam stop, the y-axis is vertical and points towards the sky, and the x-axis completes the right-handed system. The XPDTs are vertically-oriented PDTs that provide the x-coordinates of the charged particle track. Similarly, the YPDTs are horizontally oriented and provide the y-coordinates. The scintillator panels also provide crude y-coordinates of charged particle tracks. The x-profile is the plane perpendicular to the x-axis and the y-profile is the plane perpendicular to the y-axis. The YPDTs and the scintillator panels provide the coordinates of the charge particle track in the x-profile and the XPDTs provide the coordinates in the y-profile.

An independent search in the x-profile and the y-profile is made for charged

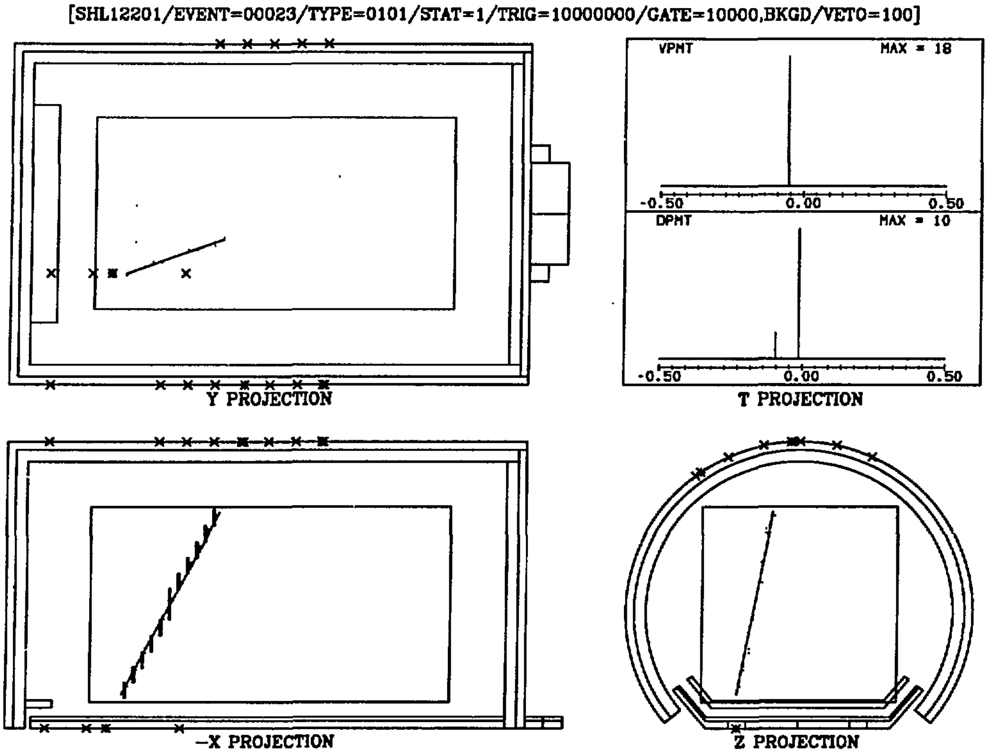

Figure 4.1: One event display of a charged particle track in the neutrino detector. The panel in the upper left hand corner displays the time history, in μs, of the active shield PMTs (VPMT) and the central detector PMTs (DPMT). The remaining panels represent different views of the event. The crosses on the shield represent hit PMTs; and the boxes and the dots in the central detector represent hit scintillator panels and PDT wires respectively. The solid line is the fitted charged particle track.

particle tracks. The search involves selecting XPDTs, YPDTs, and scintillator panels that are in contiguous planes and that fall on a straight line. The tolerance for the track element selection is determined by the size of the elements. If the track selection contains results in more than two elements, a least squares line fit is made to determine the precise line parameters. The fit in the x-profile is weighted to account for the sensitivity of the y-coordinate determinations of the liquid scintillator panels and the YPDTs. At this point the elements that are adjacent to the track, but are not currently part of the track, are selected so that possible delta-rays are included. The line parameters provide the (x,y,z) endpoints

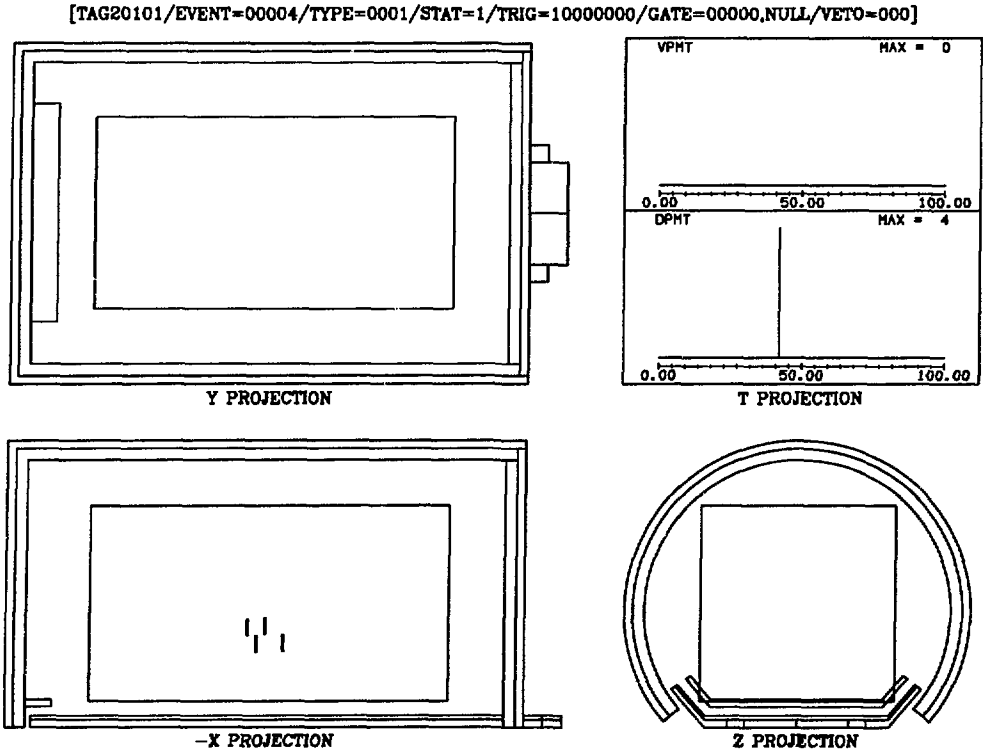

Figure 4.2: One event display of a Monte Carlo generated radiative neutron gadolinium capture. The panel in the upper left hand corner displays the time history, in μs, of the active shield PMTs (VPMT) and the central detector PMTs (DPMT). The remaining panels represent different views of the event. The boxes in the central detector represent hit scintillator panels.

and the direction cosines ($\cos\theta_x$,$\cos\theta_y$,$\cos\theta_z$). This experiment does not have the ability to determine the absolute track direction, so by definition $\cos\theta_z \geq 0$. The direction cosine $\cos\theta_z$ is of particular importance because it is proportional to the amount of material the charged particle track transverse in a plane.

4.1.3 Slow Neutron Capture

A Monte Carlo generated radiative neutron gadolinium capture event is shown in Figure 4.2. We reduce such events to four parameters: the time of the event, the scintillator panel multiplicity, the energy, and the spatial position. The time of the event is given by the reference time of the time slice. We define the scintillator panel multiplicity in terms of ANDs and XORs of the PMTs on the panels. The scintillator panel is defined to have an AND if both PMTs of the panel fire (PMT signal pulse height is above the FADC compaction threshold). Similarly, the scintillator panel is defined to have an XOR (exclusive "or") if exactly one PMT fires. The energy of the neutron capture event is taken to be the visible energy that is defined in the next section. The spatial position of the event is defined to be the average position of the scintillators. This gives the y and z coordinates. Because the capture events do not usually give signals in the PDTs, the x coordinate of the capture event is unknown.

The signature for radiative neutron capture on gadolinium is based upon the above parameters.

4.1.4 Shield PMT Cluster

Charged particles that penetrate the liquid scintillator active shield will leave a cluster of PMTs as found in Figure 4.3. It is useful in the analysis to search for and parameterize these clusters. The relevant cluster parameters are the time, the PMT multiplicity, the visible energy, and the spatial position. The time of the cluster is simply the average of all the PMT times in the cluster. The visible energy is the sum pulse height of all PMTs in the cluster. The spatial position of the cluster is the pulse height weighted average position of all the PMTs in the cluster.

4.2 Event Energy

The central detector is capable of measuring visible energy of all events and the differential energy loss of charged particle tracks. We discuss the energy measurements and the calibration of the energy scale.

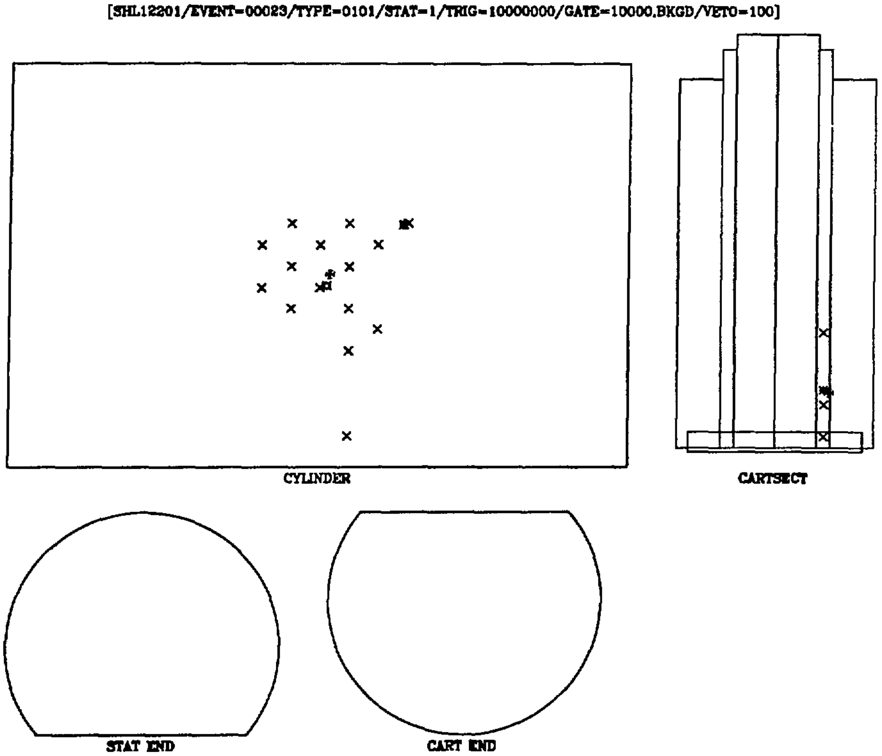

Figure 4.3: One event display of the active shield. The four panels represent the surfaces of the active shield. The crosses represent hit PMTs and the star bursts represent the PMT clusters. The fancy crosses are the projection of the track, in the central detector, onto the shield.

4.2.1 Energy Scale Calibration

The energy deposited by charged particles in the scintillators and the PDT gas is recorded as digitized signals from the scintillator PMTs and the PDT anode wires. The energy scale calibration determines the conversion from the signal pulse height, in FADC channel number, into real deposited energy. We use cosmic ray muons to perform this calibration. Cosmic ray muons are highly penetrating particles and the energy deposited in the scintillators and the PDT gas will follow a Landau distribution [50]. The average energy deposition (E_{AVG}) and most probable energy deposition (E_{PROB}) are two possible parameters from the Landau distribution that could be used as the reference point for the energy scale. We have calculated E_{AVG}

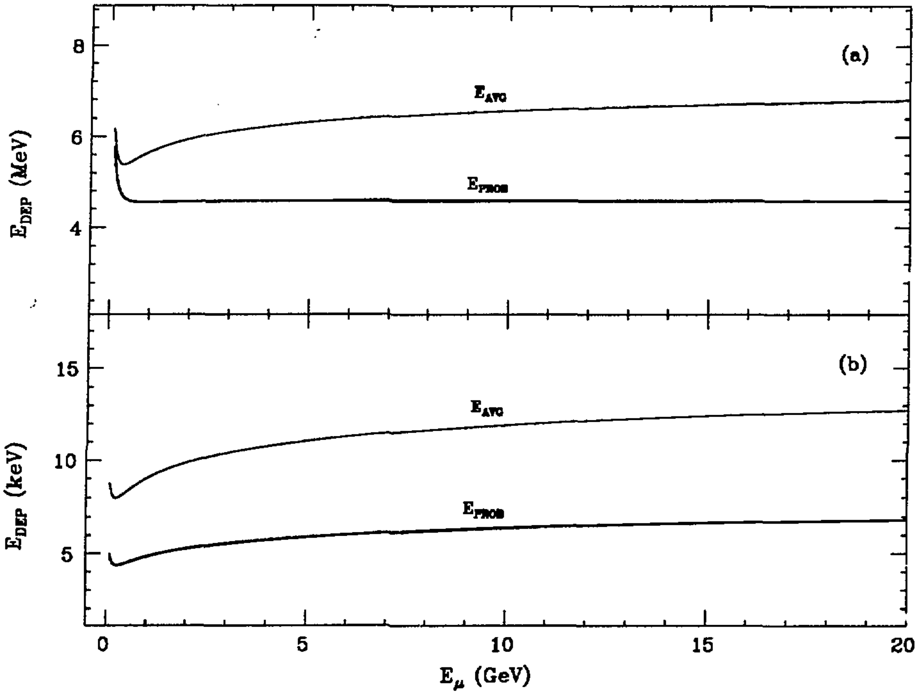

Figure 4.4: The average muon energy deposition (E_{AVG}) and the most probable muon energy deposition (E_{PROB}) (a) in the liquid scintillator and (b) in the PDT gas versus the incident muon kinetic energy. The muons have normal incidence to the detector planes and penetrate 3.0cm (2.57g/cm^2) of liquid scintillator and 3.99cm (5.19mg/cm^2) of PDT gas.

using the Bethe-Bloch formula [51,52] and E_{PROB} using the Landau formula [50], both corrected for the density effect [53,54,55], for muons with normal incidence to the detector planes and variable incident muon energy. The results of this calculation, which is given in Figure 4.4, reveals that for muons with kinetic energy greater than 0.4 GeV, E_{PROB} is nearly independent of incident muon energy, i.e., the muon is minimum ionizing. The average energy of cosmic ray muons incident on the detector is 2 GeV, which means that cosmic ray muons are in the minimum ionizing regime. The independence of E_{PROB} to the incident muon energy makes E_{PROB} an ideal reference parameter for defining the energy scale.

The database for the calibration consists of events triggered by the central detector without the active veto. Cosmic ray muons, which would normally be suppressed by the veto, are expected to make up the majority of the reconstructed events in this database. Muons in this database transverse different amounts of liquid scintillator and PDT gas, which will give energy depositions that are dependent upon the track direction cosine $\cos\theta_z$. The energy deposition is proportional to the amount of material the muon transversed; i.e.,the energy deposited, $\mathrm{E_{DEP}}(\cos\theta_z)$, by a muon with direction cosine, $\cos\theta_z$, is equal to

$$E_{DEP}(\cos\theta_z) = \frac{1}{\cos\theta_z} E_{DEP}(\cos\theta_z = 1) \tag{4.1}$$

where $\mathrm{E_{DEP}}(\cos\theta_z = 1)$ is the energy deposited by a muon with normal incidence to the detector planes. We use $\cos\theta_z$, which is determined by the track reconstruction, and Equation 4.1 to make the thickness correction to the energy deposition.

The most probable, $\mathrm{E_{PROB}}$, is not proportional to the amount of material transversed by the muon. To ensure that Equation 4.1 remains a reasonable approximation, we limit the calibration to muons with $\cos\theta_z \geq 0.5$. We represent $\mathrm{E_{PROB}}$ by an average $\overline{\mathrm{E}}_{\mathrm{PROB}}$, which is defined to be

$$\overline{E}_{PROB} = \int_{0.0}^{0.5} d\cos\theta_z \frac{dN_\mu}{d\cos\theta_z} \cos\theta_z E_{PROB}(\cos\theta_z) \tag{4.2}$$

The quantities used in the evaluation of $\overline{\mathrm{E}}_{\mathrm{PROB}}$, including the empirical muon distribution $\mathrm{dN_\mu/d\cos\theta_z}$, are given in Figure 4.5. These evaluations result in $\overline{\mathrm{E}}_{\mathrm{PROB}}(\mathrm{SCI}) = 4.66\mathrm{MeV}$ for the liquid scintillator and $\overline{\mathrm{E}}_{\mathrm{PROB}}(\mathrm{PDT}) = 6.21\mathrm{keV}$ for the PDT gas. In Figure 4.5, we plot these values of $\overline{\mathrm{E}}_{\mathrm{PROB}}$ against the quantity $\cos\theta_z \cdot \mathrm{E_{PROB}}$. The maximum deviation is 2% for the scintillators and 4% for the PDTs, which is comparable to the uncertainty in the Landau formula for $\mathrm{E_{PROB}}$ [53].

The basic calibration procedure involves making distributions of signal pulse height quantities, which are proportional to the muon energy deposition. The peak, i.e., the most probable energy deposition, of the distributions gives the energy scale calibration from signal pulse heights in FADC channels to real energy deposition in

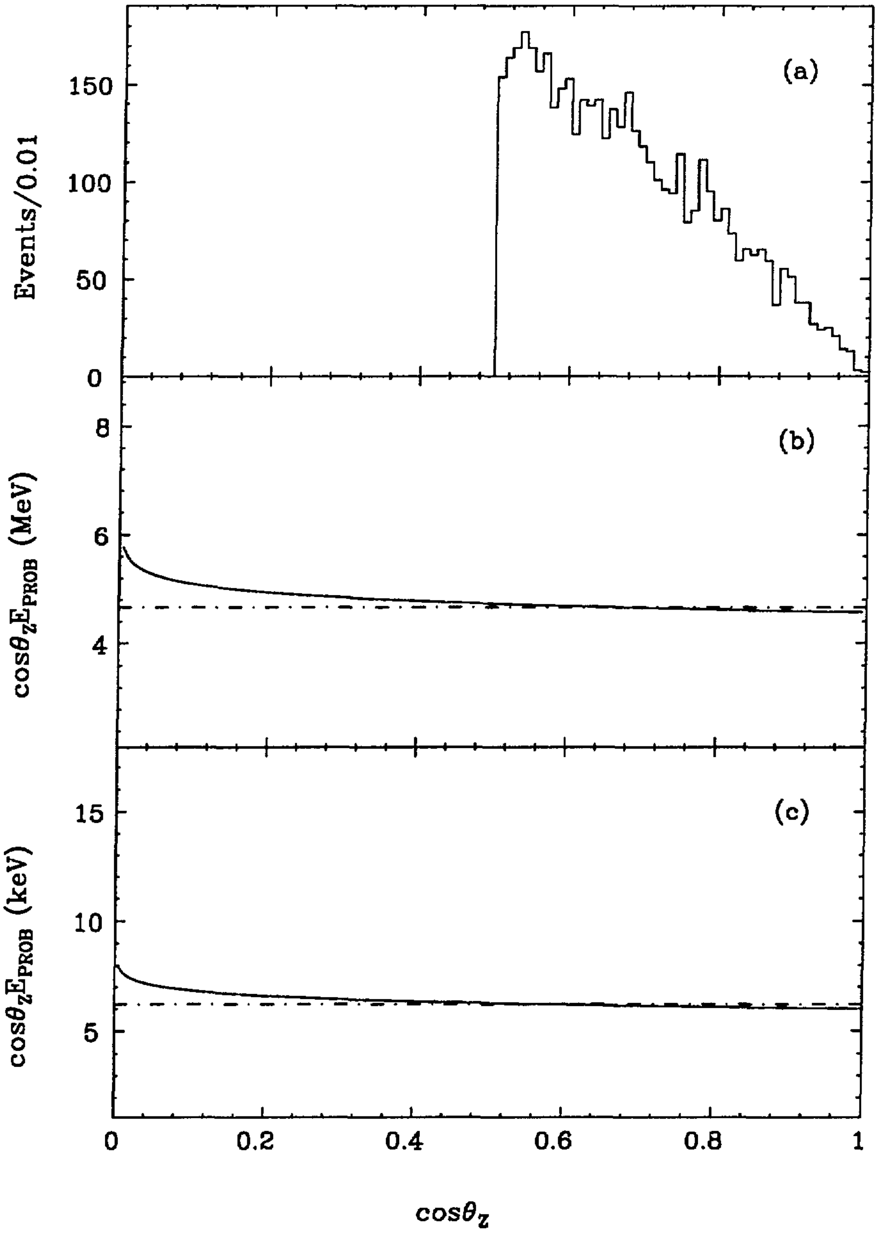

Figure 4.5: Distributions used in the evaluation of $\overline{E}_{PROB}$. (a) The empirical $\cos\theta_z$ distribution of muon tracks in the detector. (b) The quantity $\cos\theta_z \cdot E_{PROB}$ for the scintillators (solid line). (c) The quantity $\cos\theta_z \cdot E_{PROB}$ for the PDT gas (solid line). The dot-dash lines in (b) and (c) are the computed values of $\overline{E}_{PROB}$.

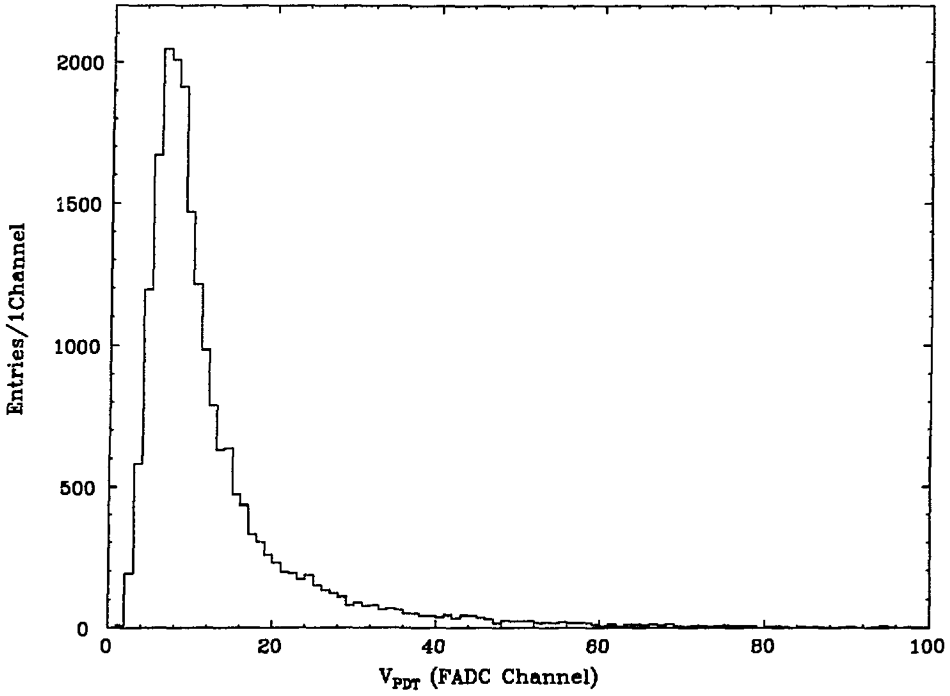

Figure 4.6: Typical V_{PDT} distribution. The peak is at 7.4 FADC channels and the FWHM is 96% of the peak.

MeV. In the case of the PDTs, the anode signal pulse heights, V_{PDT}, are directly proportional to the muon energy deposition and for each PDT along a reconstructed muon track, we histogram the quantity

$$\cos\theta_z \cdot V_{PDT} \tag{4.3}$$

where the $\cos\theta_z$ factor is to correct for PDT gas thickness. A typical V_{PDT} distribution is shown in Figure 4.6. For each calibration run , there are 410 such distributions; one for each PDT 9 wire bank. In addition to the peak, the full width half maximum (FWHM) of each distribution is also determined for diagnostic purposes.

The calibration of the scintillators is complicated by the attenuation of the scintillation light in the panels. The scintillation light in the panels viewed by each

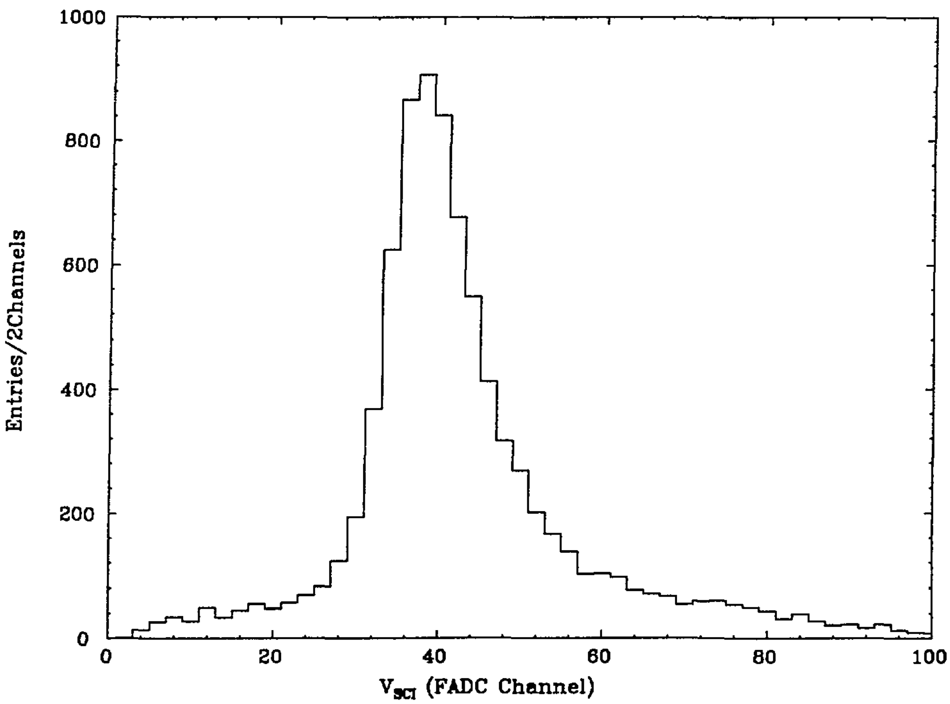

Figure 4.7: Typical V_{SCI} distribution. The peak is at 38.0 FADC channels and the FWHM is 34% of the peak.

of the two PMTs (PMT1 and PMT2) will be dependent upon the the position where the charged particle penetrates the scintillator. Because the length of the panels (366cm) is much greater than the height (30.5cm) and the width (3.64cm), the attenuation depends primarily on the coordinate that runs parallel to the panel length, which happens to be the x-coordinate. The x-coordinate is defined such that given the panel length l, PMT1 is located at $x = -\frac{l}{2}$ and PMT2 is located at $x = +\frac{l}{2}$. The attenuation is expected to be approximately exponential, i.e., if V_{PMT1} and V_{PMT2} are the pulse heights of the signals in PMT1 and PMT2 respectively, resulting from a muon which penetrated the scintillator at a position x and deposits E_{DEP} in the scintillator, then V_{PMT1} and V_{PMT2} are equal to

$$V_{PMT1}=g_1 E_{DEP} e^{-(\frac{l}{2}+x)/\Lambda}$$

$$V_{PMT2}=g_2 E_{DEP} e^{-(\frac{l}{2}-x)/\Lambda} \tag{4.4}$$

where Λ is the attenuation length. The factors g_1 and g_2 depend upon the gains and the geometrical acceptance of the PMTs; and on the scintillation efficiency that is independent of E_{DEP} for minimum ionizing particles. We would like to make distributions of a quantity relating V_{PMT1} and V_{PMT2} to a quantity proportional to E_{DEP}, which means removing the dependence upon x. The position dependence may be removed by taking the geometric mean of the pulse heights of the two PMTs. This gives a motivation for defining the scintillator "pulse height" as

$$V_{SCI} = \sqrt{V_{PMT1} \cdot V_{PMT2}} \tag{4.5}$$

which is proportional to E_{DEP}. The distribution of

$$\cos\theta_z \cdot V_{SCI} \tag{4.6}$$

is used for calibration. This is an excellent quantity because it is not necessary to know x and it is possible to measure the energy of un-tracked events. However, in order to optimize the performance of the detector, we would like to make the calibration a part of an iterative process where the gains on the individual PMTs are matched. We may remove the dependence on x by calibrating with equivalent muons that penetrate the scintillator at x = 0. The appropriate distributions are

$$\begin{gathered} \cos\theta_z \cdot V_{PMT1} \cdot e^{+x/\Lambda} \\ \cos\theta_z \cdot V_{PMT2} \cdot e^{-x/\Lambda} \end{gathered} \tag{4.7}$$

where it becomes necessary to know Λ. The attenuation length Λ, which depends upon the construction quality of the panels, must be determined for each panel. However, by making simple manipulations to Equation 4.4, we obtain the linear equation

$$\ln(\frac{V_{PMT2}}{V_{PMT1}}) = (\frac{2}{\Lambda}) \cdot x + \ln(\frac{g_2}{g_1}) \tag{4.8}$$

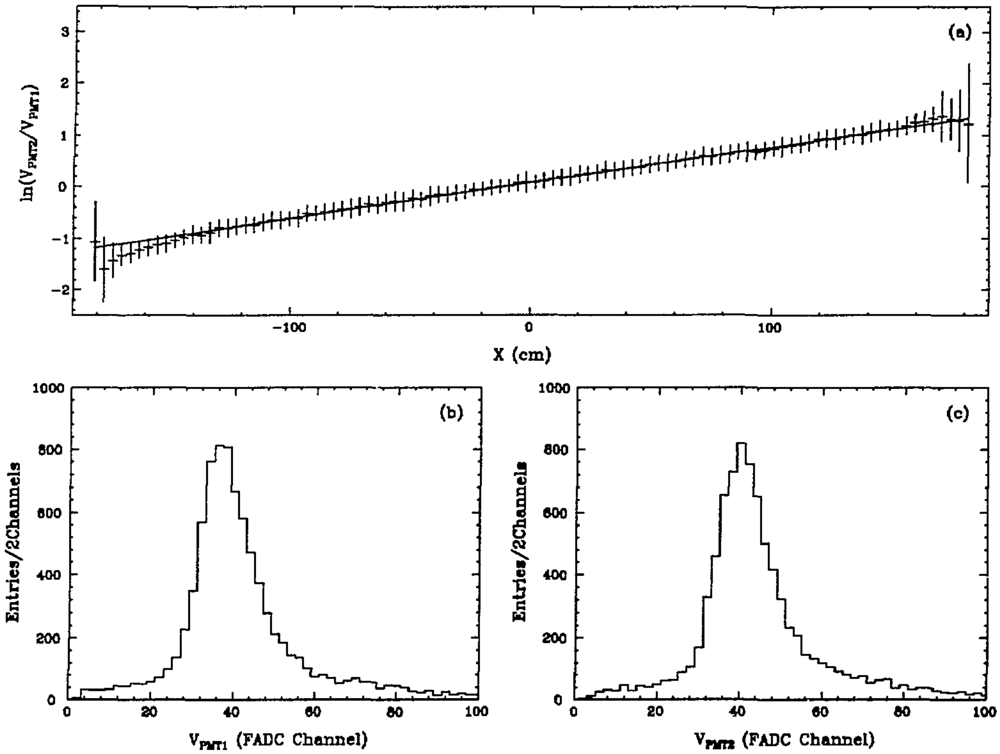

Figure 4.8: Calibration distributions of a typical scintillator panel. (a) Distribution of $\ln(V_{PMT2}/V_{PMT1})$ versus x. The fit yields an attenuation length of $\Lambda = 288$cm. (b) The V_{PMT1} distribution. The peak is at 37.0 FADC channels and the FWHM is 40% of the peak. (c) The V_{PMT2} distribution. The peak is at 40.0 FADC channels and the FWHM is 37% of the peak. The vertical bars in (a) represent two standard deviations in the values of $\ln(V_{PMT2}/V_{PMT1})$.

For each scintillator panel, we make a plot of $\ln(V_{PMT2}/V_{PMT1})$ versus x, an example of which is shown in Figure 4.8a. The attenuation length Λ is determined by making a least squares fit using Equation 4.8. Using the attenuation length Λ as measured above, we make distributions of the pulse heights for muons given in Equation 4.7. For each distribution, the most probable energy deposition is determined and recorded. The FWHM of each distribution is determined for diagnostic purposes.

In summary, we define the energy scale of the central detector using cosmic ray muons. The most probable energy deposition is used as the reference. For each 9 wire bank of PDTs there is one calibration constant, the peak of the $\cos\theta_z V_{PDT}$ distribution, which we label U_{PDT}. For each scintillator panel there are four calibration constants: the attenuation length Λ, the peak (U_{SCI}) of the $\cos\theta_z V_{SCI}$ distribution, and the peaks (U_{PMT1} and U_{PMT2}) of the $\cos\theta_z V_{PMT1}\exp(+x/\Lambda)$ and $\cos\theta_z V_{PMT2}\exp(-x/\Lambda)$ distributions.

4.2.2 Visible Energy

The visible energy (E_{vis}) of an event is defined to be the total energy deposited into the scintillators and viewed by the PMTs. We ignore the visible energy in the PDT gas, which is almost three orders of magnitude smaller. With the above definition, the visible energy of an event in a given time slice is equal to

$$E_{vis} = (4.66\mathrm{MeV}) \sum_{SCI} \frac{V_{SCI}}{U_{SCI}} \tag{4.9}$$

where V_{SCI} is the scintillator pulse height, U_{SCI} is the peak of the V_{SCI} calibration distribution, and the sum is over all scintillators in the time slice.

4.2.3 Differential Energy Loss

We measure the differential energy loss (dE/dx) of charged particles that pass through the PDT gas or the scintillators, relative to minimum ionizing particles that have normal trajectories to the detector planes. The unit of measurement for dE/dx is in *minimum ionizing particles* (MIPs). The peak of the dE/dx distribution of minimum ionizing particles will peak at dE/dx = 1 MIP. With the above definitions, a charged particle passing through a plane of PDTs with a direction cosine of $\cos\theta_z$ will have dE/dx of

$$\frac{dE}{dx}(PDT) = \cos\theta_z \cdot \frac{V_{PDT}}{U_{PDT}} \tag{4.10}$$

In order to account for possible delta-rays, PDTs adjacent to the track are included in the evaluation of dE/dx. The dE/dx for charged particles passing through a scintillator plane is equal to

$$\frac{dE}{dx}(SCI) = \cos\theta_z \cdot \begin{cases} \frac{V_{SCI}}{U_{SCI}} & \text{if } \mathrm{V_{PMT1}} > 0 \text{ and } \mathrm{V_{PMT2}} > 0 \\ \frac{V_{PMT1}}{U_{PMT1}} e^{+x/\Lambda} & \text{if } \mathrm{V_{PMT1}} > 0 \text{ and } \mathrm{V_{PMT2}} = 0 \\ \frac{V_{PMT2}}{U_{PMT2}} e^{-x/\Lambda} & \text{if } \mathrm{V_{PMT2}} > 0 \text{ and } \mathrm{V_{PMT1}} = 0 \end{cases} \tag{4.11}$$

The scintillator dE/dx also includes scintillators adjacent to the track to account for possible delta-rays.

4.3 Monte Carlo

We use Monte Carlo techniques to model the response of detector to electrons (e^+ and e^-) and neutrons. The electron and neutron Monte Carlos are checked against control samples. Monte Carlo techniques are also used to predict neutrino yields. Details are given below.

4.3.1 Control Samples

Cosmic ray muons that stop and decay in the detector provide an abundant source of electrons (both e^+ and e^-) that have an energy spectrum that is very similar to the e^+ spectrum of the $\bar{\nu}_e$p CC signal. Because stop muon events are a major source of background for the $\bar{\nu}_e$p CC signal, much effort has been focussed on designing a detector to veto these events. By "inverting" the veto, we are able to select stop muon events; an example of a selected stop muon event is shown in Figure 4.9. We measure the lifetime of the muon to test whether these events are real muon decays. In Figure 4.10 we histogram the time of the muon (t_μ) relative to the time of the decay electron muon (t_e). A fit made to Figure 4.10 with an exponential added to a flat background, i.e.,

$$N = N_0 \exp^{-(t_e - t_\mu)/\tau} + B$$

results in a muon mean lifetime of $\tau = 2.10 \pm 0.02\mu$s. This is in rough agreement with the calculated value of 2.15μs for cosmic ray muons stopped in the detector

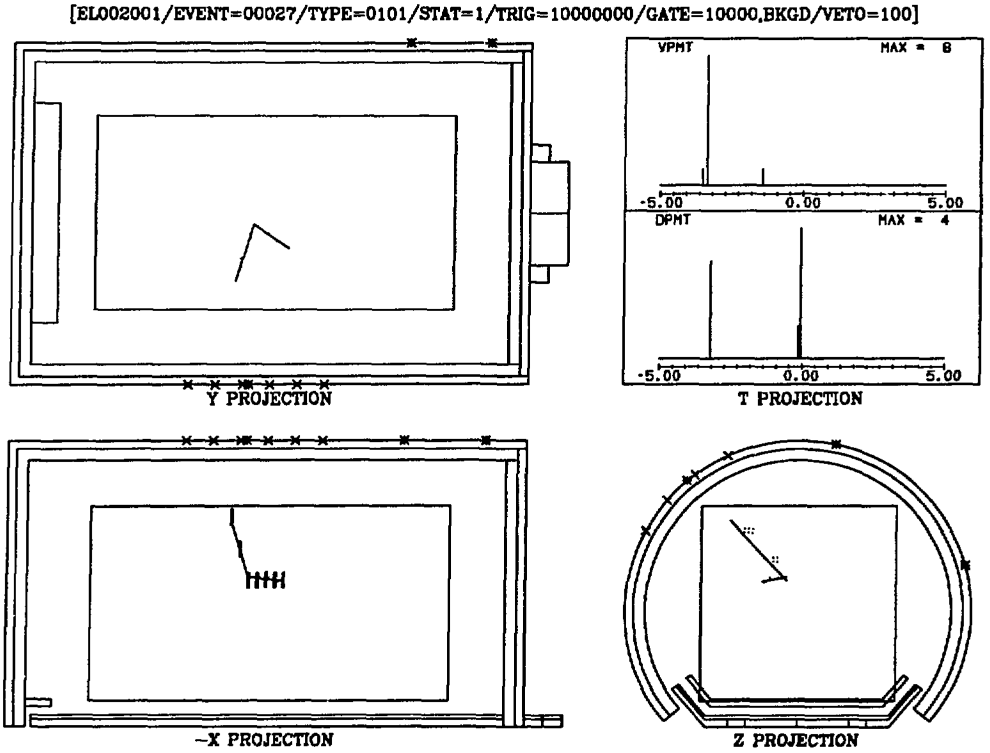

Figure 4.9: One event display of a stop muon event. The track, which is completely contained in the central detector, triggered the event and is the "electron." The other track, which appears to have entered the central detector, is the "muon." The time history shows that the "muon" precedes the "electron" by 3.2μs and that the "muon" is observed by both the active shield and in the central detector.

given in Appendix A.

We use three tagged ^{252}Cf neutron sources to provide the slow neutron control sample. Each tagged source consists of a parallel plate ion chamber with one plate coated with $\approx$ 0.8 nCi of ^{252}Cf. The spontaneous fission (SF) of ^{252}Cf results in the emission of an average of 3.74 neutrons [56], and the detection of the fission fragments with the ion chamber tags the neutrons.

4.3.2 Electron Monte Carlo

The response of the detector to electrons and photons is modeled with the EGS4 Monte Carlo code [57], which uses the E645 detector survey, composition, energy

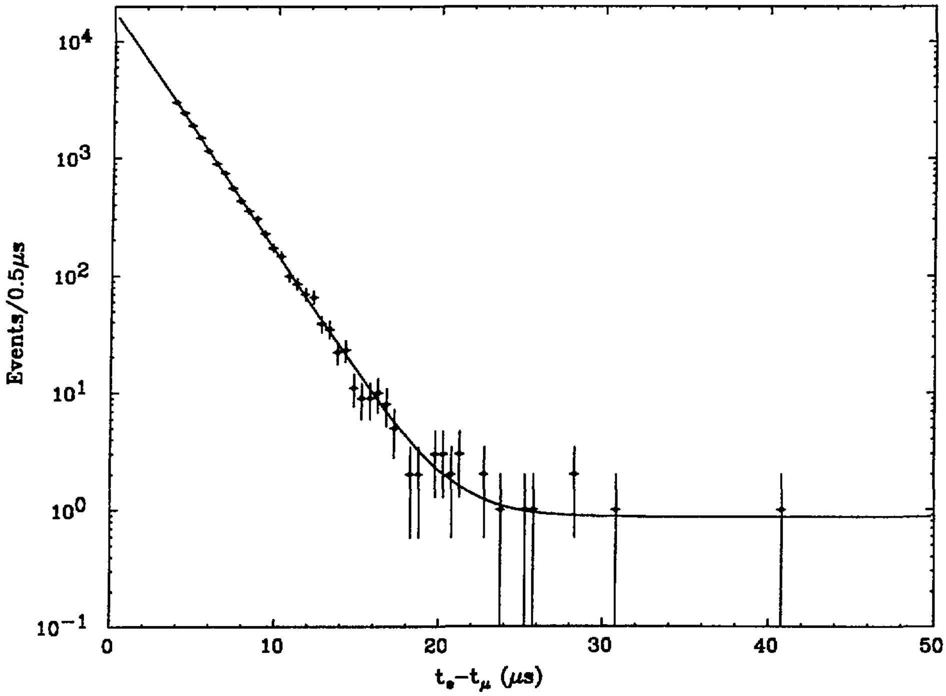

Figure 4.10: Distribution of $(t_e - t_\mu)$ for stop muon decay events. The solid line is the result of a fit to the interval $(t_e - t_\mu) \geq 3.5\mu s$, which yields a muon mean lifetime of $\tau = 2.10 \pm 0.02\mu s$. The online Short Veto suppresses the events with $(t_e - t_\mu) < 3.5\mu s$.

scale calibration, and thresholds. As a test, we simulate the decay electrons from muons stopped in the detector and make a comparison with the control sample. In Figure 4.11, we compare the scintillator dE/dx of the EGS4 Monte Carlo to data. The top figure compares the raw EGS4 simulation to the data, showing very poor agreement. We increase the width of the curve by folding in photostatistics, where an empirically determined value of 23.5 photoelectrons for a minimum ionizing particle is used. The bottom figure gives the EGS4 simulation with photostatistics, which is in excellent agreement with the data. All subsequent EGS4 Monte Carlo simulations have photostatistics. In Figure 4.12 we compare the Michel spectrum, i.e., the visible energy E_{vis} distribution of the electrons from stop muon decay, from

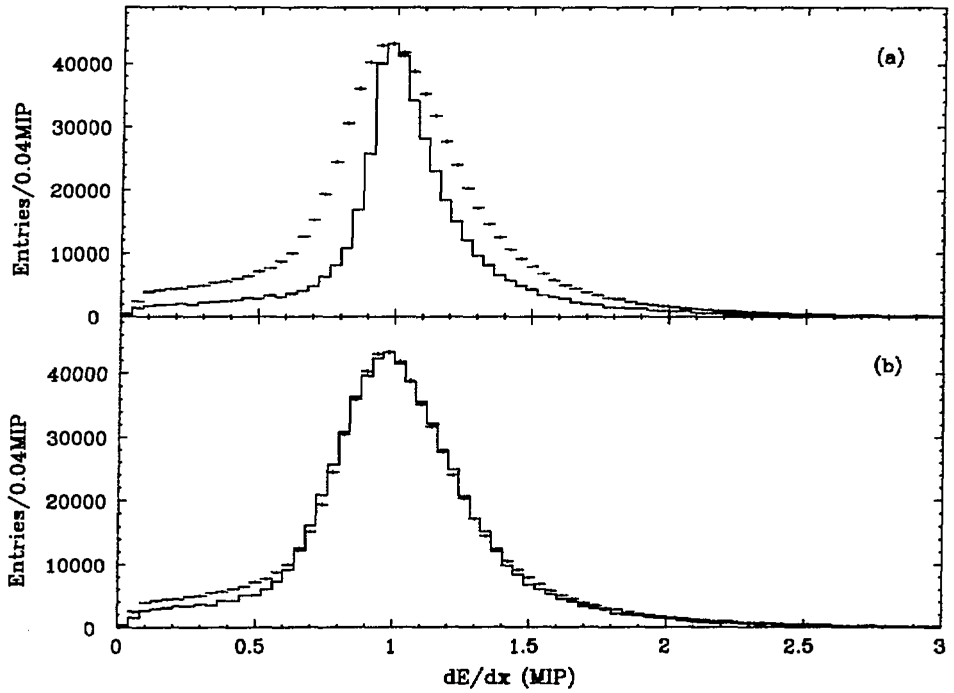

Figure 4.11: The dE/dx distribution of electrons from the decay of cosmic ray muons that stop in the detector, showing a comparison of the data (points) to an EGS4 Monte Carlo simulation (histogram). (a) Raw EGS4 Monte Carlo. (b) EGS4 Monte Carlo with photostatistics (23.5 photoelectrons). In both (a) and (b), the Monte Carlo and the data have equal peaks.

the EGS4 Monte Carlo to data. The agreement with the data is also very good.

4.3.3 Slow Neutron Monte Carlo

We use a locally developed Monte Carlo code to model slow neutrons (thermal to 10 MeV) in the E645 detector. The neutron Monte Carlo code uses the E645 detector survey and composition to transport neutrons between interactions, where the allowed neutron interactions are elastic scattering off of hydrogen, carbon, oxygen, and aluminum; and radiative capture on hydrogen and gadolinium. Cross sections for the above interactions have been compiled as curves [58]. The exception is neutron radiative capture on hydrogen for which the inverse velocity law [59] is used.

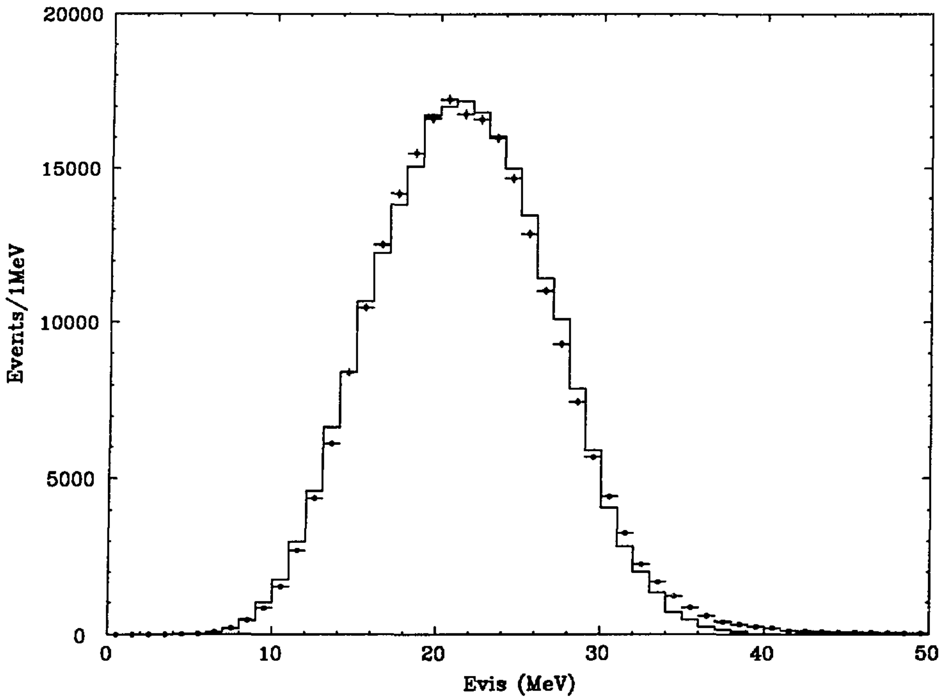

Figure 4.12: The E_{vis} distribution of electrons from the decay of cosmic ray muons that stop in the detector, showing a comparison of the data (points) to the EGS4 Monte Carlo simulation (histogram). The Monte Carlo and the data have an equal number of events.

The neutron transport continues until either the neutron escapes the detector or the neutron is captured.

The neutron elastic scattering is modeled by giving the target an initial thermal energy (temperature T = 25 °C) and a random direction in the laboratory frame. We assume that the scattering is pure s-wave so that the final direction of the neutron is isotropic in the center of mass frame. Transformation back to the laboratory frames gives the final direction neutron direction in the laboratory frame and the conservation of energy-momentum gives the final energy of the neutron. For neutron elastic scattering on hydrogen at low energies (< 10 eV), molecular binding effects become important and the target hydrogen nucleus may no longer be considered free. This increases the number of scatters required to thermalize the neutron. We

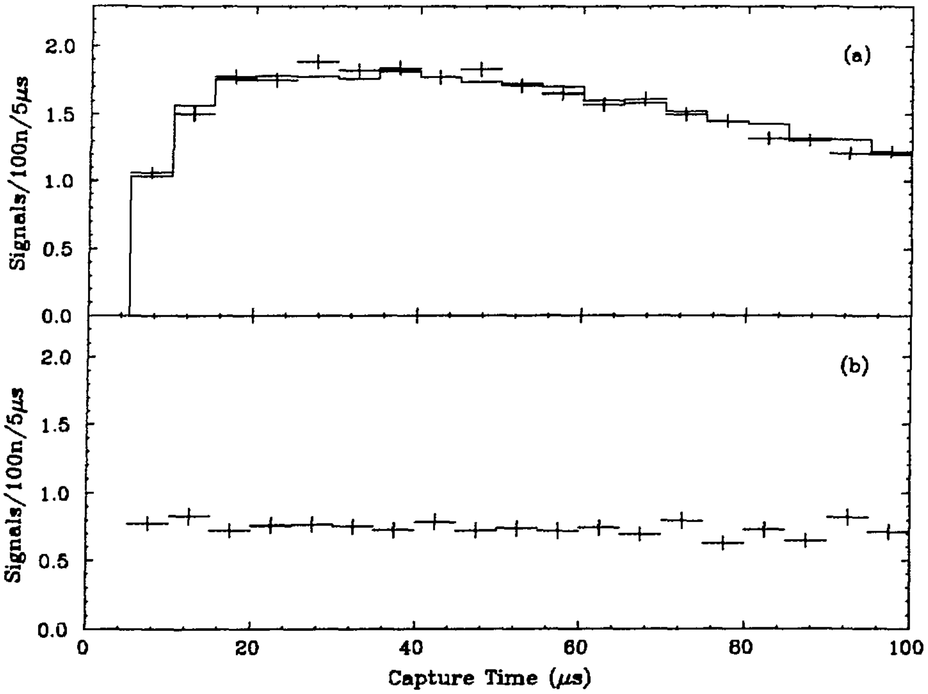

Figure 4.13: Slow neutron capture time. (a) Background subtracted tagged neutron source events (points) compared to the Monte Carlo simulation (histogram). (b) Background events from the random trigger.

crudely model this effect by making the hydrogen target heavier at neutron energies below 10 eV. The capture time distribution of neutrons from the ^{252}Cf tag source is given in Figure 4.13. The excellent agreement of the Monte Carlo with the tag source data shows that this crude approximation works.

This Monte Carlo code allows the neutron to be visible only through the detection of the photons from radiative capture. The visible energy of the recoil targets is relatively small and is not recorded. Radiative neutron capture on natural gadolinium occurs primarily on ^{155}Gd (18.4%) and ^{157}Gd (81.6%). The total photon energy is 8.5 MeV for capture on ^{155}Gd and 7.9 MeV for capture on ^{157}Gd. The photon spectra and multiplicity distribution for capture on ^{155}Gd is modeled by generated 10,000 photon energies according to measured capture spectra [60]. These photon

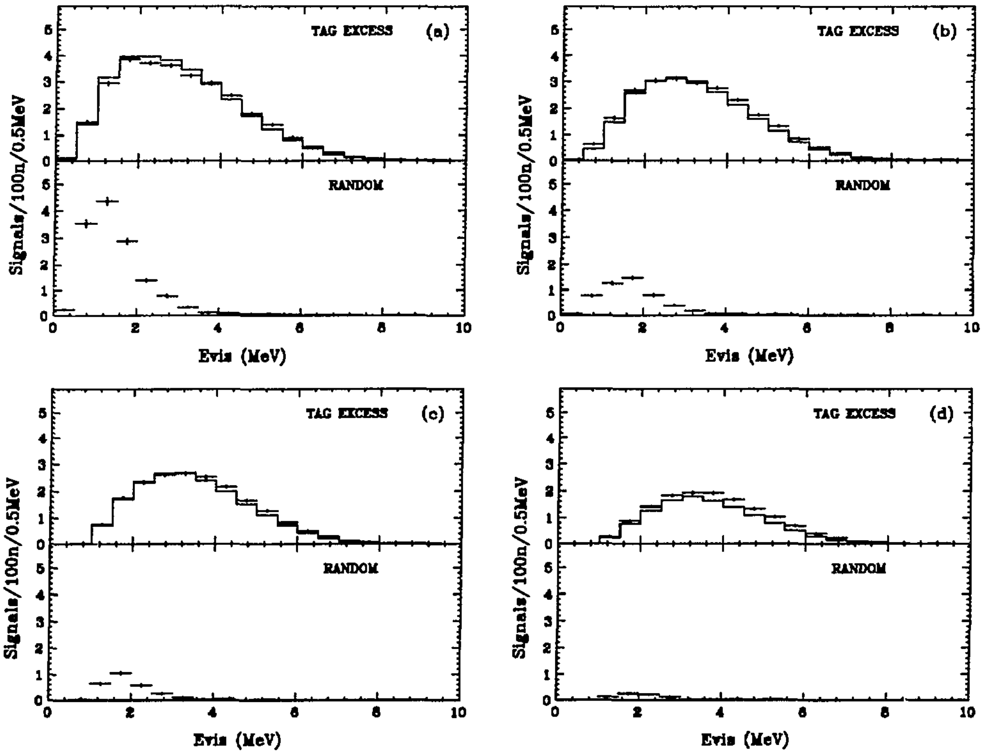

Figure 4.14: E_{vis} distributions for radiative neutron Gd-capture with the data (points) compared to the Monte Carlo (histogram). (a) Multiplicity 1A1X. (b) Multiplicity 1A2X. (c) Multiplicity 2A0X. (d) Multiplicity 2A1X. In addition to the above multiplicity all signatures require that the time of the signal is within the window $[5, 100)\mu s$, the visible energy $E_{vis} < 10$MeV, and the position of the signal is less than 150cm from the neutron source.

energies are randomly sorted into groups where the total energy in the group equals to 8.5 MeV with a ±0.5MeV tolerance. The photon energies in a group are equivalent to a neutron ^{155}Gd capture event. Neutron capture on ^{157}Gd is modeled with an identical procedure. The photon from radiative neutron capture on hydrogen is simply mono-energetic with energy $E_\gamma = 2.225$MeV. The EGS4 Monte Carlo described above is used to transport the photons from radiative neutron capture.

We use the neutron Monte Carlo code to simulate the neutrons that result from ^{252}Cf spontaneous fission. In Table 4.1, we compare the raw neutron detection efficiencies of the Monte Carlo simulation to the data for various radiative neutron

Multiplicity	Data ϵ_n	M.C. ϵ_n	a_n
1A	0.398	0.421	0.426
1A1X or 2A	0.297	0.298	0.141
1A2X or 2A	0.243	0.229	0.053
2A	0.196	0.186	0.029
2A1X or 3A	0.139	0.117	0.009

Table 4.1: Slow neutron detection efficiencies for the various multiplicity signatures (A = AND, X = XOR). The radiative capture signatures also require that the time of the signal is within the window $[5, 100)\mu s$, the visible energy $E_{vis} < 10$MeV, and the position of the signal is less than 150cm from the neutron source. The efficiencies of the tagged ^{252}Cf source data is compared to the Monte Carlo.

capture signatures. The agreement of the Monte Carlo with the data is within ±5%, with the exception of the signature with the multiplicity threshold "2A1X or 3A" where there is a 20% discrepancy. This may be due to the uncertainty in the measured radiative capture spectrum at low photon energies [60] . We compare the visible energy, E_{vis}, of the Monte Carlo simulation to the data for various multiplicity signatures in Figure 4.14. The agreement is very good.

4.3.4 Neutrino Monte Carlo

We use a neutrino Monte Carlo to predict the number of neutrino interactions in the central detector. The neutrino Monte Carlo begins by generating isotropically distributed neutrinos in the center of the LAMPF A-6 beam stop. Using information from both the LAMPF survey [69] and the E645 detector survey, the neutrinos are transported until they either hit or miss the central detector. All neutrinos that miss the central detector are discarded. The remaining neutrinos are transported through the central detector where T, the total number of neutrino targets per cm^2 along the neutrino vector from entry to exit, is counted. This transport takes into account the non-uniform target density of the detector. The neutrino interaction point, $\vec{x}$, is generated such that the number of targets per cm^2 from the neutrino entry point to $\vec{x}$ is uniform from zero to T. Final state particles, i.e. electrons, positrons, and neutrons from the neutrino interactions are generated at $\vec{x}$ with the appropriate distributions. Each neutrino interaction is assigned a weight that depends upon N - the total number of neutrinos generated, T - the number of neutrino targets per cm^2, and the cross section of the neutrino interaction. The weights are defined such that the predicted number of neutrino interactions, Y, is equal to

$$Y = \frac{r_\pi \cdot Q}{1.602 \times 10^{-19}} \sum_i w_i \tag{4.12}$$

where r$_\pi$ is the average number of π^+ decays per incident beam proton and Q is the integrated proton charge on the A-6 beam stop. For neutrino oscillation events, the weights also depend upon the oscillation parameters.

The weight assignment for each type of neutrino interaction is discussed below.

$\bar{\nu}_e$p Charge Current Reactions

The $\bar{\nu}_e$, which may arise from $\bar{\nu}_\mu, \nu_e, \nu_\mu \rightarrow \bar{\nu}_e$ oscillations or rare $\mu^+ \rightarrow e^+ \bar{\nu}_e \nu_\mu$ decay, is detected through the $\bar{\nu}_e$p CC reaction

$$\bar{\nu}_e + \mathrm{p} \rightarrow \mathrm{n} + e^+ \tag{4.13}$$

The differential cross section, d$\sigma(\bar{\nu}_e$p)/dΩ_e, for the $\bar{\nu}_e$p CC reaction has been calculated for LAMPF neutrino energies [63,64]. The weight assignment for each $\bar{\nu}_e$ appearance mode is given below.

$\bar{\nu}_\mu \rightarrow \bar{\nu}_e$ Oscillations The neutrino energy, E$_\nu$, is generated according to the dN$_{\bar{\nu}_\mu}$/dE$_\nu$ distribution given in Equation 3.7. The final state positron, from the $\bar{\nu}_e$p CC reaction, is generated isotropically with respect to the neutrino vector at $\vec{x}$. The initial positron energy and the initial neutron energy and direction is determined through the conservation of 4-momentum. The differential cross section, d$\sigma(\bar{\nu}_e$p)/dΩ_e, for this interaction is evaluated at the initial positron direction and at E_ν. This interaction is assigned the weight,

$$w = \sin^2(2\theta_{\bar{\mu}\bar{e}}) \sin^2(1.27\frac{\delta m^2_{\bar{\mu}\bar{e}} L}{E_\nu}) \frac{4\pi T}{N} \frac{d\sigma}{d\Omega_e}(\bar{\nu}_e p) \tag{4.14}$$

where $\sin^2(2\theta_{\bar{\mu}\bar{e}})$ and $\delta m^2_{\bar{\mu}\bar{e}}$ are the $\bar{\nu}_\mu \rightarrow \bar{\nu}_e$ oscillation parameters and L is the distance from the A-6 beam stop to $\vec{x}$.

$\nu_e \rightarrow \bar{\nu}_{eL}$ **Oscillations** The neutrino energy, E_ν, is generated according to the dN_{ν_e}/dE_ν distribution given in Equation 3.6. The final state positron, from the $\bar{\nu}_e$p CC reaction, is generated isotropically with respect to the neutrino vector at $\vec{x}$. The initial positron energy and the initial neutron energy and direction is determined through the conservation of 4-momentum. The differential cross section, $d\sigma(\bar{\nu}_e p)/d\Omega_e$, for this interaction is evaluated at the initial positron direction and at E_ν. This interaction is assigned the weight,

$$w = \alpha^2 \sin^2(2\theta_{e\bar{e}}) \sin^2(1.27\frac{\delta m^2_{e\bar{e}} L}{E_\nu}) \frac{4\pi T}{N} \frac{d\sigma}{d\Omega_e}(\bar{\nu}_e p) \tag{4.15}$$

where $\sin^2(2\theta_{e\bar{e}})$ and $\delta m^2_{e\bar{e}}$ are the $\nu_e \rightarrow \bar{\nu}_{eL}$ oscillation parameters, $\alpha^2 \equiv \sigma(\bar{\nu}_{eL}p)/\sigma(\bar{\nu}_{eR}p)$ is the V+A $\bar{\nu}_e$p CC cross section relative to the V-A $\bar{\nu}_e$p CC cross section, and L is the distance from the A-6 beam stop to $\vec{x}$.

$\nu_\mu \rightarrow \bar{\nu}_{eL}$ **Oscillations** The neutrino energy is mono-energetic with energy E_ν = 29.8MeV. The final state positron, from the $\bar{\nu}_e$p CC reaction, is generated isotropically with respect to the neutrino vector at $\vec{x}$. The initial positron energy and the initial neutron energy and direction is determined through the conservation of 4-momentum. The differential cross section, $d\sigma(\bar{\nu}_e p)/d\Omega_e$, for this interaction is evaluated at the initial positron direction and at E_ν. This interaction is assigned the weight,

$$w = \alpha^2 \sin^2(2\theta_{\mu\bar{e}}) \sin^2(1.27\frac{\delta m^2_{\mu\bar{e}} L}{E_\nu}) \frac{4\pi T}{N} \frac{d\sigma}{d\Omega_e}(\bar{\nu}_e p) \tag{4.16}$$

where $\sin^2(2\theta_{\mu\bar{e}})$ and $\delta m^2_{\mu\bar{e}}$ are the $\nu_\mu \rightarrow \bar{\nu}_{eL}$ oscillation parameters, $\alpha^2 \equiv \sigma(\bar{\nu}_{eL}p)/\sigma(\bar{\nu}_{eR}p)$ is the V+A $\bar{\nu}_e$p CC cross section relative to the V-A $\bar{\nu}_e$p CC cross section, and L is the distance from the A-6 beam stop to $\vec{x}$.

Rare $\mu^+ \rightarrow e^+\bar{\nu}_e\nu_\mu$ Decay The neutrino energy, E$_\nu$, is generated according to the anti-neutrino distribution from μ^+ decay, which is equal to the dN$_{\bar{\nu}_\mu}$/dE$_\nu$ distribution given in Equation 3.7. The final state positron, from the $\bar{\nu}_e$p CC reaction, is generated isotropically with respect to the neutrino vector at $\vec{x}$. The initial positron energy and the initial neutron energy and direction is determined through the conservation of 4-momentum. The differential cross section, d$\sigma(\bar{\nu}_e$p)/dΩ_e, for this interaction is evaluated at the initial positron direction and at E$_\nu$. This interaction is assigned the weight,

$$w = R\frac{4\pi T}{N}\frac{d\sigma}{d\Omega_e}(\bar{\nu}_e p) \tag{4.17}$$

where

$$R = \frac{\Gamma(\mu^+ \rightarrow e^+\bar{\nu}_e\nu_\mu)}{\Gamma(\mu^+ \rightarrow all)} \tag{4.18}$$

is the branching ratio of the rare μ^+ decay mode.

ν_en Charged Current Reactions

The dominant ν_en CC reactions in the central detector are

$$\nu_e +^{12}\mathrm{C} \rightarrow X + e^- \tag{4.19}$$

$$\nu_e +^{13}\mathrm{C} \rightarrow X + e^- \tag{4.20}$$

$$\nu_e +^{16}\mathrm{O} \rightarrow X + e^- \tag{4.21}$$

$$\nu_e +^{27}\mathrm{Al} \rightarrow X + e^- \tag{4.22}$$

where X represents a possibly final state nucleus. The electron is generated isotropically with respect to the neutrino vector at $\vec{x}$ with uniform kinetic energy from zero to E$_{max} - \Delta$, where E$_{\text{max}}$ = 52.8MeV is the ν_e endpoint energy and Δ is the ground state mass difference of the initial and final nuclei. These events are assigned the weight,

$$w = \frac{4\pi T}{N}\frac{d^2\bar{\sigma}}{dE_e d\Omega_e}(\nu_e n) \tag{4.23}$$

where

$$\frac{d^2\bar{\sigma}}{dE_e d\Omega_e}(\nu_e n) = \int dE_\nu \frac{dN_{\nu_e}}{dE_\nu}\frac{d^2\sigma}{dE_e d\Omega_e}(\nu_e n) \tag{4.24}$$

is the differential neutrino cross section averaged over the ν_e energy spectrum. The average differential cross section, $d^2\bar{\sigma}(\nu_e n)/dE_e d\Omega_e$, has been computed for ^{12}C and ^{16}O [65]. We use a parameterization of these cross sections given in [66]. For the ^{13}C and ^{27}Al cross sections, we use an extrapolation of the $\nu_e{}^{12}$C parameterization that is also given in [66].

νe^- Elastic Scattering

The neutrino-electron elastic scattering reactions are:

$$\nu_\mu + e^- \rightarrow \nu_\mu + e^- \tag{4.25}$$

$$\nu_e + e^- \rightarrow \nu_e + e^- \tag{4.26}$$

$$\bar{\nu}_\mu + e^- \rightarrow \bar{\nu}_\mu + e^- \tag{4.27}$$

The neutrino energy for interaction 4.25 is mono-energetic with $E_\nu = 29.8$MeV. The neutrino energy for interaction 4.26 is generated according to the dN_{ν_e}/dE_ν distribution given in Equation 3.6 and the neutrino energy for interaction 4.27 is generated according to the $dN_{\bar{\nu}_\mu}/dE_\nu$ distribution given in Equation 3.7. The electron kinematic parameter $y \equiv E_e/E_\nu$ is generated uniformly from zero to $y_{\mathrm{max}} \equiv E_{\mathrm{max}}/E_\nu$. Here, E_e is the kinetic energy of the recoil electron and E_{max} is the maximum kinetic energy of the recoil electron given by

$$E_{max} = \frac{E_\nu}{1 + \frac{m_e}{2E_\nu}} \tag{4.28}$$

where $m_e = 0.511$MeV is the electron rest mass. The polar direction of the recoil electron is determined through the conservation of 4-momentum and the azimuthal direction is uniformly generated. These events are assigned the weight,

$$w = \frac{T}{N}\frac{d\sigma}{dy}(\nu e^-) \tag{4.29}$$

The explicit form of the differential cross section, $d\sigma(\nu e^-)/dy$ is given in [67].

4.3.5 Synthetic Neutrino Data

Synthetic neutrino data is generated from the neutrino Monte Carlo, the electron Monte Carlo, the neutron Monte Carlo, and real Beam Gate random trigger events. Final state electrons (e^+ and e^-) and neutrons from neutrino interactions are generated by the neutrino Monte Carlo. These particles are transported through the central detector with the electron Monte Carlo and the neutron Monte Carlo, respectively. The transport results in PMT and PDT signal time and pulse height information. All Monte Carlo events that fail to satisfy the online trigger condition are discarded. The remaining events are installed into the analysis database format and superimposed on real Beam Gate random trigger events. The synthetic neutrino data is the resultant concoction of Monte Carlo and random trigger data.

The synthetic neutrino data contains PMT and PDT signal time and pulse height information with the correct thresholds and energy scale corresponding to electrons (e^+ and e^-) and neutrons with the correct temporal, energy, spatial, and angular distributions as predicted by the neutrino interaction cross sections. The synthetic neutrino data also contain random "noise," which was introduced by real random trigger data. Therefore, the synthetic neutrino data is a proper representation of the predicted neutrino events and may be used in estimating neutrino detection efficiencies and predicting neutrino yields.

Chapter 5

Data Analysis

5.1 Overview

LAMPF E645 acquired beam data from June to December 1987 during LAMPF cycles 48, 49, and 50. A total of 1.26×10^6 triggers were accepted during a live time of 368.6 LD, where 1 LD (LAMPF Day) $\equiv$ 5600 seconds is the approximate beam time in a 24 hour day given a 6.5% duty factor. The breakdown of the events into the individual gates is given in the run summary in Table 5.1. The Beam Gate live time of 81.4 LD represents a total of 5527.7 coulombs of integrated proton charge on the A-6 beam stop.

We search the 1987 data for $\bar{\nu}_e$ appearance candidates. This search begins by selecting events that are both tracked and contained in the fiducial volume of the central detector. Events that appear to be induced by cosmic ray muons, based

	Live Time	Events
Beam Gate	81.4 LD	276452
Pre-Beam Gate	184.1 LD	633727
Post-Beam Gate	103.1 LD	352136
Total	368.6 LD	1262315

Table 5.1: 1987 run summary.

on signals in the active shield or the central detector, are removed. A particle identification technique is then employed on the surviving tracks to remove events that are not electrons (either e^+or e^-). Events that appear to be the result of DIF ν_μn and $\bar{\nu}_\mu$p CC interactions are also removed. These tests are made on the data in three passes: Pass-1, Pass-2, and Pass-3, which are described in detail below. All events that survive these tests constitute the neutrino sample. A final pass, Pass-4, is made on the neutrino sample to identify the events that have delayed neutron coincidences.

In addition to the $\bar{\nu}_e$ appearance events, we also make a search of the 1987 data for possible beam associated backgrounds that are proton-like, photon-like, and DIF neutrino-like in character. The topology of these events and the details of the search are discussed below.

5.2 Pass-1

The Pass-1 analysis performs the Track tests, the Fiducial Volume tests, and the cosmic ray muon removal. The cosmic ray muon removal consists of two tests, the Short Veto, which rejects direct muon interactions, and the Long Veto, which rejects electrons from muon decay. The online Short Veto and Long Veto complement their offline counterparts. These tests and the results of the Pass-1 analysis are discussed below.

A search for proton-like events is also performed in the Pass-1 analysis. This search is discussed below.

5.2.1 Track

The Track tests, Track-1 and Track-2, require that a "clean" charged particle track is found in the trigger time slice. These tests are described below.

Track-1 Reject an event if the trigger time slice does not contain at least one charged particle track that is reconstructed in both the x-profile and y-profile. This test ensures that the track endpoints and direction cosines are known in three dimensions.

Track-2 Reject an event if the trigger time slice does not contain at least one charged particle track that satisfies all of the following conditions:

1. The track must contain at least two scintillator planes, at least two XPDT planes, and at least two YPDT planes. This test ensures that the track provides at least two samples of scintillator dE/dx and four samples of PDT dE/dx.
2. The z-direction cosine of the track must satisfy $\cos\theta_z \geq 0.4$. From Figure 4.5, this condition ensures that approximation for E_{PROB} given in Equation 4.2 is correct to within ±2% for the scintillators and ±4% for the PDTs.

5.2.2 Fiducial Volume

The Fiducial Volume tests require that events must be completely contained in the central detector. This ensures that the total energy of the event can be measured and that possible background sources of the event are visible.

The Fiducial Volume is defined by the tests listed below:

1. Reject an event if the trigger time slice contains one or more scintillators, XPDTs, or YPDTs on the first or last detector plane. This test is designed to remove events that may have entered (or exited) the central detector through the front or the back.
2. Reject an event if the trigger time slice contains one or more tracks that have an endpoint that is within 15.24cm (1/2 height of a Scintillator panel) from

the edge of the central detector in the x or y direction. This test is designed to remove events that may have entered (or exited) the central detector through the sides.

3. Reject an event if the trigger time slice contains one or more tracks that have an external endpoint that is within 7.62cm from the edge of the central detector in the x or y direction. The external endpoints of a track are defined to be the projection of the track onto the next scintillator plane. This test compliments the above test by removing events with small $\cos\theta_z$ tracks near the edge of the central detector.

5.2.3 Short Veto

The following offline Short Vetoes test events for prompt activity in the active shield. These vetoes are designed, primarily, to reject cosmic ray muon triggers and, to a much lesser degree, photon and neutron triggers. The offline Short Vetoes compliment the online Short Vetoes by taking advantage of the spatial and pulse height information of the shield PMTs that were unavailable online. The four Short Veto tests are described in detail below.

ShortVeto-1 The event is rejected if the trigger track is spatially correlated to a cluster containing one or more shield PMTs in the time window $[-0.40, 0.25)\mu$s relative to the trigger. The spatial correlation requires that the centroid of the shield PMT cluster be within 200cm (perpendicular projection) of the line defined by the trigger track. The ShortVeto-1 test is designed to remove cosmic ray muons and neutrons that interact in the active shield before leaving pristine tracks in the central detector.

ShortVeto-2 The event is rejected if the trigger track is spatially correlated to a cluster containing one or more shield PMTs in the time window $[-0.40, 0.25)\mu$s relative to the trigger. The spatial correlation requires that the centroid of the

Section	Cycle 48 Threshold	Cycles 49-50 Threshold
Front Wall	$m \geq 2$ and $v \geq 1$	$m \geq 2$ and $v \geq 1$
Back Wall	$m \geq 2$ and $v \geq 1$	$m \geq 2$ and $v \geq 1$
Rim	$m \geq 1$ and $v \geq 1$	$m \geq 1$ and $v \geq 1$
Cylinder	$m \geq 2$ and $v \geq 1$ $m \geq 1$ and $v \geq 20$	$m \geq 2$ and $v \geq 1$ $m \geq 1$ and $v \geq 25$
Bottom	$m \geq 1$ and $v \geq 15$	$m \geq 1$ and $v \geq 20$

Table 5.2: Shield PMT cluster multiplicity (m) and sum pulse height (v) thresholds for ShortVeto-4. Note that there are different thresholds for LAMPF cycles 48 and 49-50. This is to take into account the pulse height gains in the digitized PMT signals that are the result of modifications made to the shield electronics hardware during the beam off period between LAMPF cycles 48 and 49.

shield PMT cluster be within 10g/cm^2 of detector material from the endpoint of the trigger track. The ShortVeto-2 test is designed to remove cosmic ray events that may involve a neutral particle (photon or neutron).

ShortVeto-3 The event is rejected if the trigger track is spatially correlated to a cluster containing one or more shield PMTs in the time window $[-0.40, 0.25)\mu$s relative to the trigger. The spatial correlation requires that $|z_{\mathrm{END}} - z_{\mathrm{PMT}}| <$ 150cm where z_{END} is the z-coordinate of a trigger track endpoint and z_{PMT} is the z-coordinate of the shield PMT cluster. The ShortVeto-3 test is designed to remove cosmic ray events that may involve a vertical charged particle track in the dead regions of the central detector.

ShortVeto-4 The event is rejected if there is a shield PMT cluster in the time window $[-0.40, 0.25)\mu$s relative to the trigger. The shield PMT cluster must satisfy the multiplicity and pulse height thresholds given in Table 5.2. These thresholds are set by the "noise" level in the active shield as determined by the random trigger events. The ShortVeto-4 test is designed to remove cosmic ray events that may involve a neutral particle (photon or neutron).

5.2.4 Long Veto

The following offline "long" vetoes are designed to remove non-neutrino background electron events that result from muon decay. These background events include the decay of stopping cosmic ray muons, which is the major contributor, the decay of spallation products left in the wake of inelastically scattering cosmic ray muons, and cosmic ray hadron induced pion production. These vetoes are divided into nine tests that are described in detail below.

LongVeto-1 This veto is enabled when all of the following conditions are met:

1. The triggered event is preceeded by a "muon" track, which passes within 100cm of a trigger track endpoint. The "muon" track must be reconstructed in both the x-profile and the y-profile.
2. The "muon" track is temporally ($\pm 0.5\mu s$) and spatially correlated with a shield PMT cluster. The spatial correlation requires that the centroid of the shield PMT cluster be within 200cm (perpendicular projection) of the line defined by the "muon" track. If there is more than one spatially correlated shield PMT cluster, then orientation of these clusters must be topologically consistent with a stopping muon (all of the spatially correlated clusters must be at one endpoint of the "muon" track).

All events that are preceeded by this veto are rejected. This veto is designed to remove stopping cosmic ray muons where the muon leaves a pristine track in the central detector.

LongVeto-2 This veto is enabled when all of the following conditions are met:

1. The triggered event is preceeded by a "muon" track whose endpoint is within one detector plane of a trigger track endpoint.
2. The "muon" track is temporally ($\pm 0.5\mu s$) correlated with a shield PMT cluster.

3. All elements of the "muon" track lie (within tolerances given by the physical size of the scintillator panels and PDT wire spacing) on the line defined by the projection of the trigger track onto the "muon" track endplane and the centroid of the shield PMT cluster.

All events that are preceeded by this veto are rejected. This veto is designed to remove stopping cosmic ray muons where the muon has a very steep (small $\cos\theta_z$) track.

LongVeto-3 This veto is enabled when all of the following conditions are met:

1. The triggered event is preceeded by a spatially correlated "muon," where the "muon" is simply a single scintillator panel. The spatial correlation requires that the "muon" is within one detector plane of a trigger track endpoint and that the projection of the trigger track onto the "muon" plane lies within the physical boundaries of the scintillator panel.
2. The "muon" is temporally ($\pm 0.5\mu s$) correlated with a shield PMT cluster.

All events that are preceeded by this veto are rejected. This veto is designed to remove stopping cosmic ray muons where the muon interacts in a single scintillator panel.

LongVeto-4 This veto is set when all of the following conditions are met:

1. The triggered event is preceeded by a detector time slice that contains more than one "muon" track that is reconstructed in both the x-profile and the y-profile. One of the "muon" tracks must pass within 100cm of a trigger track endpoint.
2. Each "muon" track must have temporally ($\pm 0.5\mu s$) and spatially correlated shield PMT clusters at both endpoints. The spatial correlation requires that the centroid of the shield PMT cluster be within 200cm (perpendicular projection) of the line defined by the "muon" track.

All events preceeded by this veto within 15μs are rejected. This veto is designed to remove stopping cosmic ray muons, where there are multiple muons involved. Multiple muon events are not removed by LongVeto-1 if the multiple muons confuse the stop muon topology.

LongVeto-5 This veto is set when all of the following conditions are met:

1. The triggered event is preceeded by a "muon" track whose endpoint comes within 50cm of a trigger track endpoint in either the x-profile or the y-profile.
2. The "muon" track must be temporally ($\pm 0.5\mu$s) correlated with a shield PMT cluster.

All events preceeded by this veto within 25μs are rejected. This veto is designed to remove stopping cosmic ray muon that was not removed by LongVeto-1 due to an error in the reconstruction of the "muon" track.

LongVeto-6 This veto is set when all of the following conditions are met:

1. The triggered event is preceeded by a "muon" track that is reconstructed in both the x-profile and the y-profile. The "muon" track must have one endpoint inside and one endpoint outside the fiducial volume of the central detector.
2. The "muon" track is temporally ($\pm 0.5\mu$s) and spatially correlated with a shield PMT cluster. The spatial correlation requires that the centroid of the shield PMT cluster be within 200cm (perpendicular projection) of the line defined by the "muon" track. In addition, the shield PMT cluster must be nearer to the "muon" track endpoint that is outside the fiducial volume (so that the "muon" track is topologically consistent with a muon stopping in the fiducial volume).

All events preceeded by this veto within 25μs are rejected. This veto is designed to remove events that result from the electron bremsstrahlung following the decay of cosmic ray muons that stop in the central detector.

LongVeto-7 This veto is set when all of the following conditions are met:

1. The triggered event is preceeded by a "muon" track that passes within 200cm of a trigger track endpoint. The "muon" track must be reconstructed in both the x-profile and the y-profile.
2. The "muon" track is temporally ($\pm 0.5\mu$s) and spatially correlated with at least two shield PMT clusters. The spatial correlation requires that the centroid of the shield PMT cluster be within 200cm (perpendicular projection) of the line defined by the "muon" track. The orientation of the clusters must be consistent with a muon that passes completely through the detector (there must be a cluster at each endpoint of the "muon" track).

All events preceeded by this veto within 15μs are rejected. This veto is designed to remove $\pi^\pm \rightarrow \mu^\pm \rightarrow e^\pm$ decay events where the pion is a spallation product from an inelastic cosmic ray muon interaction.

LongVeto-8 This veto is set when all of the following conditions are met:

1. The triggered event is preceeded by a detector time slice that has a minimum visible energy of 50 MeV and a shower density of 1.75 scintillators panels/plane.
2. The time slice is temporally ($\pm 0.5\mu$s) correlated with a shield PMT cluster.

All events preceeded by this veto within 25μs are rejected. This veto is designed to remove $\pi^\pm \rightarrow \mu^\pm \rightarrow e^\pm$ decay events where the pion is the product

Section	Cycle 48 Threshold	Cycles 49-50 Threshold
Front Wall	m $\geq$ 3 and v $\geq$ 1	m $\geq$ 4 and v $\geq$ 1
Back Wall	m $\geq$ 3 and v $\geq$ 1	m $\geq$ 4 and v $\geq$ 1
Rim	m $\geq$ 3 and v $\geq$ 1	m $\geq$ 3 and v $\geq$ 1
Cylinder	m $\geq$ 3 and v $\geq$ 1 —	m $\geq$ 4 and v $\geq$ 1 m $\geq$ 3 and v $\geq$ 40
Bottom	m $\geq$ 1 and v $\geq$ 30	m $\geq$ 1 and v $\geq$ 40

Table 5.3: Shield PMT cluster multiplicity (m) and pulse height (v) thresholds for LongVeto-9. Note that there are different thresholds for LAMPF cycles 48 and 49-50. This is to take into account the pulse height gains in the digitized PMT signals that are the result of modifications made to the shield electronics hardware during the beam off period between LAMPF cycles 48 and 49.

from an inelastic interaction of an energetic cosmic ray hadron. The inelastic interaction results in many particles that contribute to the large visible energy.

LongVeto-9 This veto is set when all of the following conditions are met:

1. The triggered event is preceeded by a shield PMT cluster that satisfies the multiplicity and pulse height thresholds given in Table 5.3. These thresholds are set by the "noise" level in the active shield as determined by the random trigger events.
2. The centroid of the shield PMT cluster must be less than 100g/cm^2 of detector material from a trigger track endpoint.

All events preceeded by this veto within 20μs are rejected. This veto is designed to remove events that result from electron bremsstrahlung emitted following the decay of a cosmic ray muon in the passive shield.

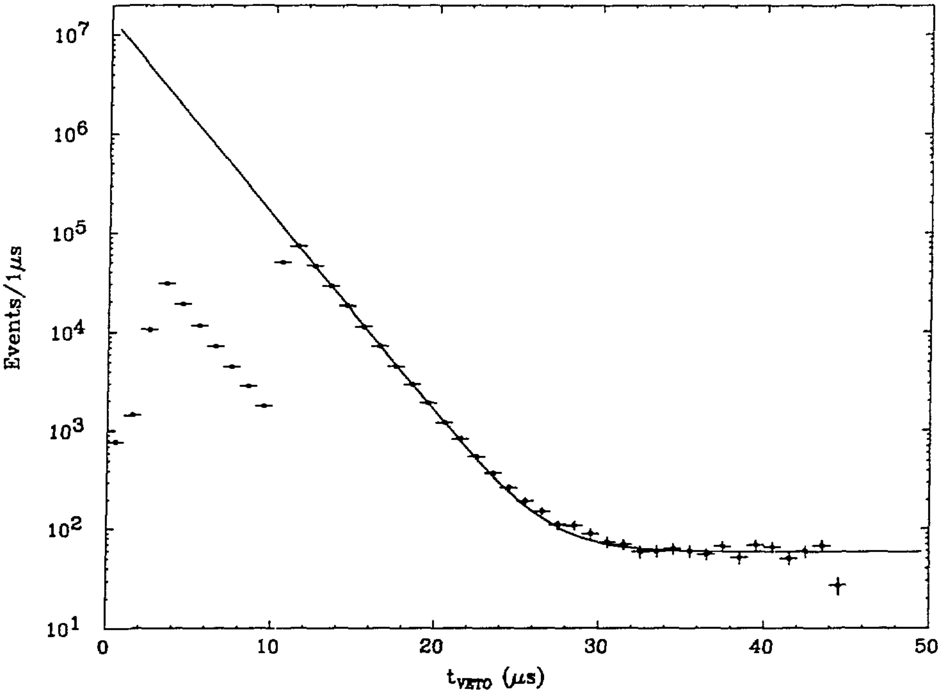

Figure 5.1: t_{veto} distribution for LongVeto-1. The interval $t_{veto} < 12\mu s$ is suppressed by the online vetoes. The solid line is the result of a fit to the interval $t_{veto} \geq 12\mu s$, which yields a muon mean lifetime of $\tau = 2.17 \pm 0.07\mu s$.

5.2.5 Results

The order of the Pass-1 data analysis tests and the number of events that survive each test are given in Table 5.4. The analysis efficiency of each test for $\bar{\nu}_e p$ CC events from full strength $\bar{\nu}_\mu \rightarrow \bar{\nu}_e$ oscillation, is also given in Table 5.4.

Approximately 36% of the events input to Pass-1 were rejected by the long vetoes. It is of academic interest to check whether the long vetoes remove stop muon decays. In Figure 5.1 we histogram the time of the veto (t_{veto}) for all events removed by the LongVeto-1 test. A fit is made to Figure 5.1 with an exponential added to a flat background

$$N = N_0 \exp^{-t_{veto}/\tau} + B$$

Test	Beam Gate		Pre-Beam Gate		Post-Beam Gate		Relative Efficiency
	Surviving Events	Relative Reduction	Surviving Events	Relative Reduction	Surviving Events	Relative Reduction	
(On Tape)	276452	—	633727	—	352136	—	—
Track-1	196817	0.712	451879	0.713	251348	0.714	0.913
ShortVeto-1	115890	0.589	265730	0.588	147346	0.586	0.994
LongVeto-1	41681	0.360	95902	0.361	53193	0.361	0.982
LongVeto-2	22228	0.533	51317	0.535	28446	0.535	0.993
LongVeto-3	17994	0.807	41295	0.805	22996	0.808	0.991
Track-2	17778	0.988	40903	0.991	22766	0.990	0.998
Track-3	14201	0.799	32598	0.797	18161	0.798	0.935
Fiducial	5788	0.605	13475	0.611	7498	0.618	0.714
ShortVeto-2	5615	0.970	13080	0.971	7272	0.970	0.995
ShortVeto-3	5323	0.948	12357	0.945	6867	0.944	0.982
ShortVeto-4	5094	0.957	11802	0.955	6556	0.955	0.985
LongVeto-4	5050	0.991	11709	0.992	6507	0.993	1.000
LongVeto-5	4434	0.878	10230	0.874	5640	0.867	0.995
LongVeto-6	4345	0.980	9973	0.975	5485	0.973	0.990
LongVeto-7	4224	0.972	9688	0.971	5319	0.970	0.996
LongVeto-8	4206	0.996	9648	0.996	5294	0.995	0.998
LongVeto-9	3394	0.807	7688	0.797	4219	0.797	0.925

Table 5.4: Results of the Pass-1 analysis. The relative efficiency in the last column is for synthetic $\bar{\nu}_e$p CC events from full strength $\bar{\nu}_\mu \to \bar{\nu}_e$ oscillation.

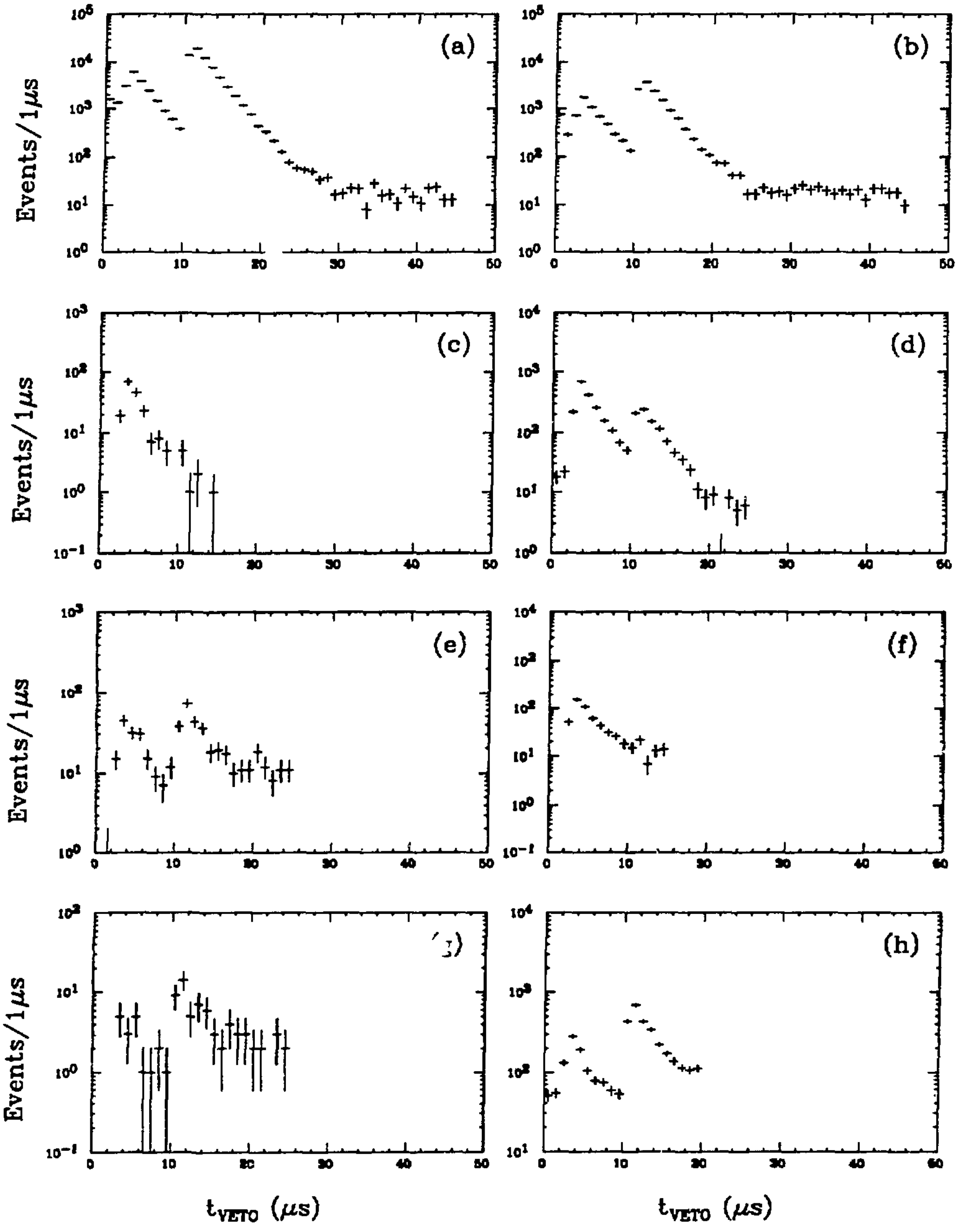

Figure 5.2: Distribution of $t_{\rm veto}$ for (a) LongVeto-2, (b) LongVeto-3, (c) LongVeto-4, (d) LongVeto-5, (e) LongVeto-6, (f) LongVeto-7, (g) LongVeto-8, and (h) LongVeto-9.

results in a muon mean lifetime of $\tau = 2.17 \pm 0.07\mu s$. This is in excellent agreement with the calculated value of $2.15\mu s$ for cosmic ray muons stopped in the detector given in Appendix A. It appears that the LongVeto-1 test does indeed remove muon decay events. From the above fit there are 57.7 accidental LongVeto-1 removals per $1\mu s$ bin or a total of 2597 accidental removals in 45 bins; the number of accidental removals by LongVeto-1 is less than 0.8%. In Figure 5.2 we plot the t_{veto} distribution for the remaining long vetoes. The long vetoes in Figure 5.2 have similar distributions to those of LongVeto-1 in Figure 5.1.

The search for recoil protons, which result from the interaction of fast neutrons, is made in the sample of events that survive the Track-1 test. We take advantage of the highly ionizing character of protons to make the identification of protons in this sample. In Figure 5.3 we make a scatter plot of the visible energy (E_{vis}) versus differential energy loss (dE/dx) of all events that survive the Track-1 test. The strong band clustered at dE/dx = 1MIP is interpreted as being minimum ionizing muons and electrons. The scattered events with higher dE/dx is interpreted as recoil protons. From Figure 4.11 in the previous chapter, we find that there are very few electrons with dE/dx $\geq$ 2MIPs; the proton events are defined to be tracks with dE/dx $\geq$ 2MIPs. Using this definition, we find that there are 9059 Beam Gate proton events, 20498 Pre-Beam Gate proton events, and 11463 Post-Beam Gate proton events.

5.3 Pass-2

The Pass-2 analysis selects electron (both e^+ and e^-) candidates from the sample of events that survive the Pass-1 analysis. The electrons are identified by scintillator and PDT differential energy loss (dE/dx). This analysis also selects photon candidates that are identified by dE/dx. The electron identification technique and the results of the analysis are discussed below.

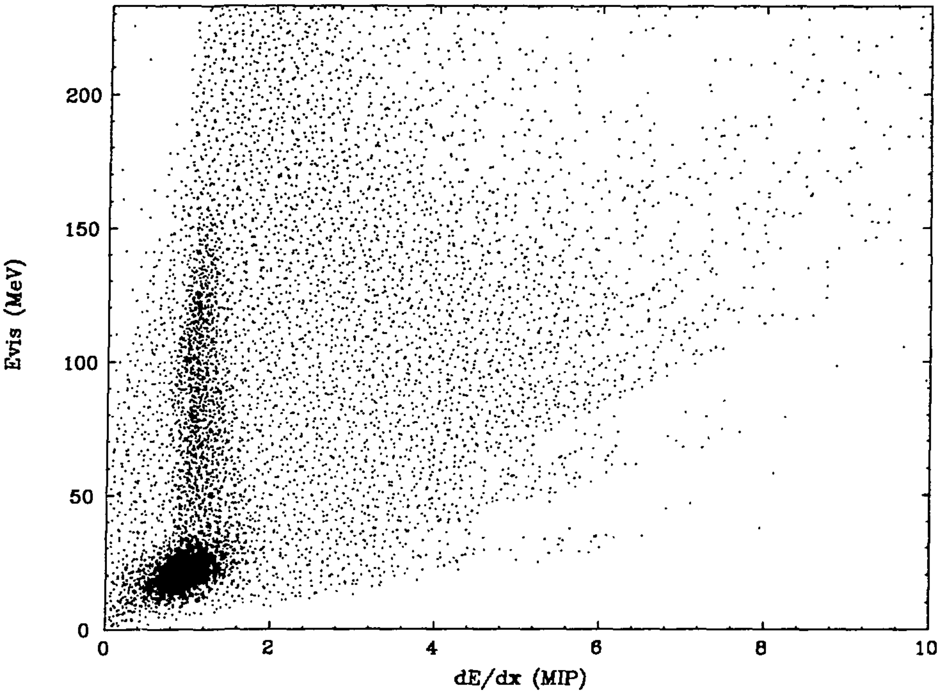

Figure 5.3: Distribution of E_{vis} versus dE/dx for all events that survive the Track-1 test.

5.3.1 Electron Identification

We use the measured differential energy loss (dE/dx) of charged particle tracks to identify electrons (both $e^+$and e^-). Events that pass the Track-2 test will have a minimum of four PDT dE/dx samples and two scintillator dE/dx samples. To quantify the dE/dx information, we use a likelihood method, which tests the track dE/dx samples to an electron hypothesis. This method was successfully used for particle identification by the Brookhaven neutrino experiment BNL E734 [61].

Separate likelihood functions are defined for the PDTs and the scintillators. The PDT likelihood function is defined as:

$$L_{PDT} = \prod_{PDT} P_{PDT}\left(e|\frac{dE_i}{dx}\right) \tag{5.1}$$

where the product is over the number of PDT samples. The probability density func-

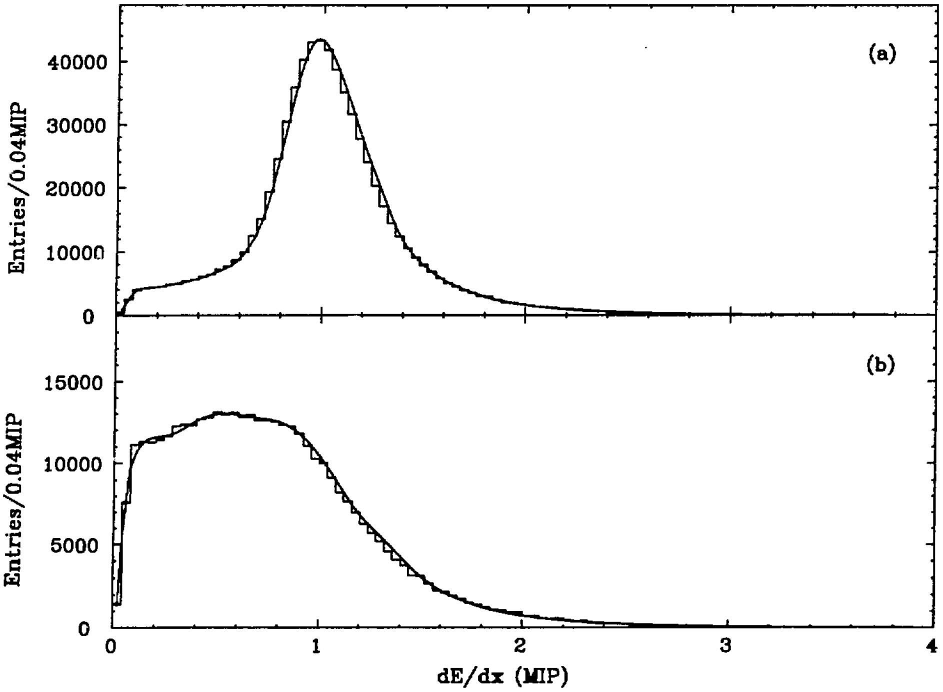

Figure 5.4: Scintillator electron *p.d.f.'s*. (a) Center Scintillators *p.d.f.*, P_{CSCI}. (b) End Scintillators *p.d.f.*, P_{ESCI}. The histogram is the measured *p.d.f.* from the stop muon data and the solid curve is the cubic spline and power law parameterization.

tion (*p.d.f.*) $P_{\mathrm{PDT}}\left(e|\frac{dE_i}{dx}\right)$ represent the probability that the particle is an electron given a differential energy loss measurement of dE_i/dx. Similarly, the scintillator likelihood function is defined as:

$$L_{SCI} = \prod_{CSCI} P_{CSCI}\left(e|\frac{dE_i}{dx}\right) \cdot \prod_{ESCI} P_{ESCI}\left(e|\frac{dE_i}{dx}\right) \qquad (5.2)$$

where the first product is over the scintillators at the center of a track and the second product is over the scintillators at the end of a track. A scintillator is defined to be at the center if the topology of the track requires that the particle passed completely through; that is, the scintillator is bounded by other planes of scintillators or PDTs. The scintillator topologies are treated differently because end scintillators will give an artificially low or high measurement of dE/dx. The center and the end scintillators have separate *p.d.f.s*, P_{CSCI} and P_{ESCI} respectively.

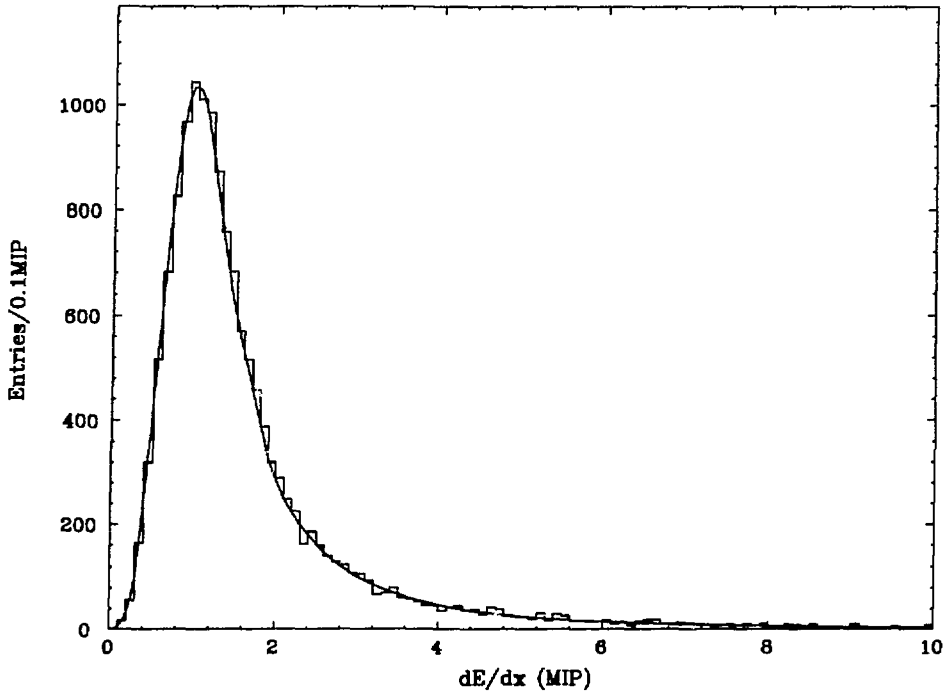

Figure 5.5: Typical PDT electron *p.d.f.* The histogram is measured *p.d.f.* from the stop muon data and the solid curve is the cubic spline and power law parameterization. There is one such *p.d.f.* per data tape.

The *p.d.f.s* are empirically determined from the decay electrons of cosmic ray muons that stop in the central detector. From the discussion of the Pass-1 results, we have found that over 35% of the events written to tape are due to stop muon decays. Stop muon decays result in electrons with energies very similar to the e^+ energy from $\bar{\nu}_e$p CC reactions and these electrons are ideal in determining the *p.d.f.s*. The database for *p.d.f.* calibration is provided by pristine stop muon events selected from the sample of events that were removed by the long veto tests in Pass-1. The PDT and scintillator dE/dx samples of events in this database are histogramed. The *p.d.f.s* are actually parameterization that are fit to the histograms. The parameterization is a combination of cubic splines [62] that continue into a power law decay in the tail. The histograms and the parameterization are shown in Figure 5.4

	Beam Gate Surviving Events	Pre-Beam Surviving Events	Post-Beam Surviving Events	Relative Efficiency
(from Pass-1)	3394	7688	4219	—
Electron ID	99	121	72	0.827

Table 5.5: Results of the Pass-2 analysis. The relative efficiency in the last column is for synthetic $\bar{\nu}_e$p CC events from full strength $\bar{\nu}_\mu \rightarrow \bar{\nu}_e$ oscillation.

and Figure 5.5. The PDT gains are found to drift up to 15% on a tape to tape basis. In order to adjust to the PDT gain drifts, one PDT *p.d.f.* calibration is made for each data tape. The scintillator gains are stable and a single *p.d.f.* is used for the entire 1987 run.

The parameters used in making an electron identification decision are the scintillator confidence level "C.L.(SCI)" and the PDT confidence level "C.L.(PDT)" that a track is an electron given the likelihoods L_{PDT} and L_{SCI}. The confidence levels are computed with Monte Carlo integration of 10,000 likelihoods generated from the empirical *p.d.f.s.*

5.3.2 Results

The distribution of electron confidence level for all events that survive the Pass-1 analysis is shown in Figure 5.6. The striking feature in Figure 5.6 is the strong peak in the bin C.L.(SCI) < 0.05 and C.L.(PDT) < 0.05. For comparison, electrons from stop muon decay will give a flat distribution of electron confidence levels as seen in Figure 5.7. The electron confidence level distribution of the Pass-1 neutrino candidates with low C.L.(SCI) or low C.L.(PDT) is inconsistent with electrons. We remove such events by requiring that C.L.(SCI) ≥ 0.05 and C.L.(PDT) ≥ 0.05. The electron confidence level distribution of the resultant sample of events is shown in Figure 5.8. We find that the region with C.L.(SCI) ≥ 0.15 and C.L.(PDT) ≥ 0.15 is consistent with the flat electron distribution, but the region C.L.(SCI) < 0.15 is

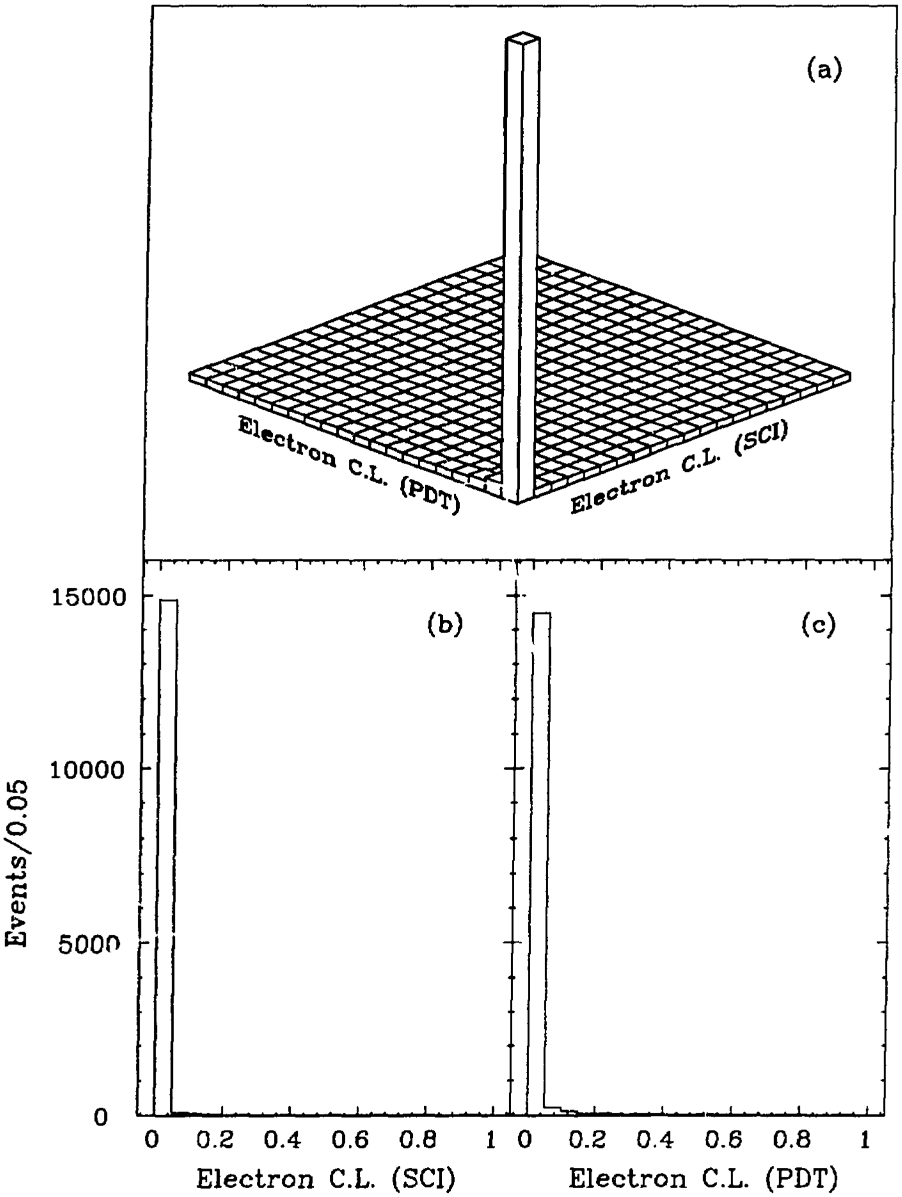

Figure 5.6: Electron confidence levels for all Pass-1 neutrino candidates. (a) Two-dimensional histogram of electron C.L.(PDT) versus electron C.L.(SCI). (b) Electron C.L.(SCI) projection. (c) Electron C.L.(PDT) projection.

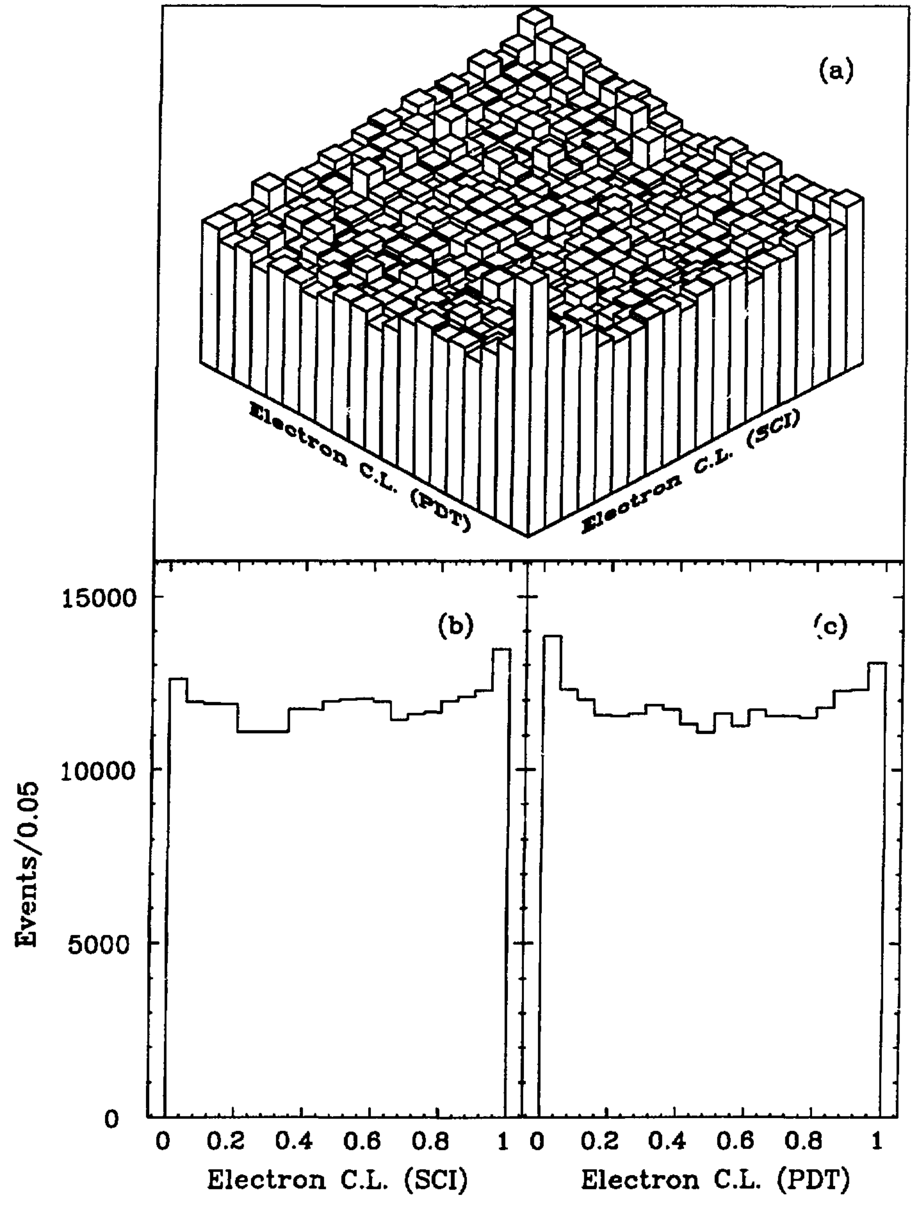

Figure 5.7: Electron confidence levels for selected decay electrons from cosmic ray muons that stop in the central detector. (a) Two-dimensional histogram of electron C.L.(PDT) versus electron C.L.(SCI). (b) Electron C.L.(SCI) projection. (c) Electron C.L.(PDT) projection.

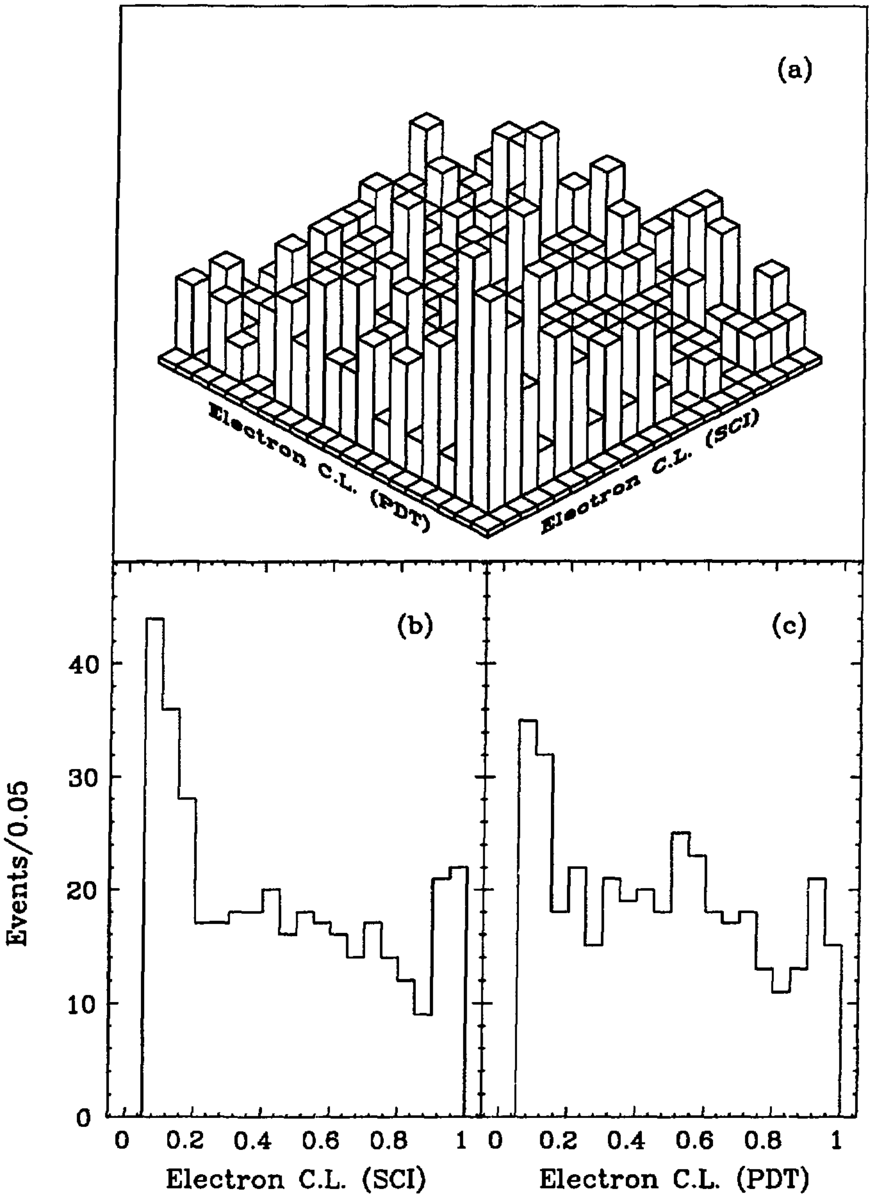

Figure 5.8: Electron confidence levels for Pass-1 neutrino candidates with C.L.(SCI) $\geq$ 0.05 and C.L.(PDT) $\geq$ 0.05. (a) Two-dimensional histogram of electron C.L.(PDT) versus electron C.L.(SCI). (b) Electron C.L.(SCI) projection. (c) Electron C.L.(PDT) projection.

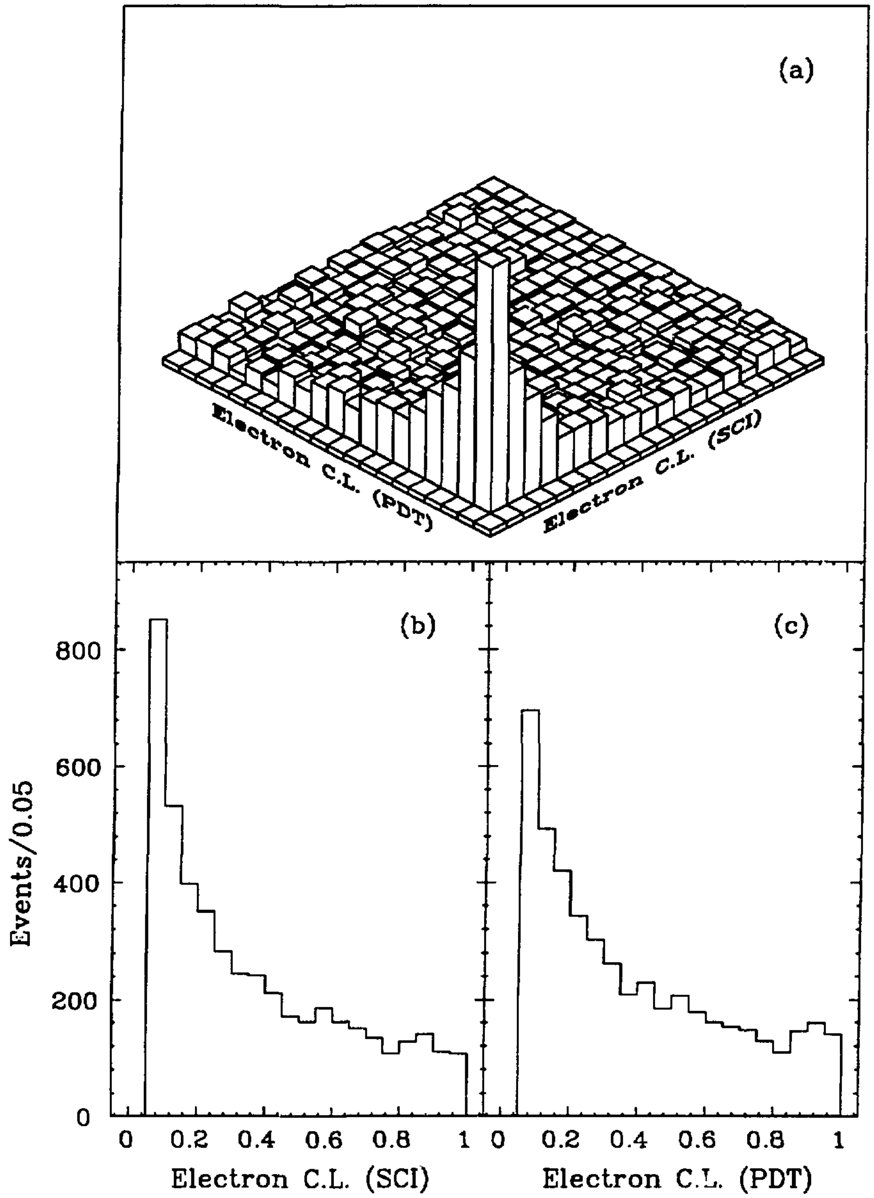

Figure 5.9: Electron confidence levels for Monte Carlo generated $\pi^0 \rightarrow 2\gamma$ events with C.L.(SCI) $\geq$ 0.05 and C.L.(PDT) $\geq$ 0.05. (a) Two-dimensional histogram of electron C.L.(PDT) versus electron C.L.(SCI). (b) Electron C.L.(SCI) projection. (c) Electron C.L.(PDT) projection.

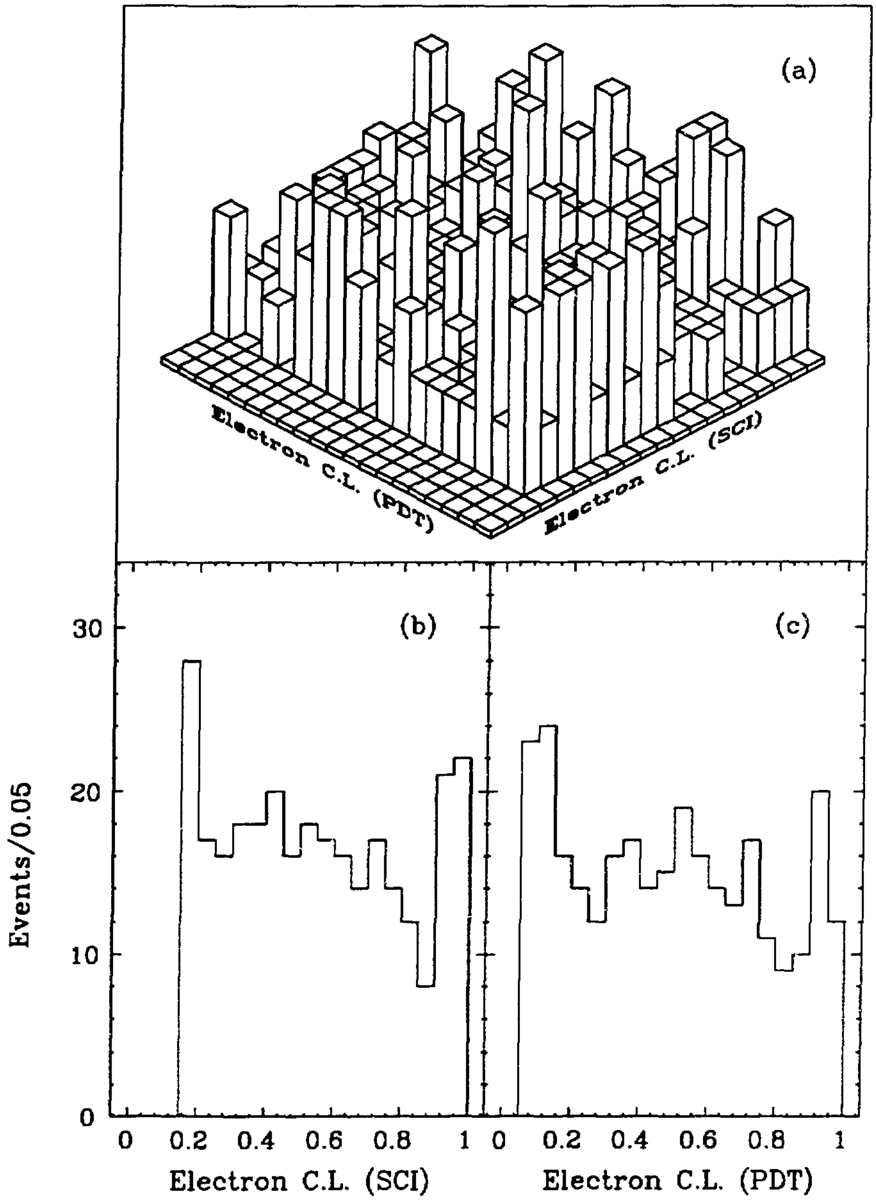

Figure 5.10: Electron confidence levels for all Pass-2 neutrino candidates. (a) Two-dimensional histogram of electron C.L.(PDT) versus electron C.L.(SCI). (b) Electron C.L.(SCI) projection. (c) Electron C.L.(PDT) projection.

not. It is expected that photons that interact through pair production can produce events with electron confidence levels in interval $0.05 \geq$ C.L. < 0.15. An example is shown in Figure 5.9, which is the electron confidence level distribution of Monte Carlo-generated stopped $\pi^0 \rightarrow 2\gamma$ decays. From the above discussion, we make the following particle identification criteria for neutrino candidates:

$$0.15 \leq \text{C.L.(SCI) and } 0.05 \leq \text{C.L.(PDT)}$$

and photon candidates:

$$0.05 \leq \text{C.L.(SCI)} < 0.15 \text{ and } 0.05 \leq \text{C.L.(PDT)}$$

The criterion results in 99 Beam Gate, 121 Pre-Beam Gate, and 72 Post-Beam Gate Pass-2 neutrino candidates; and 30 Beam Gate, 38 Pre-Beam Gate, and 14 Post-Beam Pass-2 photon candidates. The results of the Pass-2 analysis are summarized in Table 5.5.

5.4 Pass-3

The Pass-3 analysis removes DIF neutrino candidates from the sample of events that survive the Pass-2 analysis. The removed events are put into the DIF neutrino sample. The decay of the muon ($\bar{\nu}_\mu$ and ν_μ), from ν_μn and $\bar{\nu}_\mu$p CC reactions, identifies the DIF neutrino candidate. The test for DIF neutrino candidates and the results of the Pass-3 analysis are discussed below.

5.4.1 DIF Neutrino Veto

The following tests are designed to identify and remove DIF neutrino candidates from the sample of events that survive the Pass-2 analysis. The muon (μ^- and μ^+), from the ν_μn and $\bar{\nu}_\mu$p CC reactions, identifies the DIF neutrino candidate. We design these tests under the assumption that the electron, from $\mu^\pm \rightarrow e^\pm$ decay, triggers the event so that the basic topology for the DIF neutrino candidate is a spatially correlated muon track preceeding an electron trigger track. The DIF neutrino vetoes are divided into three tests, which are described in detail below.

DIF Veto-1 This veto is enabled when the triggered event is preceeded by a spatially correlated "muon" track. The spatial correlation requires that, if the "muon" track is reconstructed in both the x-profile and the y-profile, then the "muon" track must pass within 100cm of a trigger track endpoint. The "muon" track must be reconstructed in both the x-profile and the y-profile. If the "muon" track is reconstructed in either the x-profile or the y-profile, then the "muon" track must pass within 50cm of a trigger track endpoint. All events that are preceeded by this veto are rejected. This veto is designed to remove DIF neutrino candidates where the muon leaves a pristine track in the central detector.

DIF Veto-2 This veto is enabled when the triggered event is preceeded by a "muon" track whose endpoint is within one detector plane of a trigger track endpoint. All events preceeded by this veto within $25\mu s$ are rejected. This veto is designed to remove DIF neutrino candidates where the muon has a very steep (small $\cos\theta_z$) track.

DIF Veto-3 This veto is enabled when the triggered event is preceeded by a spatially correlated "muon", where the "muon" is simply a single scintillator panel. The spatial correlation requires that the "muon" be within one detector plane of a trigger track endpoint and that the projection of the trigger track onto the "muon" plane lies within the physical boundaries of the scintillator panel. All events preceeded by this veto within $25\mu s$ are rejected. This veto is designed to remove DIF neutrino candidates where the "muon" interacts in a single scintillator panel.

	Beam Gate Surviving Events	Pre-Beam Surviving Events	Post-Beam Surviving Events	Relative Efficiency
(from Pass-2)	99	121	72	—
DIF Veto-1	74	92	58	0.995
DIF Veto-2	68	89	57	0.993
DIF Veto-3	51	87	52	0.981

Table 5.6: Results of the Pass-3 analysis. The relative efficiency in the last column is for full strength $\bar{\nu}_\mu \rightarrow \bar{\nu}_e$+p→n+$e^+$ synthetic neutrino events.

5.4.2 Results

The results of the Pass-3 analysis are given in Table 5.6. The 51 Beam Gate, the 87 Pre-Beam Gate, and the 52 Post-Beam Gate events that survive the Pass-3 data reduction make up the final sample of neutrino candidates. The 48 Beam Gate, the 34 Pre-Beam Gate, and the 20 Post-Beam Gate events that were rejected by the Pass-3 data reduction tests make up the final sample DIF neutrino candidates.

The Pass-3 analysis is also performed on the Photon candidates that were selected in Pass-2. The final sample of Photon candidates consists of 23 Beam Gate events, 33 Pre-Beam Gate events, and 12 Post-Beam Gate events.

5.5 Pass-4

The Pass-4 analysis separates the final sample of neutrino candidates into two distinct sub-samples: the GD0 sub-sample and the GD1 sub-sample. The GD1 sub-sample contains all neutrino candidates that have one or more delayed slow neutron Gd-capture coincidences and the neutrino candidates in the GD0 sub-sample have zero delayed coincidences. The Gd-capture signature, used in the classification, has a multiplicity threshold of 1AND and 1XOR or 2 ANDs. This signature also requires that the visible energy of the capture signal be less than 9 MeV and that the centroid of the signal be less than 150cm from a trigger track endpoint. The

	Beam Gate Events	Pre-Beam Events	Post-Beam Events
All Neutrinos	51	87	52
GD0 Neutrinos	44	72	44
GD1 Neutrinos	7	15	8

Table 5.7: Results of the Pass-4 analysis.

window for the delayed coincidence is $[5, 100)\mu s$ relative to the trigger time. The results of the Pass-4 analysis are given in Table 5.7.

5.6 Neutrino Yield

The synthetic neutrino data is used to predict the number of neutrino induced events in the final sample of neutrino candidates. Synthetic neutrino events for each type of neutrino interaction are passed through the data analysis described above. The neutrino yield is equal to

$$Y = \frac{r_\pi \cdot Q}{1.602 \times 10^{-19}} \sum_i w_i \qquad (5.3)$$

where r_π is the number of π^+ decays per proton, Q is the integrated proton charge on the A-6 beam stop, w_i is the weight for synthetic event i, and the the sum is over all synthetic events that survive the data analysis. This method of estimating the neutrino yield is in effect a weighted Monte Carlo integration technique [68].

We would like to emphasize the fact that the synthetic neutrino data contains PMT and PDT signal time and pulse height information with the correct thresholds and energy scale corresponding to electrons (e^+ and e^-) and neutrons with the correct temporal, energy, spatial, and angular distributions as predicted by the neutrino interaction cross sections. The synthetic neutrino data also contains completely uncorrelated cosmic ray signals from random trigger data that introduces a loss in neutrino detection efficiency from accidental cosmic ray vetoes. The random

Reaction	Cross Section (cm^2)	Number of Targets	Trigger Efficiency	Analysis Efficiency	Number of Events
$\bar{\nu}_\mu \rightarrow \bar{\nu}_e$					
$\bar{\nu}_e$+p→n+e^+	9.56×10^{-41}	1.54×10^{30}	0.313	0.409	677.0 ± 83.7
$\nu_e \rightarrow \bar{\nu}_{eL}$					
$\bar{\nu}_{eL}$+p→n+e^+	7.36×10^{-41}	1.54×10^{30}	0.264	0.420	450.4 ± 55.7
$\nu_\mu \rightarrow \bar{\nu}_{eL}$					
$\bar{\nu}_{eL}$+p→n+e^+	6.13×10^{-41}	1.54×10^{30}	0.172	0.441	257.6 ± 31.8
$\mu^+ \rightarrow e^+ \bar{\nu}_e \nu_\mu$					
$\bar{\nu}_e$+p→n+e^+	9.56×10^{-41}	1.54×10^{30}	0.313	0.409	677.0 ± 83.7
Background					
$\nu_e + {}^{12}\mathrm{C} \rightarrow X + e^-$	1.46×10^{-41}	8.21×10^{29}	0.105	0.446	20.1 ± 5.6
$\nu_e + {}^{13}\mathrm{C} \rightarrow X + e^-$	4.0×10^{-41}	9.13×10^{27}	0.237	0.429	1.3 ± 0.7
$\nu_e + {}^{16}\mathrm{O} \rightarrow X + e^-$	5.2×10^{-42}	1.49×10^{29}	0.050	0.463	0.6 ± 0.2
$\nu_e + {}^{27}\mathrm{Al} \rightarrow X + e^-$	4.0×10^{-41}	6.35×10^{27}	0.159	0.458	0.7 ± 0.3
$\nu_\mu + e^- \rightarrow \nu_\mu + e^-$	4.68×10^{-44}	7.80×10^{30}	0.120	0.489	0.8 ± 0.1
$\nu_e + e^- \rightarrow \nu_e + e^-$	3.00×10^{-43}	7.80×10^{30}	0.210	0.482	8.5 ± 1.0
$\bar{\nu}_\mu + e^- \rightarrow \bar{\nu}_\mu + e^-$	4.95×10^{-44}	7.80×10^{30}	0.208	0.470	1.4 ± 0.2
Total Background Neutrino Events					33.3 ± 5.8

Table 5.8: Predicted neutrino yields. The prediction is for 5528 coulombs of integrated proton charge on the A-6 target, which gives a neutrino flux of $3.59 \times 10^{13} \nu/\mathrm{cm}^2$ (of each type: ν_μ, ν_e, and $\bar{\nu}_\mu$) incident on the E645 detector. The predicted signal yields are for full strength $\bar{\nu}_\mu, \nu_e, \nu_\mu \rightarrow \bar{\nu}_e$ oscillations and $\mu^+ \rightarrow e^+ \bar{\nu}_e \nu_\mu$ decay. The errors reflect a 12.5% uncertainty in the neutrino flux, a 25% uncertainty in the $\nu_e{}^{12}\mathrm{C}$ and $\nu_e{}^{16}\mathrm{O}$ cross sections, and a 50 % uncertainty in the $\nu_e{}^{13}\mathrm{C}$ and $\nu_e{}^{27}\mathrm{Al}$ cross sections.

trigger data also gives the synthetic neutrino data accidental neutron coincidences. Therefore all online and offline losses in neutrino detection efficiency are properly modeled by the synthetic neutrino data.

The predicted yields for Q = 5527.7 and $r_\pi = 0.089 \pm 0.011$ are given in Table 5.8. The errors in the yields given in Table 5.8 reflect a 12.5% uncertainty in r_π, a 25% uncertainty in the $\nu_e {}^{12}C$ and $\nu_e {}^{16}O$ CC cross sections, and a 50% uncertainty in the $\nu_e {}^{13}C$ and $\nu_e {}^{27}Al$ CC cross sections [66]. In addition, there is a 2% uncertainty in the $\bar{\nu}_e p$ CC cross section and a 5% uncertainty in the νe^- elastic cross sections. The *statistical uncertainties*, based upon the number of synthetic events that survive the analysis, are less than 1% for the $\bar{\nu}_e$ appearance signal and less that 2% for the background neutrino events.

Chapter 6

Results

6.1 Neutrino Sample

We investigate the beam excess and Post-Beam excess of neutrino candidates. In both cases, the Pre-Beam Gate data is used to estimate the cosmic ray background.

6.1.1 Beam Excess

The 51 Beam Gate and the 87 Pre-Beam Gate neutrino candidates are categorized in Table 6.1. The beam excess of 12.5±8.2 events is expected to consist of $\nu_\mu e^-$, $\nu_e e^-$, and $\bar{\nu}_\mu e^-$elastic scattering background events; ν_en CC background events; and the $\bar{\nu}_e$p CC signal from possible $\bar{\nu}_e$ appearance. Background events induced by fast beam neutrons and DIF ν_μn and $\bar{\nu}_\mu$p CC interactions are also expected, however,

Gate	Total Number of Neutrinos	Number of GD0 Neutrinos	Number of GD1 Neutrinos
Beam	51	44	7
Pre-Beam	87	72	15
Beam Excess	12.5 ± 8.2	12.2 ± 7.6	0.4 ± 3.2

Table 6.1: Neutrino candidates. The ratio of the Beam Gate live time to the Pre-Beam Gate live time is 0.442 .

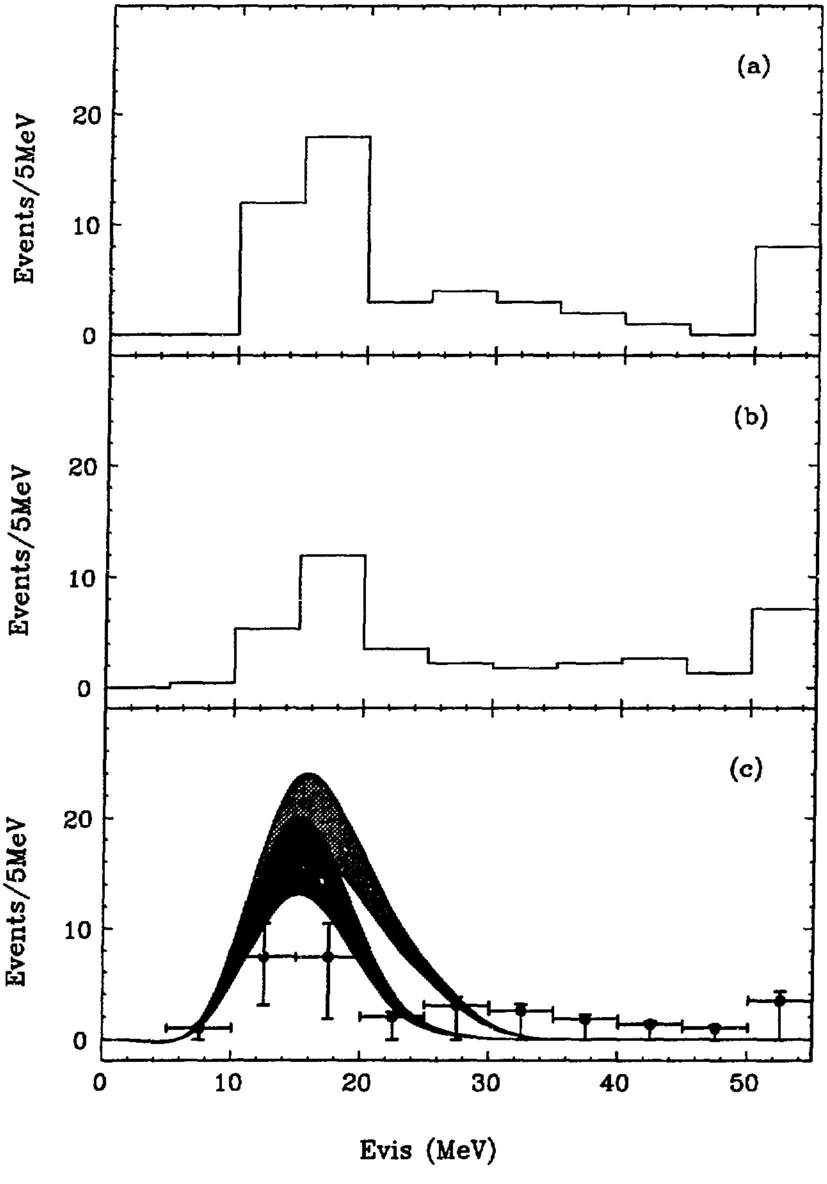

Figure 6.1: The E_{vis} distribution of the neutrino candidates. (a) Beam Gate data. (b) Pre-Beam Gate data normalized to the Beam Gate live time. (c) Beam excess. The dark shaded band, in (c), is the predicted beam excess spectrum assuming the null hypothesis, i.e., the beam excess results from νe^- elastic scattering and ν_en CC interactions. The light shaded band represents the same, but with a $\bar{\nu}_e$p CC signal resulting from a 2.5% $\bar{\nu}_\mu \rightarrow \bar{\nu}_e$ oscillation probability. The width of the bands represents a two standard deviation systematic uncertainty in the predicted spectrum. The last bin on the right contains all events with $E_{vis} \geq 50$MeV. The procedure used in estimating the points and the vertical "error bars" (68.3% confidence regions) in (c), is described in Appendix B.

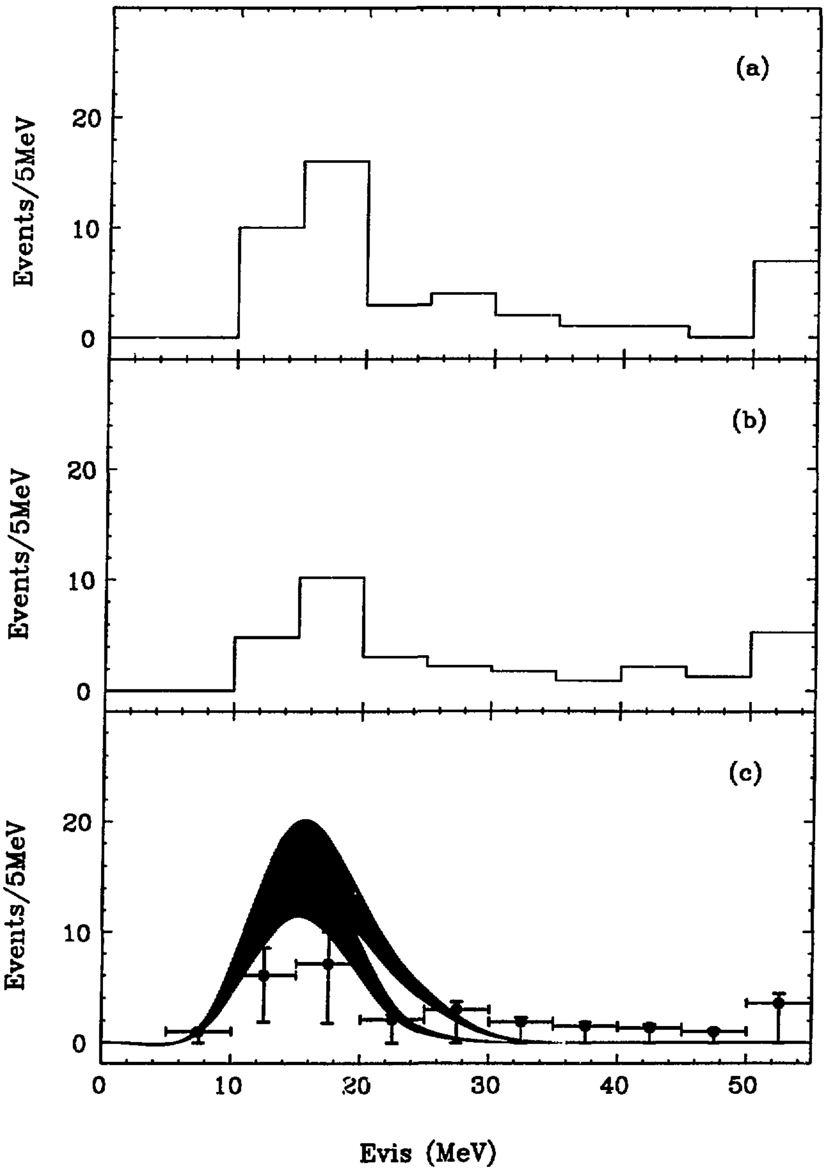

Figure 6.2: The E_{vis} distribution of the GD0 neutrino candidates. (a) Beam Gate data. (b) Pre-Beam Gate data normalized to the Beam Gate live time. (c) Beam excess. The dark shaded band, in (c), is the predicted beam excess spectrum assuming the null hypothesis, i.e., the beam excess results from νe^- elastic scattering and ν_en CC interactions. The light shaded band represents the same, but with a $\bar{\nu}_e$p CC signal resulting from a 2.5% $\bar{\nu}_\mu \rightarrow \bar{\nu}_e$ oscillation probability. The width of the bands represents a two standard deviation systematic uncertainty in the predicted spectrum. The last bin on the right contains all events with $E_{vis} \geq 50$MeV. The procedure used in estimating the points and the vertical "error bars" (68.3% confidence regions) in (c), is described in Appendix B.

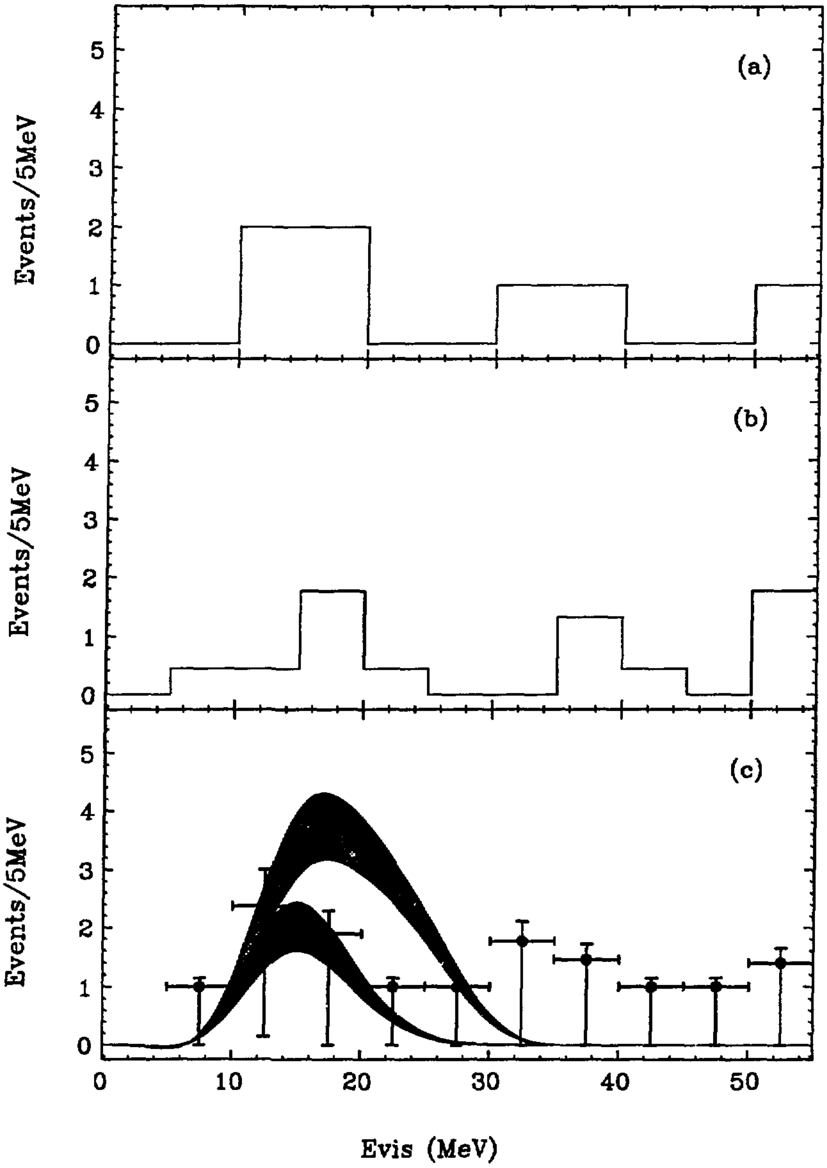

Figure 6.3: The E_{vis} distribution of the GD1 neutrino candidates. (a) Beam Gate data. (b) Pre-Beam Gate data normalized to the Beam Gate live time. (c) Beam excess. The dark shaded band, in (c), is the predicted beam excess spectrum assuming the null hypothesis, i.e., the beam excess results from νe^- elastic scattering and ν_en CC interactions. The light shaded band represents the same, but with a $\bar{\nu}_e$p CC signal resulting from a 2.5% $\bar{\nu}_\mu \rightarrow \bar{\nu}_e$ oscillation probability. The width of the bands represents a two standard deviation systematic uncertainty in the predicted spectrum. The last bin on the right contains all events with $E_{vis} \geq 50$MeV. The procedure used in estimating the points and the vertical "error bars" (68.3% confidence regions) in (c), is described in Appendix B.

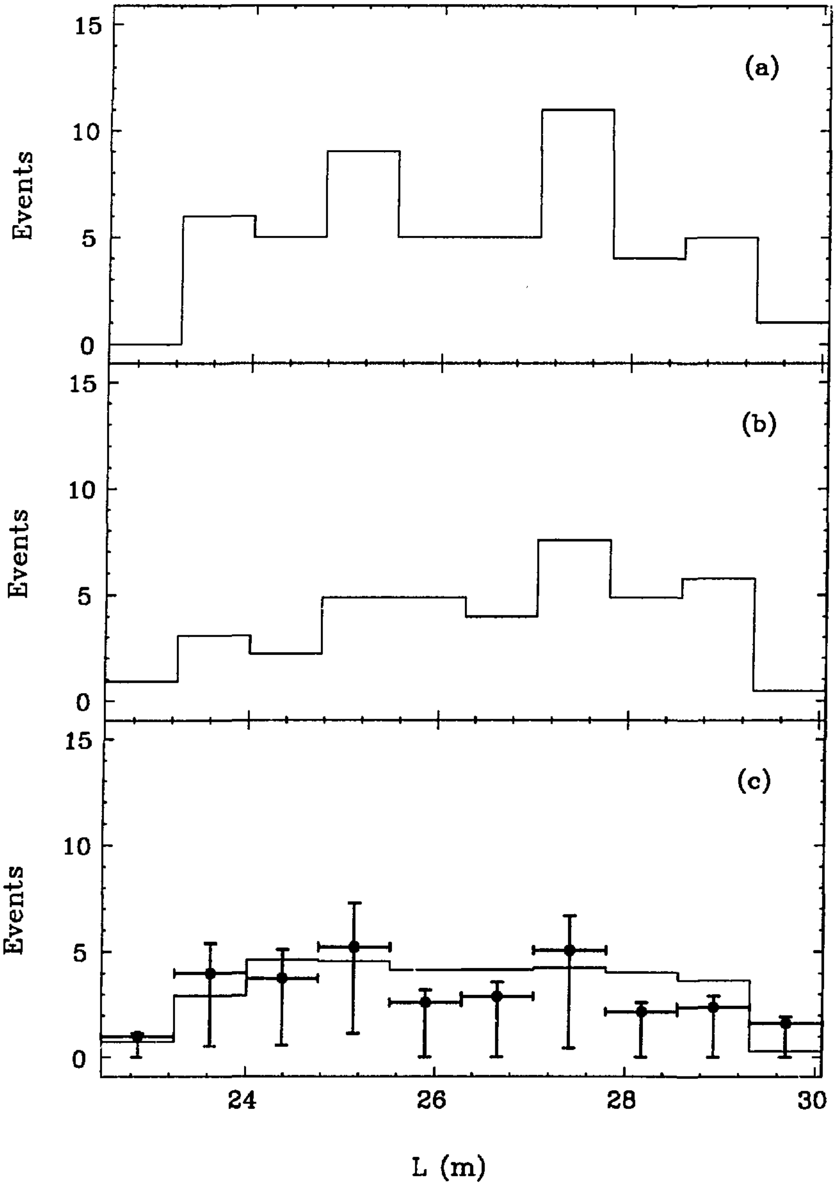

Figure 6.4: The spatial distribution of the neutrino candidates. (a) Beam Gate data. (b) Pre-Beam Gate data normalized to the Beam Gate live time. (c) Beam excess. The spatial parameter "L" is the distance from the A-6 beam stop to the event track, averaged over the track endpoints. The histogram, in (c), is the beam excess spatial distribution predicted by the null hypothesis, i.e., the beam excess results from νe^- elastic scattering and ν_en CC interactions. The procedure used in estimating the points and the vertical "error bars" (68.3% confidence regions) in (c), is described in Appendix B.

for the present discussion we shall assume these events are negligible.

The E_{vis} distribution of the neutrino candidates is shown in Figure 6.1. The same distribution of the GD0 and GD1 neutrino candidates are shown in Figures 6.2 and 6.3 respectively. The predicted beam excess spectrum under the null hypothesis, where there is no $\bar{\nu}_e$ appearance and the beam excess consists solely of νe^- elastic scattering events and ν_en CC events, is given in Figure 6.1 by the dark solid band. For comparison, the predicted beam excess spectrum with a 2.5% $\bar{\nu}_\mu \rightarrow \bar{\nu}_e$ oscillation probability is also given in Figure 6.1 by the light solid band. The full width of the solid bands represents the two standard deviation systematic uncertainties in the predicted spectrum. We find that the beam excess E_{vis} distribution of the data agrees with the null hypothesis in shape, but not in normalization where there is a large deficiency in the observed beam excess. The deficiency in the number of observed events becomes much more evident in the integral, where observed beam excess is 12.5 ± 8.2 events and null hypothesis predicts 33.3 ± 5.8 events. The deficiency in the observed beam excess is -20.8 ± 10.1 events or approximately two standard deviations.

A possible $\bar{\nu}_e$ appearance signal will further increase the deficiency in the measured beam excess. In addition, the shape of the $\bar{\nu}_e$ appearance signal is inconsistent with the measured data. Therefore, we find no evidence for $\bar{\nu}_e$ appearance in the neutrino sample.

However, the deficiency in the number of beam excess neutrino candidates is a potential problem because it indicates that the neutrino acceptance or the neutrino flux may be overestimated. We will address this problem in the Chapter 7.

6.1.2 Post-Beam Excess

The number of Post-Beam Gate and Pre-Beam Gate neutrino candidates is given in Table 6.2. The E_{vis} distribution of these events is shown in Figure 6.5. We find that there is a Post-Beam excess in this distribution in the interval $20\text{MeV} \leq E_{vis} <$

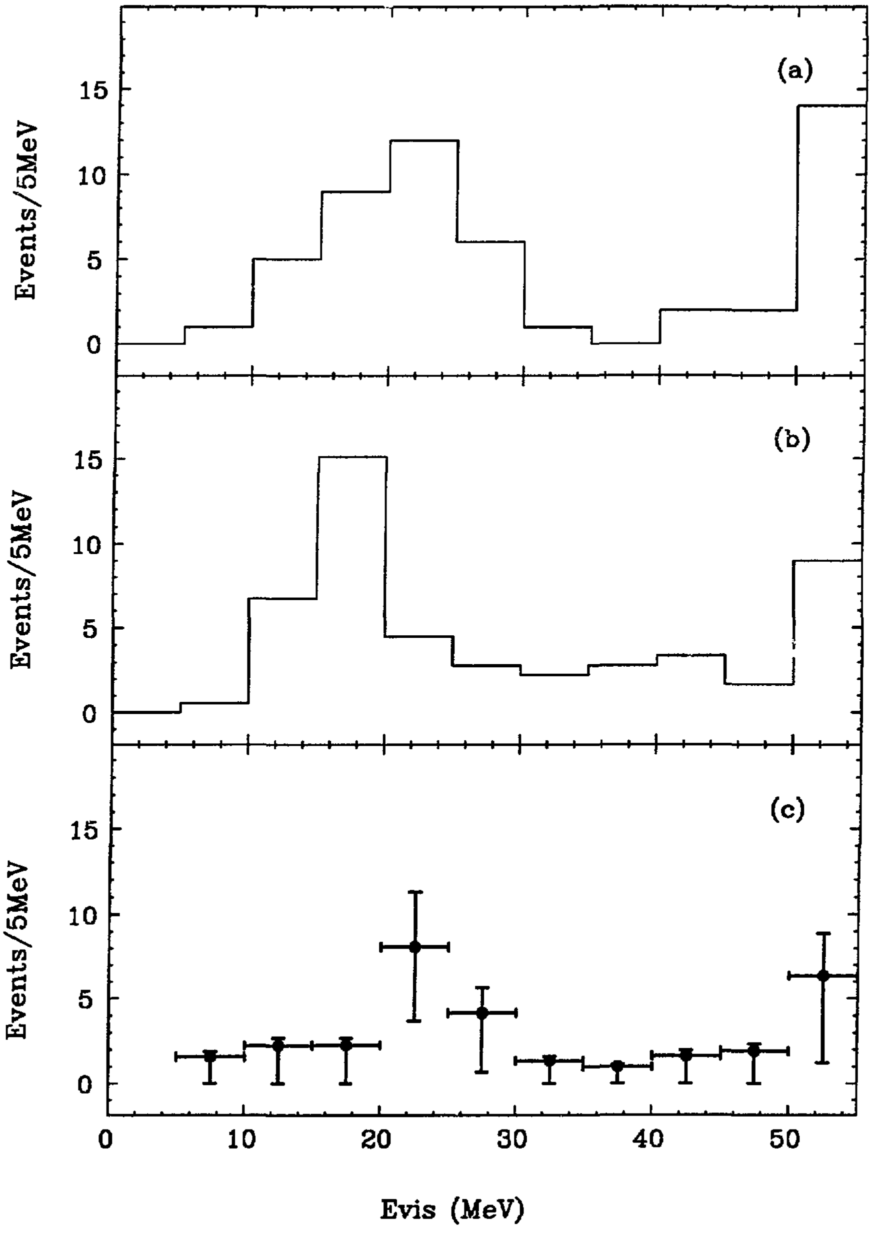

Figure 6.5: The Post-Beam E_{vis} distribution of the neutrino candidates. (a) Post-Beam Gate data. (b) Pre-Beam Gate data normalized to the Post-Beam Gate live time. (c) Post-Beam excess. The last bin on the right contains all events with $E_{vis} \geq 50$MeV. The procedure used in estimating the points and the vertical "error bars" (68.3% confidence regions) in (c), is described in Appendix B.

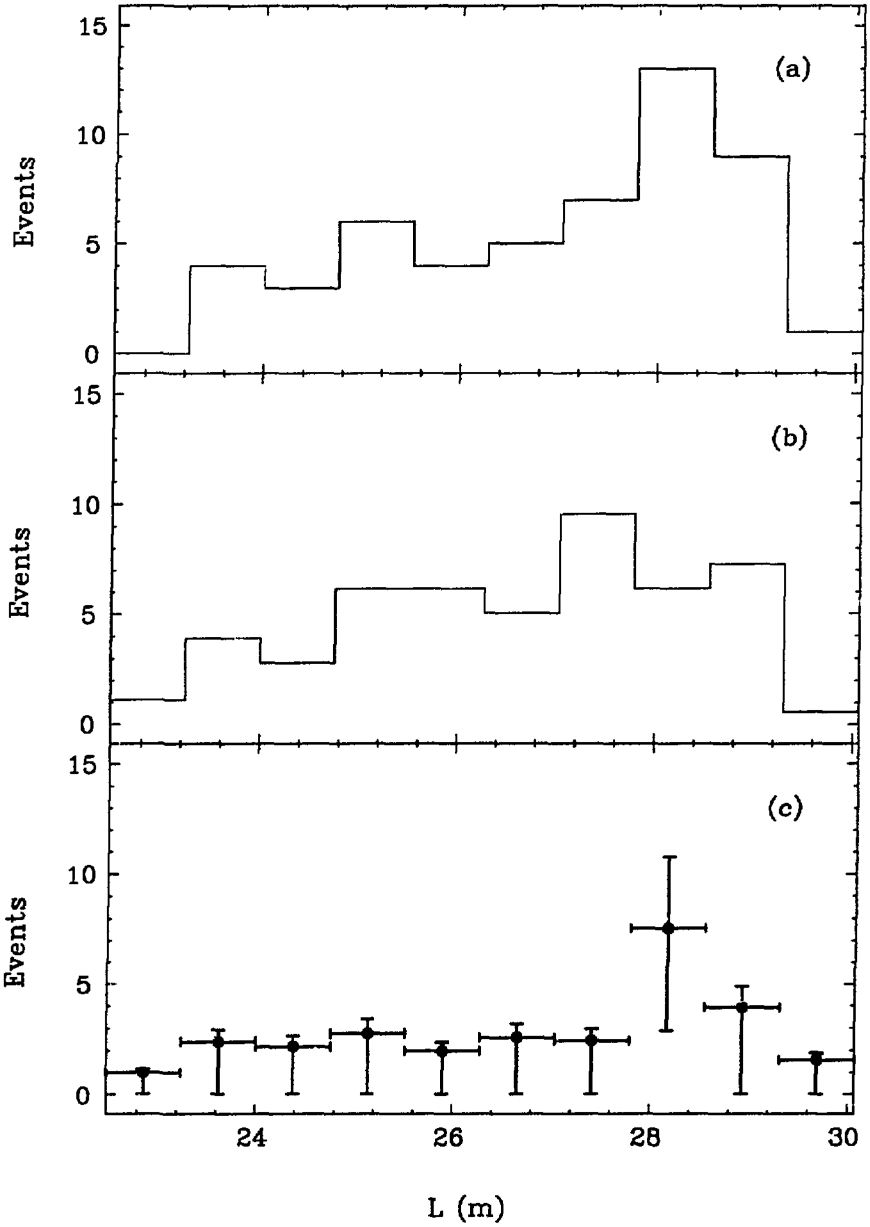

Figure 6.6: The Post-Beam spatial distribution of the neutrino candidates. (a) Post-Beam Gate data. (b) Pre-Beam Gate data normalized to the Post-Beam Gate live time. (c) Post-Beam excess. The spatial parameter "L" is the distance from the A-6 beam stop to the event track, averaged over the track endpoints. The procedure used in estimating the points and the vertical "error bars" (68.3% confidence regions) in (c), is described in Appendix B.

Gate	Number of Neutrinos
Post-Beam	52
Pre-Beam	87
Post Excess	3.3 ± 8.9

Table 6.2: Post-Beam Neutrino candidates. The ratio of the Post-Beam Gate live time to the Pre-Beam Gate live time is 0.560 .

30MeV and for $E_{vis} \geq 50$MeV. The Post-Beam excess is also evident in the spatial distribution given in Figure 6.6, where the excess occurs in the back of the central detector.

It is important to note that the shape of the Post-Beam E_{vis} distribution in Figure 6.5 and the spatial distribution in Figure 6.6 are different from the beam excess E_{vis} and spatial distributions given in Figures 6.1 and 6.4, respectively. This indicates that the background source of Post-Beam excess is not present in the Beam Gate.

The existence of the Post-Beam excess may indicate some "long-lived" ($\sim$ 1ms) beam associated events. There will be no attempt to discuss the origins of these events. We conclude by merely pointing out the existence of the Post-Beam excess and leave the comprehensive investigation of this phenomenon to a future analysis.

6.2 Background Samples

The Beam Gate and the Pre-Beam Gate background candidates are categorized in Table 6.3. We discuss each background topology individually below. In addition, we develop a model to describe the beam background and estimate the contamination of the observed beam background into the neutrino sample.

Gate	Number of Protons	Number of Photons	Number of DIF Neutrinos
Beam	9059	23	48
Pre-Beam	20498	33	34
Beam Excess	-1.1 ± 114.3	8.4 ± 5.4	33.0 ± 7.4

Table 6.3: Background candidates. The ratio of the Beam Gate live time to the Pre-Beam Gate live time is 0.442 .

6.2.1 Proton

From Table 6.3, the proton beam excess is equal to -1.1 ± 114.3 events. This zero beam excess is confirmed by the E_{vis} distribution of the proton candidate given in Figure 6.7, which shows a flat distribution.

The proton events are expected to arise from energetic neutrons that scatter off of the hydrogen atoms in the central detector. In approximately one-half of such scatters, the recoil proton carries most of the momentum of the incident neutron. The detector will accept protons with kinetic energy $T_p \geq 80$MeV at normal incidence [70]. Therefore, the zero beam excess of proton candidates indicates that the flux of beam neutrons incident upon the detector with normal incident and $T_n \geq 80$MeV is negligible.

6.2.2 Photon

The search for photon events results in a non-zero beam excess of 8.4 ± 5.4 events. The E_{vis} distribution of these events is given in Figure 6.8. For comparison, we also plot the E_{vis} distribution of Monte Carlo generated stopped $\pi^0 \rightarrow 2\gamma$ decays normalized to the number of beam excess photon events. We find that the E_{vis} distribution of the observed data is in agreement with the predicted E_{vis} distribution of π^0 decays. The spatial distribution of the photon candidates, given in Figure 6.9, reveals that beam excess photon candidates are confined to a limited region of the central detector.

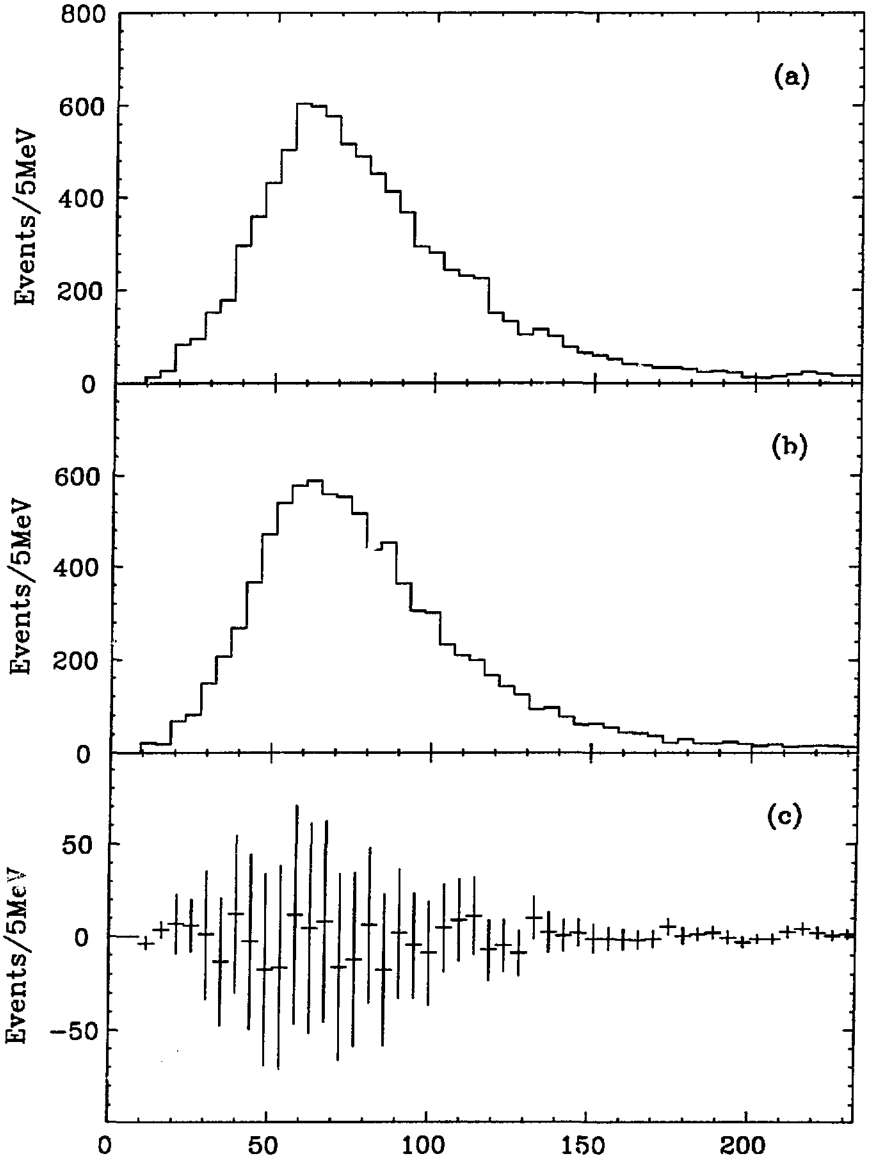

Figure 6.7: The E_{vis} distribution of the proton candidates. (a) Beam Gate data. (b) Pre-Beam Gate data normalized to the Beam Gate live time. (c) Beam excess.

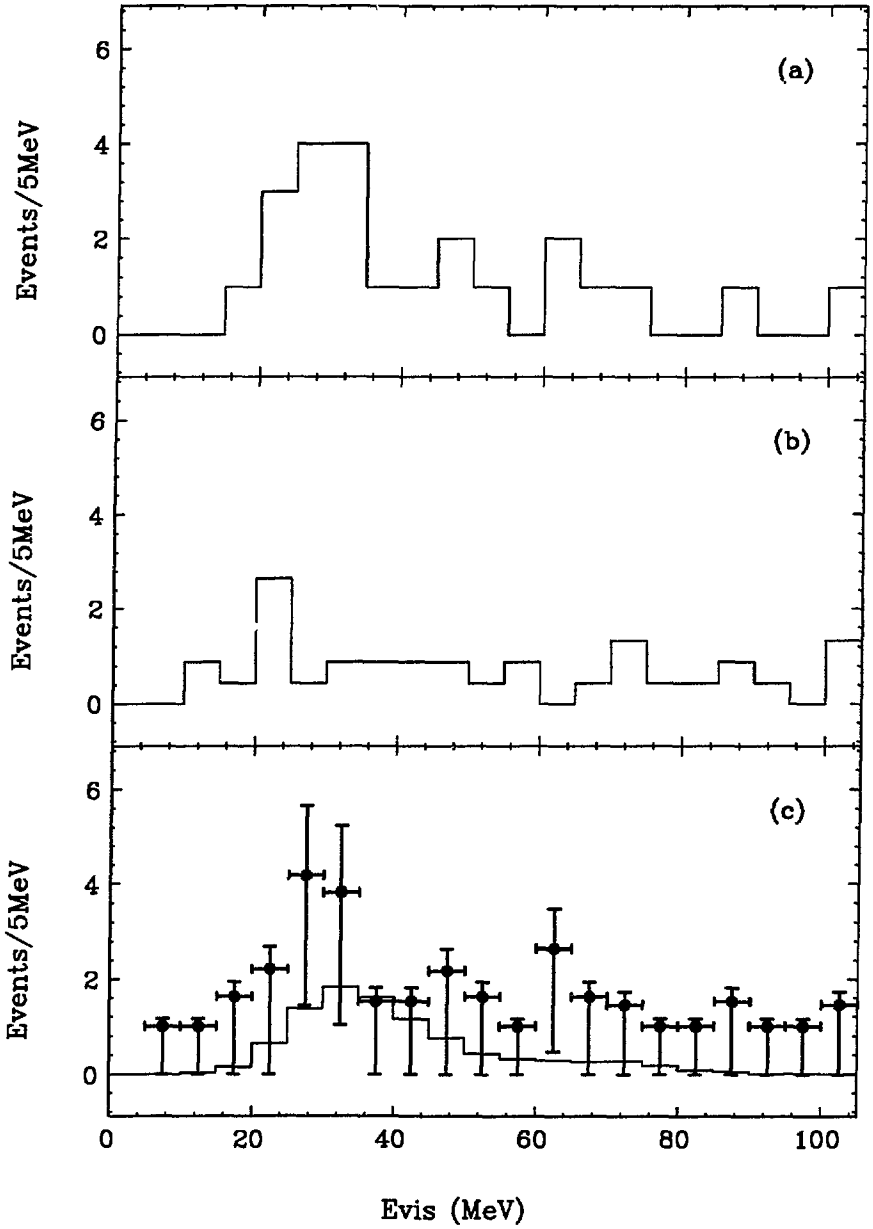

Figure 6.8: The E_{vis} distribution of the photon candidates. (a) Beam Gate data. (b) Pre-Beam Gate data normalized to the Beam Gate live time. (c) Beam excess. The histogram, in (c), is the E_{vis} distribution from Monte Carlo generated $\pi^0 \rightarrow 2\gamma$ decays. This histogram is normalized to the number of beam excess events. The last bin on the right contains all events with $E_{vis} \geq 100$MeV. The procedure used in estimating the points and the vertical "error bars" (68.3% confidence regions) in (c), is described in Appendix B.

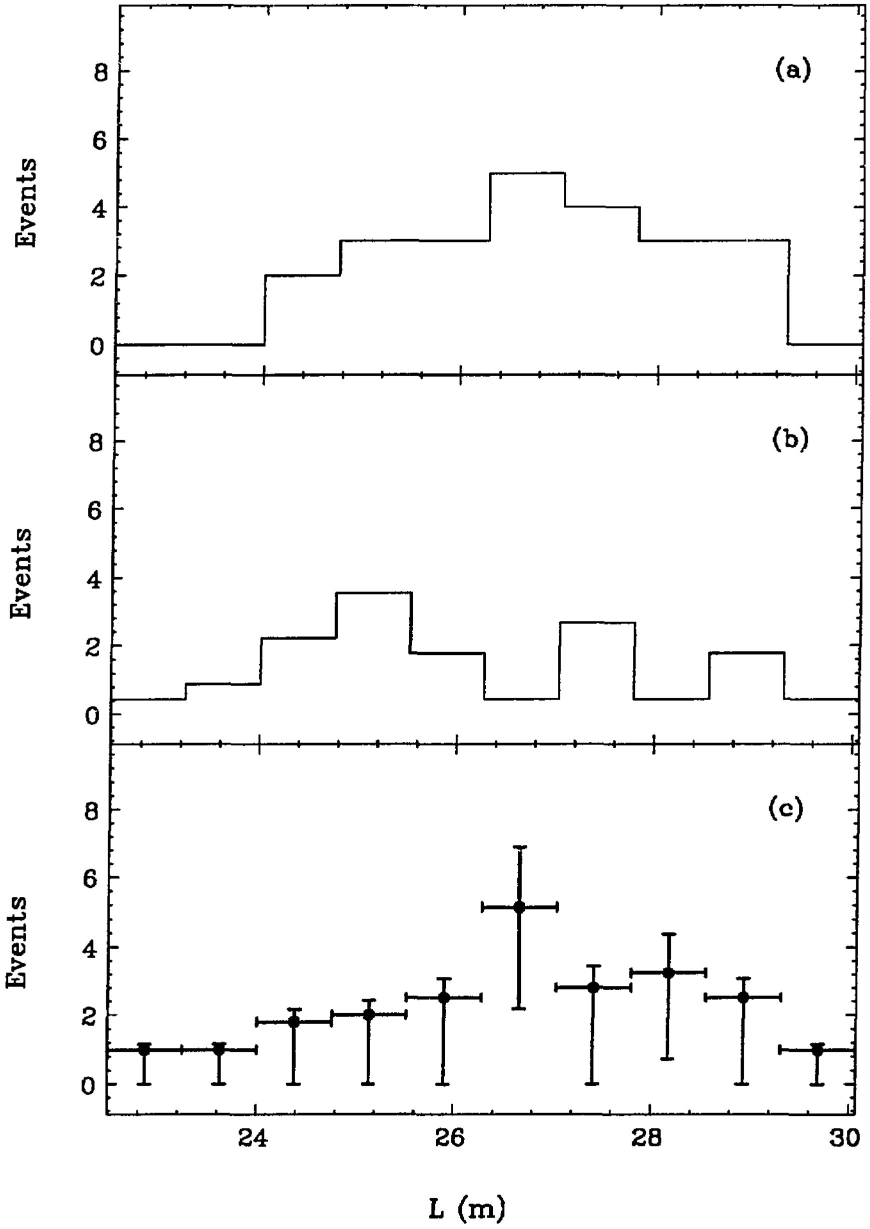

Figure 6.9: The spatial distribution of the photon candidates. (a) Beam Gate data. (b) Pre-Beam Gate data normalized to the Beam Gate live time. (c) Beam excess. The spatial parameter "L" is the distance from the A-6 beam stop to the event track, averaged over the track endpoints. The procedure used in estimating the points and the vertical "error bars" (68.3% confidence regions) in (c), is described in Appendix B.

Both neutral and charged pions are expected to result from the inelastic interactions of fast neutrons. If the beam excess photon candidates are in fact neutral pions, then this would indicate that beam neutrons are incident upon a confined region of the central detector.

6.2.3 DIF Neutrino

The search for DIF neutrino candidates results in a beam excess of 33.0 ± 7.4 events. The distribution of the time of the muon t_μ, from the DIF ν_μn and $\bar{\nu}_\mu$p CC reaction, relative to the time t_e of the electron is given in Figure 6.10. We find that the decay of the observed beam excess $t_e - t_\mu$ distribution is in agreement with the muon mean lifetime of $\tau_\mu = 2.2\mu$s. The electron E_{vis} distribution of DIF neutrino candidates is given in Figure 6.11. For comparison, the electron E_{vis} distribution of Monte Carlo-generated stopped $\mu^\pm \rightarrow e^\pm$ decays is also given. The observed beam excess E_{vis} distribution is in agreement with $\mu^\pm \rightarrow e^\pm$ decay. The electron spatial distribution of the DIF neutrino candidates is given in Figure 6.12. We find that this distribution peaks in nearly the same location as the peak in the spatial distribution of the photon candidates. The predicted spatial distribution of real DIF neutrinos should be nearly uniform.

Low energy charged pion events have exactly the same event selection topology as the DIF neutrinos. The fact that the spatial distribution of the DIF neutrino candidates peaks at the same location as the $\pi^0 \rightarrow 2\gamma$ decay events (the photon candidates), indicates that at least half of the DIF neutrino candidates are really low energy charged pion decays. This further strengthens the above hypothesis that beam neutrons are incident upon the central detector.

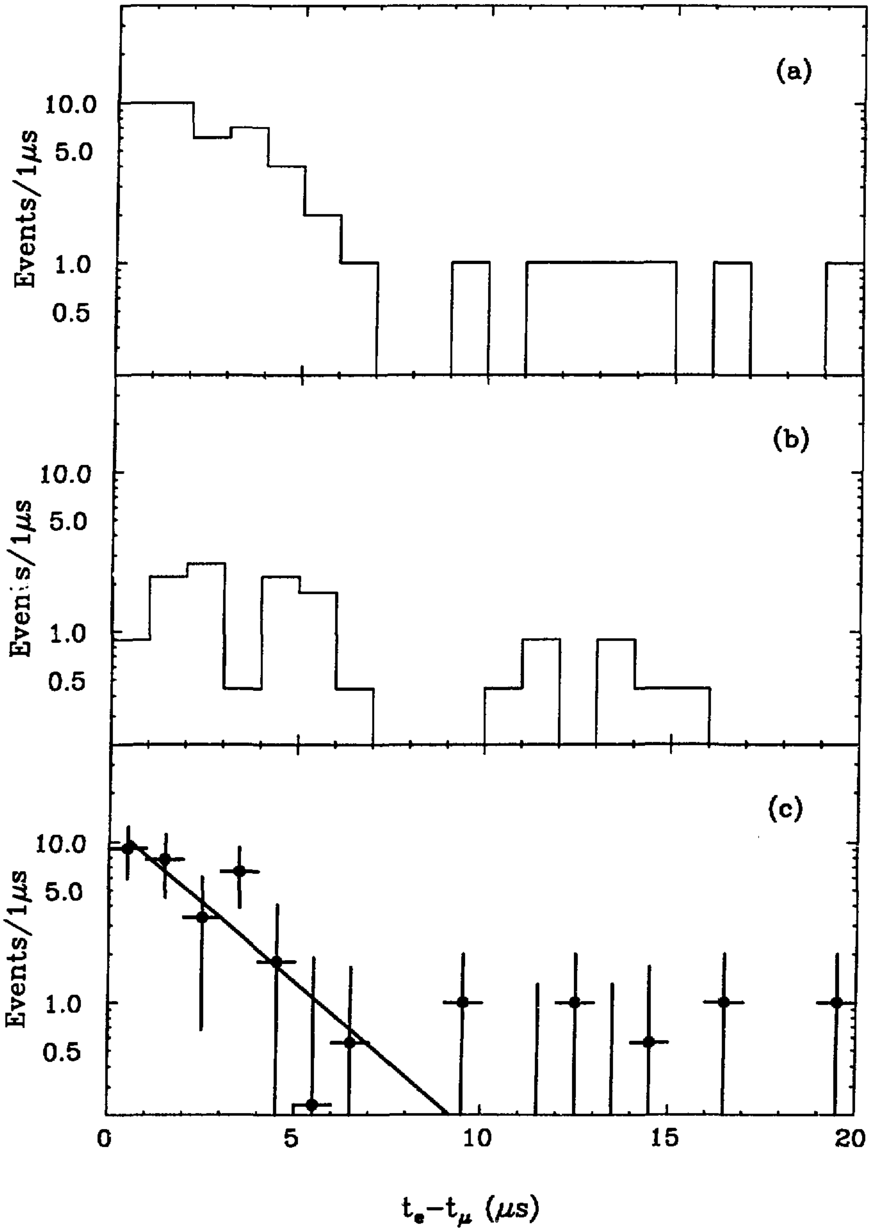

Figure 6.10: Distribution of $t_e - t_\mu$ for the DIF neutrino candidates. (a) Beam Gate data. (b) Pre-Beam Gate data normalized to the Beam Gate live time. (c) Beam excess. The straight line, in (c), shows the muon mean lifetime $\tau_\mu = 2.2\mu$s, which is arbitrarily placed for comparison.

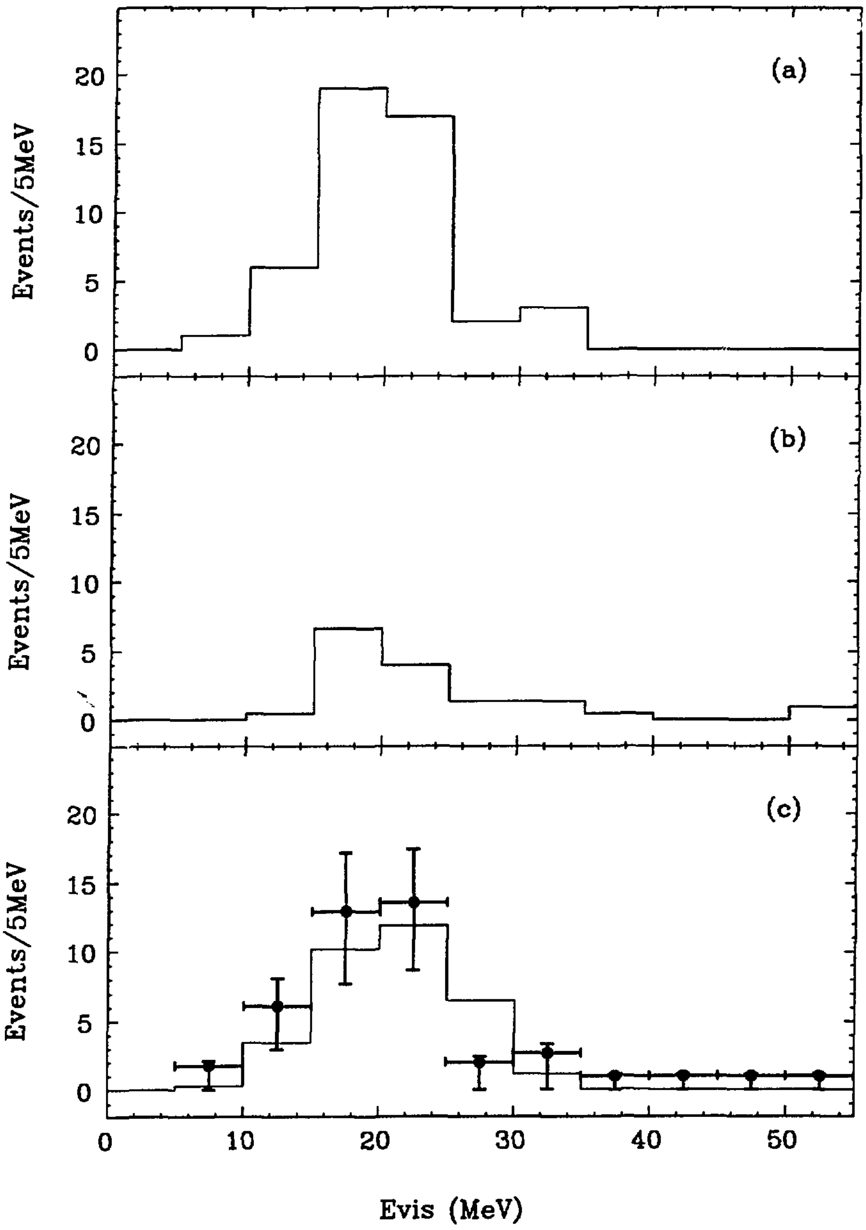

Figure 6.11: The E_{vis} distribution of the DIF neutrino candidates. (a) Beam Gate data. (b) Pre-Beam Gate data normalized to the Beam Gate live time. (c) Beam excess. The histogram, in (c), is the E_{vis} distribution from Monte Carlo generated stopped $\mu^{\pm} \rightarrow e^{\pm}$ events. This histogram is normalized to the number of beam excess events. The last bin on the right contains all events with $E_{vis} \geq$ 50MeV. The procedure used in estimating the points and the vertical "error bars" (68.3% confidence regions) in (c), is described in Appendix B.

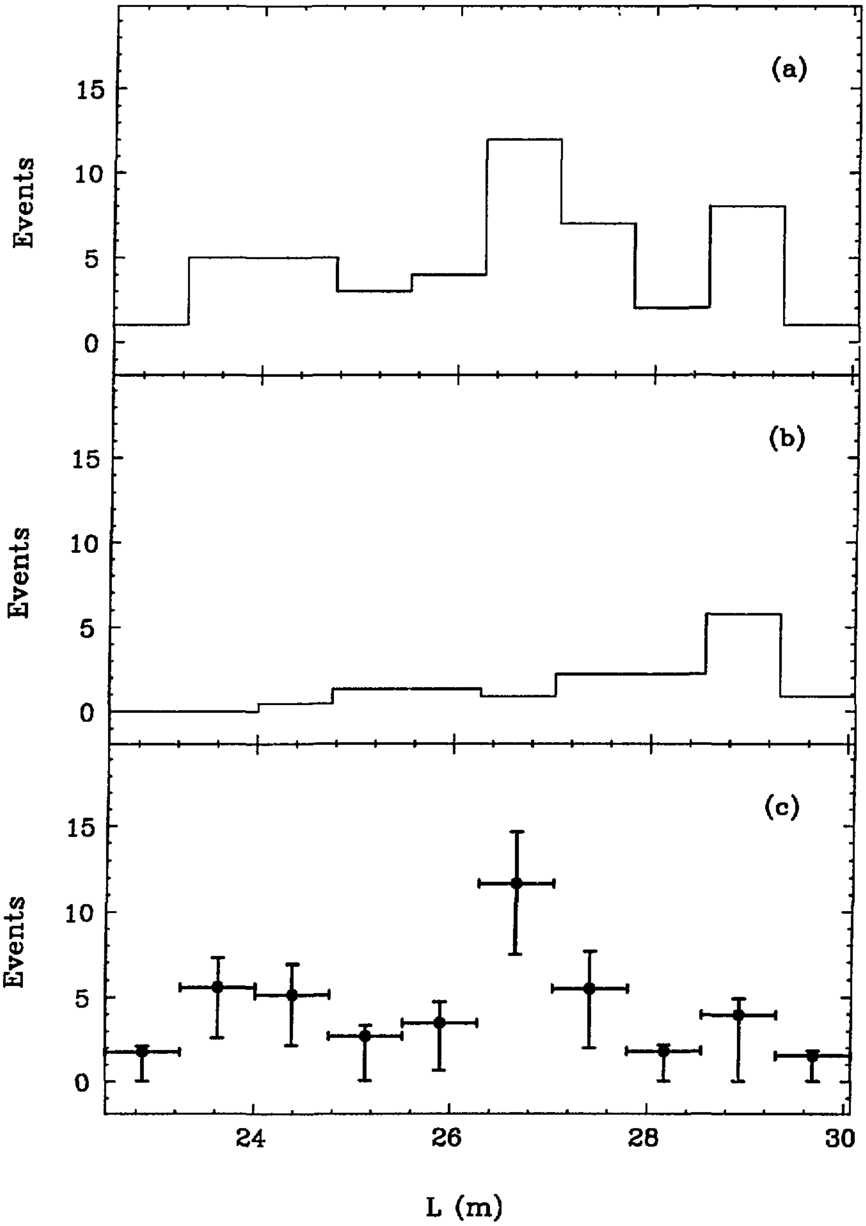

Figure 6.12: The spatial distribution of the DIF neutrino candidates. (a) Beam Gate data. (b) Pre-Beam Gate data normalized to the Beam Gate live time. (c) Beam excess. The spatial parameter "L" is the distance from the A-6 beam stop to the event track, averaged over the track endpoints. The procedure used in estimating the points and the vertical "error bars" (68.3% confidence regions) in (c), is described in Appendix B.

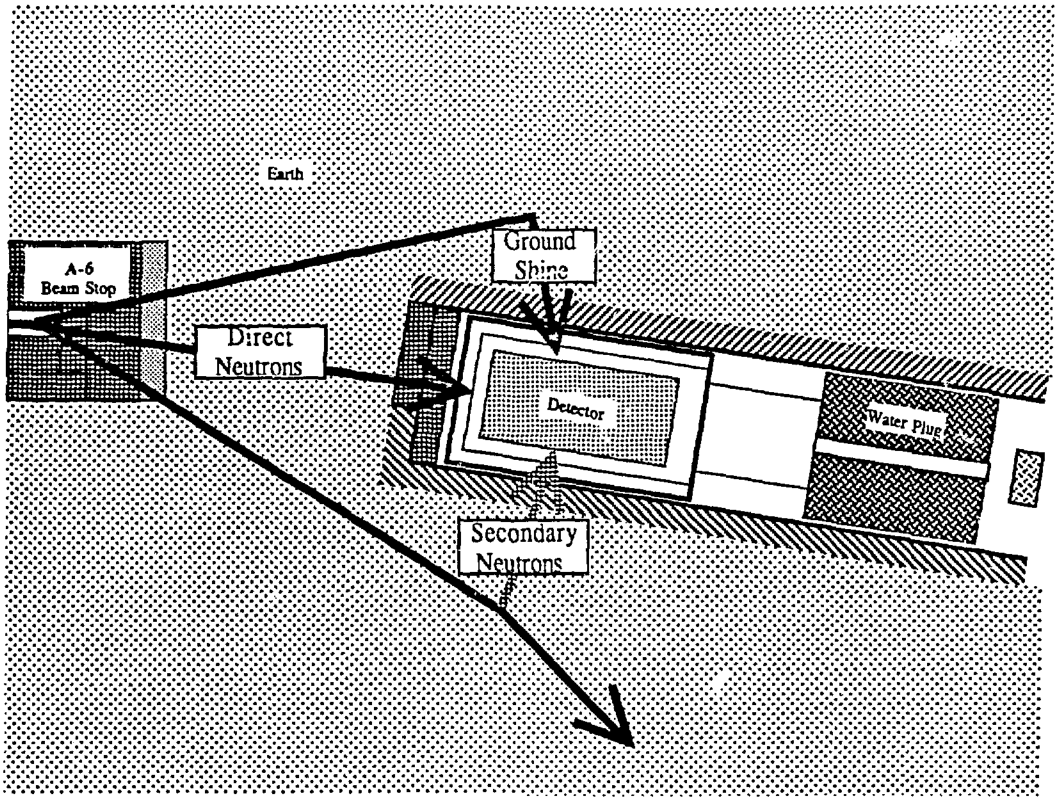

Figure 6.13: Plan view of the neutrino detector relative to the A-6 beam stop. This figure shows that primary beam neutrons may enter the detector directly (direct neutrons) or after scattering (ground shine). In addition, secondary neutrons may also enter the detector.

6.2.4 Beam Neutron Background

We find that, through the observation of charged and neutral pions, there are indications of beam neutrons incident upon a confined region of the central detector. However, we find no evidence of beam neutrons from the examination of recoil protons. The explanation for this result becomes evident through the examination of the ways in which beam neutrons enter the detector. The beam neutron flux incident on the detector consists of primary neutrons that are produced in the A-6 beam stop and secondary neutrons that are produced by the primary neutrons in the shielding. As shown in Figure 6.13, the primary neutrons may enter the detector either through a direct path from the beam stop or through an indirect path where multiple scattering takes place. The direct component of the beam neutron flux consists of the primary neutrons that make a direct path to the detector. The ground shine component consists of both the primary neutrons that scatter into the detector and secondary neutrons.

Neutrons from both the direct flux and the ground shine may interact both elastically and inelastically in the central detector. In approximately one half of the neutron-hydrogen elastic scattering interactions, the recoil proton carries most of the neutron momentum. The acceptance for the recoil protons from direct neutrons is relatively high, because the direct neutrons are energetic (by definition, little momentum was lost through scattering) and the direction of the direct neutron flux is nearly perpendicular to the detector planes. This makes the counting of recoil protons a useful method for estimating the direct neutron flux. However, this method is not as effective for estimating the ground shine flux, because in addition to having less energetic neutrons, the ground shine flux may have components that move in a direction parallel to the detector planes where the acceptance for recoil protons is very low. This component of the ground shine flux will be only visible through the detection of photons, neutral pions, and charged pions from the inelastic reactions. The zero proton beam excess implies that the shielding between the A-6 beam stop and the detector is sufficient to eliminate essentially all of the direct beam neutrons. The beam excess of charged and neutral pions in a confined region of the central detector indicates that the beam neutrons do scatter around this shielding resulting in the observed ground shine.

The important issue is the level of contamination of the beam neutrons into the sample of neutrino events. We will show that the contamination by direct beam neutrons is negligible through the following arguments. The observed recoil proton beam excess is less than 115 events at the 68.3% confidence level. An extremely conservative upper limit on the direct beam neutron contamination may be set by assuming that all of the 87 Pre-Beam Gate neutrino candidates result from cosmic ray neutrons. There are 20498 Pre-Beam Gate proton candidates, so the ability of the detector to remove such events from the neutrino sample is better than 4×10^{-3}. This translates to less than 0.5 neutrino candidates due to direct beam neutrons.

The spatial distribution of the neutrino candidates in Figure 6.4 is relatively uniform and is different from the spatial distribution of the $\pi^0 \rightarrow 2\gamma$ (photon) candidates in Figure 6.9 and the $\pi^\pm \rightarrow \mu^\pm \rightarrow e^\pm$ (DIF neutrino) candidates in Figure 6.12. Therefore, we may conclude that the data analysis has been relatively successful in preventing the ground shine from contaminating the final sample of neutrino candidates.

6.3 Maximum Likelihood Analysis

We perform a maximum likelihood analysis [71] on the neutrino data in order to determine or limit the $\bar{\nu}_\mu \rightarrow \bar{\nu}_e$ oscillation parameters: $\sin^2(2\theta_{\bar{\mu}\bar{e}})$ and $\delta m^2_{\bar{\mu}\bar{e}}$; the $\nu_e \rightarrow \bar{\nu}_{eL}$ oscillation parameters: $\alpha^2 \sin^2(2\theta_{e\bar{e}})$ and $\delta m^2_{e\bar{e}}$; the $\nu_\mu \rightarrow \bar{\nu}_{eL}$ oscillation parameters: $\alpha^2 \sin^2(2\theta_{\mu\bar{e}})$ and $\delta m^2_{\mu\bar{e}}$; and the rare $\mu^+ \rightarrow e^+ \bar{\nu}_e \nu_\mu$ decay branching ratio: R. This analysis is performed under the hypothesis that $\bar{\nu}_e$ appearance may only occur through exactly one of the following processes: $\bar{\nu}_\mu \rightarrow \bar{\nu}_e$ oscillations, $\nu_e \rightarrow \bar{\nu}_{eL}$ oscillations, $\nu_\mu \rightarrow \bar{\nu}_{eL}$ oscillations, and rare $\mu^+ \rightarrow e^+ \bar{\nu}_e \nu_\mu$ decay. We therefore make four separate investigations of $\bar{\nu}_e$ appearance with the following likelihood functions: $\mathcal{L}(\sin^2(2\theta_{\bar{\mu}\bar{e}}), \delta m^2_{\bar{\mu}\bar{e}})$, $\mathcal{L}(\alpha^2 \sin^2(2\theta_{e\bar{e}}), \delta m^2_{e\bar{e}})$, $\mathcal{L}(\alpha^2 \sin^2(2\theta_{\mu\bar{e}}), \delta m^2_{\mu\bar{e}})$, and $\mathcal{L}(R)$. The details of this analysis are given below.

6.3.1 Likelihood Function

We perform the likelihood analysis on the GD0 E_{vis} distribution given in Figure 6.2 and the GD1 E_{vis} distribution given in Figure 6.3. Let there be m_i Beam Gate and m_{0i} Pre-Beam Gate events in each bin i of the GD0 E_{vis} distribution; and let there be n_i Beam Gate and n_{0i} Pre-Beam Gate events in each bin i of the GD1

Bin	E_{vis}		m_i	m_{0i}	n_i	n_{0i}
	Min.	Max.				
$i = 2$	5MeV	10MeV	0	0	0	1
$i = 3$	10MeV	15MeV	10	11	2	1
$i = 4$	15MeV	20MeV	16	23	2	4
$i = 5$	20MeV	25MeV	3	7	0	1
$i = 6$	25MeV	30MeV	4	5	0	0
$i = 7$	30MeV	35MeV	2	4	1	0
$i = 8$	35MeV	40MeV	1	2	1	3
$i = 9$	40MeV	45MeV	1	5	0	1
$i = 10$	45MeV	50MeV	0	3	0	0

Table 6.4: Data used for the maximum likelihood analysis.

E_{vis} distribution. The data used for the likelihood analysis is given in Table 6.4. We consider only the bins from $i = 2$ through $i = 10$, because bin $i = 1$ ($E_{vis} < 5$MeV) is below the threshold of the experiment and $\bar{\nu}_e$ appearance does not contribute events to bins $i > 10$ ($E_{vis} \geq 50$MeV). The experimental results m_i, m_{0i}, n_i, and n_{0i} are drawn from Poisson distributions such that the probability $P(m_i)$ of getting the result m_i, the probability $P(m_{0i})$ of getting the result m_{0i}, the probability $P(n_i)$ of getting the result n_i, and the probability $P(n_{0i})$ of getting the result n_{0i} are equal to

$$P(m_i)=\frac{x_i^{m_i}}{m_i!}e^{-x_i} \tag{6.1}$$

$$P(m_{0i})=\frac{x_{0i}^{m_{0i}}}{m_{0i}!}e^{-x_{0i}} \tag{6.2}$$

$$P(n_i)=\frac{y_i^{n_i}}{n_i!}e^{-y_i} \tag{6.3}$$

$$P(n_{0i})=\frac{y_{0i}^{n_{0i}}}{n_{0i}!}e^{-y_{0i}} \tag{6.4}$$

where x_i, x_{0i}, y_i, and y_{0i} are the predicted number of events. The observation of each m_i, m_{0i}, n_i, and n_{0i} is made independently, so that the joint probability $P(\vec{m}, \vec{m}_0, \vec{n}, \vec{n}_0)$ of obtaining the experimental results $\vec{m} = (m_2, m_3, \ldots, m_{10})$, $\vec{m}_0 = (m_{02}, m_{03}, \ldots, m_{010})$, $\vec{n} = (n_2, n_3, \ldots, n_{10})$, and $\vec{n}_0 = (n_{02}, n_{03}, \ldots, n_{010})$ is equal to

$$P(\vec{m}, \vec{m}_0, \vec{n}, \vec{n}_0) = \prod_{i=2}^{10} \frac{x_i^{m_i}e^{-x_i}}{m_i!}\frac{x_{0i}^{m_{0i}}e^{-x_{0i}}}{m_{0i}!}\frac{y_i^{n_i}e^{-y_i}}{n_i!}\frac{y_{0i}^{n_{0i}}e^{-y_{0i}}}{n_{0i}!} \tag{6.5}$$

The joint probability given in Equation 6.5 is the basic form of the likelihood function.

The number of predicted events, x$_i$ and y$_i$, in the Beam Gate contains the $\bar{\nu}_e$ appearance signal, beam associated background, and cosmic ray background. Explicitly, x$_i$ and y$_i$ are equal to

$$x_i = x_i(\bar{\nu}_e p) + x_i(\nu e^-) + x_i(\nu_e n) + x_i(DIF) + x_i(FBN) + x_i(CR) \tag{6.6}$$

$$y_i = y_i(\bar{\nu}_e p) + y_i(\nu e^-) + y_i(\nu_e n) + y_i(DIF) + y_i(FBN) + y_i(CR) \tag{6.7}$$

where ($\bar{\nu}_e$p) represents the $\bar{\nu}_e$p CC signal from $\bar{\nu}_e$ appearance; (νe^-) represents the $\nu_\mu e^-$, $\nu_e e^-$, and $\bar{\nu}_\mu e^-$elastic scattering background; (ν_en) represents the ν_en CC background; (DIF) represents the DIF ν_μn and $\bar{\nu}_\mu$p CC background; (FBN) represents the fast beam neutron background; and (CR) represents the cosmic ray background. The ($\bar{\nu}_e$p) signal terms depends upon the parameters $\sin^2(2\theta_{\bar{\mu}\bar{e}})$ and $\delta m^2_{\bar{\mu}\bar{e}}$ when investigating $\bar{\nu}_\mu \rightarrow \bar{\nu}_e$ oscillations; the parameters $\alpha^2 \sin^2(2\theta_{e\bar{e}})$ and $\delta m^2_{e\bar{e}}$ when investigating $\nu_e \rightarrow \bar{\nu}_{eL}$ oscillations; the parameters $\alpha^2 \sin^2(2\theta_{\mu\bar{e}})$ and $\delta m^2_{\mu\bar{e}}$ when investigating $\nu_\mu \rightarrow \bar{\nu}_{eL}$ oscillations; and on the branching ratio R when investigating rare $\mu^+ \rightarrow e^+ \bar{\nu}_e \nu_\mu$ decay. Because the Pre-Beam Gate data is used to estimate the cosmic ray background, the (CR) terms are equal to

$$\begin{aligned} x_i(CR) &= \beta x_{0i} \\ y_i(CR) &= \beta y_{0i} \end{aligned} \tag{6.8}$$

where $\beta = 0.442$ is the ratio of the Beam Gate live time to the Pre-Beam Gate live time. From the examination of selected (DIF) and (FBN) samples, we have concluded that the (DIF) and (FBN) contributions to x$_i$ and y$_i$ are negligible

$$\begin{aligned} x_i(DIF) &= y_i(DIF) = 0 \\ x_i(FBN) &= y_i(FBN) = 0 \end{aligned} \tag{6.9}$$

With the inclusion of Equations 6.8 and 6.9, Equations 6.6 and 6.7 reduce to

$$x_i = x_i(\bar{\nu}_e p) + x_i(\nu e^-) + x_i(\nu_e n) + \beta x_{0i} \tag{6.10}$$

$$y_i = y_i(\bar{\nu}_e p) + y_i(\nu e^-) + y_i(\nu_e n) + \beta y_{0i} \tag{6.11}$$

The $(\bar{\nu}_e\mathrm{p})$, the (νe^-), and the $(\nu_e\mathrm{n})$ terms are estimated with the synthetic neutrino analysis described in the previous chapter. There are systematic uncertainties associated with the $(\bar{\nu}_e\mathrm{p})$, (νe^-), and $(\nu_e\mathrm{n})$ terms that require the modification of Equations 6.10 and 6.11. The dominant systematic uncertainties are the neutrino flux (12.4%), the $\nu_e{}^{12}\mathrm{C}$ and $\nu_e{}^{16}\mathrm{O}$ CC cross sections (25%), and the $\nu_e{}^{13}\mathrm{C}$ and $\nu_e{}^{27}\mathrm{Al}$ CC cross sections (50%). We will disregard lesser systematic uncertainties in the $\bar{\nu}_e\mathrm{p}$ CC cross section (2%) and the νe^- elastic scattering cross section ($< 5\%$). We also ignore the statistical uncertainty ($< 2\%$) due to the finite number of synthetic neutrino events used in the evaluation of $(\bar{\nu}_e\mathrm{p})$, (νe^-), and $(\nu_e\mathrm{n})$. With the inclusion of the dominant systematic uncertainties, Equations 6.10 and 6.11 become

$$\begin{aligned} x_i=&(1+s_f)\{x_i(\bar{\nu}_e p)+x_i(\nu e^-)+(1+s_1)[x_i(\nu_e{}^{12}C)+x_i(\nu_e{}^{16}O)] \\ &+(1+s_2)[x_i(\nu_e{}^{13}C)+x_i(\nu_e{}^{27}Al)]\}+\beta x_{0i} \qquad (6.12) \\ y_i=&(1+s_f)\{y_i(\bar{\nu}_e p)+y_i(\nu e^-)+(1+s_1)[y_i(\nu_e{}^{12}C)+y_i(\nu_e{}^{16}O)] \\ &+(1+s_2)[y_i(\nu_e{}^{13}C)+y_i(\nu_e{}^{27}Al)]\}+\beta y_{0i} \qquad (6.13) \end{aligned}$$

where $\mathrm{s_f}$ represents the uncertainty in the neutrino flux, $\mathrm{s_1}$ represents the uncertainty in the $\nu_e{}^{12}\mathrm{C}$ and $\nu_e{}^{16}\mathrm{O}$ CC cross sections, and $\mathrm{s_2}$ represents the uncertainty in the $\nu_e{}^{13}\mathrm{C}$ and $\nu_e{}^{27}\mathrm{Al}$ CC cross sections. Unfortunately, the probability distribution of the systematic variables $\mathrm{s_f}$, $\mathrm{s_1}$, and $\mathrm{s_2}$ are not known. We shall make the naive assumption that $\mathrm{s_f}$, $\mathrm{s_1}$, and $\mathrm{s_2}$ have uniform distributions. Explicitly, the probability distributions of $\mathrm{s_f}$, $\mathrm{s_1}$, and $\mathrm{s_2}$ are equal to

$$P(s_f)=\frac{1}{2\sqrt{3}\sigma_f}\Theta(s_f+\sqrt{3}\sigma_f)\Theta(\sqrt{3}\sigma_f-s_f) \qquad (6.14)$$

$$P(s_1)=\frac{1}{2\sqrt{3}\sigma_1}\Theta(s_1+\sqrt{3}\sigma_1)\Theta(\sqrt{3}\sigma_1-s_1) \qquad (6.15)$$

$$P(s_2)=\frac{1}{2\sqrt{3}\sigma_2}\Theta(s_2+\sqrt{3}\sigma_2)\Theta(\sqrt{3}\sigma_2-s_2) \qquad (6.16)$$

where $\Theta(s)$ is the *Heaviside* unit function, $\sigma_\mathrm{f} = 0.124$ is the standard deviation of $\mathrm{s_f}$, $\sigma_1 = 0.25$ is the standard deviation of $\mathrm{s_1}$, and $\sigma_2 = 0.50$ is the standard deviation of $\mathrm{s_2}$.

It is possible to remove the beam associated background terms (νe^-) and (ν_en) in Equations 6.10 and 6.11. We introduce the quantities S_i and B_i, which are defined as

$$S_i \equiv x_i(\bar{\nu}_e p) + y_i(\bar{\nu}_e p) \tag{6.17}$$

$$B_i \equiv x_i(\nu e^-) + x_i(\nu_e n) + y_i(\nu e^-) + y_i(\nu_e n) \tag{6.18}$$

We also define ϵ_n to be the probability of detecting a delayed Gd-capture coincidence for the $\bar{\nu}_e$p CC signal and r_n to be the probability of detecting a delayed Gd-capture coincidence for the νe^- elastic scattering and ν_en CC background. The synthetic neutrino analysis predicts $\epsilon_n = 0.359$ for full strength $\bar{\nu}_\mu \rightarrow \bar{\nu}_e$ oscillation events and $r_n = 0.128$. With the above definitions, Equations 6.10 and 6.11 may be rewritten as

$$x_i = \bar{\epsilon}_n S_i + \bar{r}_n B_i + \beta x_{0i} \tag{6.19}$$

$$y_i = \epsilon_n S_i + r_n B_i + \beta y_{0i} \tag{6.20}$$

where $\bar{\epsilon}_n \equiv 1 - \epsilon_n$ and $\bar{r}_n \equiv 1 - r_n$. Given that $\epsilon_n \neq r_n$, Equations 6.19 and 6.20 provide us with a pair of nonsingular equations for which we may eliminate B_i and solve for S_i.

Given the joint probability in Equation 6.5, we shall write down the ***Background Model Dependent*** (BMD) likelihood functions and the ***Background Model Independent*** (BMI) likelihood functions. The BMD likelihood functions are equal to

$$\left.\begin{matrix} \mathcal{L}^{BMD}(\sin^2(2\theta_{\bar{\mu}\bar{e}}), \delta m^2_{\bar{\mu}\bar{e}}) \\ \mathcal{L}^{BMD}(\alpha^2 \sin^2(2\theta_{e\bar{e}}), \delta m^2_{e\bar{e}}) \\ \mathcal{L}^{BMD}(\alpha^2 \sin^2(2\theta_{\mu\bar{e}}), \delta m^2_{\mu\bar{e}}) \\ \mathcal{L}^{BMD}(R) \end{matrix}\right\} = \begin{array}{r} \frac{1}{2\sqrt{3}\sigma_f} \int_{-\sqrt{3}\sigma_f}^{+\sqrt{3}\sigma_f} ds_f \frac{1}{2\sqrt{3}\sigma_1} \int_{-\sqrt{3}\sigma_1}^{+\sqrt{3}\sigma_1} ds_1 \frac{1}{2\sqrt{3}\sigma_2} \int_{-\sqrt{3}\sigma_2}^{+\sqrt{3}\sigma_2} ds_2 \\ \times \prod_{i=2}^{10} \{ [\int_0^\infty dx_{0i} \frac{x_i^{m_i} e^{-x_i}}{m_i!} \frac{x_{0i}^{m_{0i}} e^{-x_{0i}}}{m_{0i}!}] \\ \times [\int_0^\infty dy_{0i} \frac{y_i^{n_i} e^{-y_i}}{n_i!} \frac{y_{0i}^{n_{0i}} e^{-y_{0i}}}{n_{0i}!}] \} \end{array} \tag{6.21}$$

where x_i and y_i are given by Equations 6.12 and 6.13 respectively; and the unobserved s_f, s_1, s_2, x_{0i}, and y_{0i} are removed through integration. The BMD likelihood functions require the calculation of the beam associated background terms (νe^-) and (ν_en). The BMI likelihood functions are equal to

$$\left.\begin{array}{c} \mathcal{L}^{BMI}(\sin^2(2\theta_{\bar{\mu}\bar{e}}), \delta m^2_{\bar{\mu}\bar{e}}) \\ \mathcal{L}^{BMI}(\alpha^2 \sin^2(2\theta_{e\bar{e}}), \delta m^2_{e\bar{e}}) \\ \mathcal{L}^{BMI}(\alpha^2 \sin^2(2\theta_{\mu\bar{e}}), \delta m^2_{\mu\bar{e}}) \\ \mathcal{L}^{BMI}(R) \end{array}\right\} = \begin{array}{r} \frac{1}{2\sqrt{3}\sigma_f} \int_{-\sqrt{3}\sigma_f}^{+\sqrt{3}\sigma_f} ds_f \prod_{i=2}^{10} \int_0^\infty dB_i \{ \\ \times[\int_0^\infty dx_{0i} \frac{x_i^{m_i} e^{-x_i}}{m_i!} \frac{x_{0i}^{m_{0i}} e^{-x_{0i}}}{m_{0i}!}] \\ \times[\int_0^\infty dy_{0i} \frac{y_i^{n_i} e^{-y_i}}{n_i!} \frac{y_{0i}^{n_{0i}} e^{-y_{0i}}}{n_{0i}!}]\} \end{array} \quad (6.22)$$

where x$_i$ and y$_i$ are given by

$$x_i = (1 + s_f) x_i(\bar{\nu}_e p) + \tilde{r}_n B_i + \beta x_{0i} \quad (6.23)$$

$$y_i = (1 + s_f) y_i(\bar{\nu}_e p) + r_n B_i + \beta y_{0i} \quad (6.24)$$

and the unobserved s$_f$, B$_i$, x$_{0i}$, and y$_{0i}$ are removed through integration. The BMI likelihood function is independent of the calculated values of the beam associated background terms (νe^-) and (ν_en). In fact the BMI likelihood functions are nearly independent of the composition, the shape, and the normalization of the beam associated background. Because νe^- elastic scattering and ν_en CC reactions do not have final state neutrons, r$_n$ is actually the probability of detecting an accidental Gd-capture coincidence. Therefore, B$_i$ represents all beam associated background reactions that do not have detectable final state neutrons.

6.3.2 Maximum Likelihood

We use the grid search method [72] to determine the maximum likelihood $\bar{\nu}_e$ appearance parameters. This search is confined to the physical region, where the $\bar{\nu}_e$ appearance parameters have the following bounds

$$\begin{array}{rcc} \bar{\nu}_\mu \rightarrow \bar{\nu}_e \text{ oscillations:} & 0 \leq \sin^2(2\theta_{\bar{\mu}\bar{e}}) \leq 1 & 0 \leq \delta m^2_{\bar{\mu}\bar{e}} < \infty \\ \nu_e \rightarrow \bar{\nu}_{eL} \text{ oscillations:} & 0 \leq \alpha^2 \sin^2(2\theta_{e\bar{e}}) \leq 1 & 0 \leq \delta m^2_{e\bar{e}} < \infty \\ \nu_\mu \rightarrow \bar{\nu}_{eL} \text{ oscillations:} & 0 \leq \alpha^2 \sin^2(2\theta_{\mu\bar{e}}) \leq 1 & 0 \leq \delta m^2_{\mu\bar{e}} < \infty \\ \mu^+ \rightarrow e^+ \bar{\nu}_e \nu_\mu \text{ decay:} & \multicolumn{2}{c}{0 \leq R \leq 1} \end{array}$$

In the search for $\bar{\nu}_\mu \rightarrow \bar{\nu}_e$ oscillations, the BMD and BMI likelihood functions are sampled on a 500 point by 500 point linear $\sin^2(2\theta_{\bar{\mu}\bar{e}}) \otimes \delta m^2_{\bar{\mu}\bar{e}}$ grid in the interval

$$\begin{aligned} 0 \leq \sin^2(2\theta_{\bar{\mu}\bar{e}}) \leq 1 \\ 0 \leq \delta m^2_{\bar{\mu}\bar{e}} \leq 100\mathrm{eV}^2 \end{aligned} \tag{6.25}$$

The large-$\delta m^2_{\bar{\mu}\bar{e}}$ ($\delta m^2_{\bar{\mu}\bar{e}} > 100\mathrm{eV}^2$) region, where the likelihood functions are essentially independent of $\delta m^2_{\bar{\mu}\bar{e}}$, is not examined. On the above grid we find that for both the BMD and BMI likelihood functions, the likelihood is maximum when either $\sin^2(2\theta_{\bar{\mu}\bar{e}}) = 0$ or $\delta m^2_{\bar{\mu}\bar{e}} = 0$, i.e., the experimental data gives the maximum likelihood with the no $\bar{\nu}_\mu \rightarrow \bar{\nu}_e$ oscillations hypothesis. This confirms the conclusion drawn from the visual inspection of the $\mathrm{E_{vis}}$ distribution of the neutrino candidates given in Figure 6.1.

The likelihood functions are sampled on similar grids in the search for $\nu_e \rightarrow \bar{\nu}_{eL}$ and $\nu_\mu \rightarrow \bar{\nu}_{eL}$ oscillations. We find that, for both of these oscillation modes, the no neutrino oscillation hypothesis:

$$\begin{aligned} \nu_e \rightarrow \bar{\nu}_{eL} \text{ oscillations:} \quad & \alpha^2 \sin^2(2\theta_{e\bar{e}}) = 0 \text{ or } \delta m^2_{e\bar{e}} = 0 \\ \nu_\mu \rightarrow \bar{\nu}_{eL} \text{ oscillations:} \quad & \alpha^2 \sin^2(2\theta_{\mu\bar{e}}) = 0 \text{ or } \delta m^2_{\mu\bar{e}} = 0 \end{aligned}$$

gives the maximum likelihood.

In the search for rare $\mu^+ \rightarrow e^+\bar{\nu}_e\nu_\mu$ decay, the likelihood functions are sampled on 10,000 equidistant points in the interval $0 \leq \mathrm{R} \leq 1$. We find that both the BMD and BMI likelihood functions are maximum at $\mathrm{R} = 0$.

6.3.3 90% Confidence Region

The 90% confidence region for the $\bar{\nu}_\mu \rightarrow \bar{\nu}_e$ oscillation parameters $\sin^2(2\theta_{\bar{\mu}\bar{e}})$ and $\delta m^2_{\bar{\mu}\bar{e}}$ is defined by a surface in $\sin^2(2\theta_{\bar{\mu}\bar{e}}) \otimes \delta m^2_{\bar{\mu}\bar{e}}$ space that contains the maximum likelihood parameters. Because the maximum likelihood parameters lie on the physical boundary, the 90% confidence region is bounded below by the contours corresponding to $\sin^2(2\theta_{\bar{\mu}\bar{e}}) = 0$ and $\delta m^2_{\bar{\mu}\bar{e}} = 0$. The 90% confidence region is bounded above by a contour of constant likelihood. It is convenient to define the contours in terms of constant log-likelihood ratios

$$\Delta\chi^2 \equiv -2\ln(\frac{\mathcal{L}}{\mathcal{L}_{\max}}) \tag{6.26}$$

where $\mathcal{L}_{\max}$ is the likelihood function evaluated at the maximum likelihood parameters. The 90% confidence level (C.L.) $\Delta\chi^2$ contour is estimated with a technique suggested by the *Particle Data Group* [39]. The likelihood function is renormalized to the physical region and the solution of the following equation

$$\begin{gathered}\oint_{\Delta\chi^2} d(\sin^2(2\theta_{\bar{\mu}\bar{e}}))d(\delta m^2_{\bar{\mu}\bar{e}})\mathcal{L}(\sin^2(2\theta_{\bar{\mu}\bar{e}}),\delta m^2_{\bar{\mu}\bar{e}}) = \\ (0.90)\int_0^1 d(\sin^2(2\theta_{\bar{\mu}\bar{e}}))\int_0^\infty d(\delta m^2_{\bar{\mu}\bar{e}})\mathcal{L}(\sin^2(2\theta_{\bar{\mu}\bar{e}}),\delta m^2_{\bar{\mu}\bar{e}})\end{gathered} \tag{6.27}$$

defines the 90% C.L. $\Delta\chi^2$ contour. The exact determination of $\Delta\chi^2$ is impossible because the integral on the right hand side of Equation 6.27 diverges. We determine an approximation to $\Delta\chi^2$ by taking advantage of the behaviour of the likelihood function at large-$\delta m^2_{\bar{\mu}\bar{e}}$ ($\delta m^2_{\bar{\mu}\bar{e}} > 100\text{eV}^2$), where the oscillation probability

$$\sin^2(2\theta_{\bar{\mu}\bar{e}})\sin^2(1.27\frac{\delta m^2_{\bar{\mu}\bar{e}}l}{E_\nu}) \rightarrow \frac{1}{2}\sin^2(2\theta_{\bar{\mu}\bar{e}}) \tag{6.28}$$

becomes independent of $\delta m^2_{\bar{\mu}\bar{e}}$. The reduced likelihood function $\tilde{\mathcal{L}}$, which is defined to be the likelihood function at large $\delta m^2_{\bar{\mu}\bar{e}}$

$$\tilde{\mathcal{L}}(\sin^2(2\theta_{\bar{\mu}\bar{e}})) \equiv \mathcal{L}(\sin^2(2\theta_{\bar{\mu}\bar{e}}),\delta m^2_{\bar{\mu}\bar{e}} > 100\text{eV}^2) \tag{6.29}$$

depends only on the single parameter $\sin^2(2\theta_{\bar{\mu}\bar{e}})$. The 90% confidence interval on $\sin^2(2\theta_{\bar{\mu}\bar{e}})$ with the reduced likelihood function is defined by

$$0 \leq \sin^2(2\theta_{\bar{\mu}\bar{e}}) \leq \overline{\sin^2(2\theta_{\bar{\mu}\bar{e}})} \tag{6.30}$$

where the upper bound $\overline{\sin^2(2\theta_{\bar{\mu}\bar{e}})}$ is solution of

$$\int_0^{\overline{\sin^2(2\theta_{\bar{\mu}\bar{e}})}} d(\sin^2(2\theta_{\bar{\mu}\bar{e}}))\tilde{\mathcal{L}}(\sin^2(2\theta_{\bar{\mu}\bar{e}})) = (0.90)\int_0^1 d(\sin^2(2\theta_{\bar{\mu}\bar{e}}))\tilde{\mathcal{L}}(\sin^2(2\theta_{\bar{\mu}\bar{e}})) \tag{6.31}$$

Oscillation Mode	$\Delta\chi^2$(90%C.L.) BMD	$\Delta\chi^2$(90%C.L.) BMI
$\bar{\nu}_\mu \rightarrow \bar{\nu}_e$	4.37	4.36
$\nu_e \rightarrow \bar{\nu}_{eL}$	4.40	4.29
$\nu_\mu \rightarrow \bar{\nu}_{eL}$	4.07	3.34

Table 6.5: The 90% confidence level (C.L.) $\Delta\chi^2$ contours for the BMD and BMI $\bar{\nu}_\mu, \nu_e, \nu_\mu \rightarrow \bar{\nu}_e$ oscillation likelihood functions.

This equation, which is solved numerically, results in $\overline{\sin^2(2\theta_{\bar{\mu}\bar{e}})} = 1.91 \times 10^{-2}$ for the BMD likelihood function and $\overline{\sin^2(2\theta_{\bar{\mu}\bar{e}})} = 1.89 \times 10^{-2}$ for the BMI likelihood function. The 90% confidence region corresponds to contours of constant

$$\Delta\chi^2 = -2\ln(\frac{\tilde{\mathcal{L}}(\overline{\sin^2(2\theta_{\bar{\mu}\bar{e}})})}{\mathcal{L}_{\mathrm{max}}}) \tag{6.32}$$

The resultant 90% C.L. $\Delta\chi^2$ contours are given in Table 6.5. The 90% C.L. contours for $\nu_e \rightarrow \bar{\nu}_{eL}$ oscillations and $\nu_\mu \rightarrow \bar{\nu}_{eL}$ oscillations, which are obtained through a similar analysis, are also given in Table 6.5.

The 90% confidence interval on the rare $\mu^+ \rightarrow e^+\bar{\nu}_e\nu_\mu$ decay branching ratio, R, is defined by the interval

$$0 \leq R \leq \bar{R} \tag{6.33}$$

where R̄ is the 90% C.L. upper bound on R. In analogy with Equation 6.31, the 90% C.L. upper bound R̄ is the solution of the following equation

$$\int_0^{\bar{R}} dR\mathcal{L}(R) = (0.90) \int_0^1 dR\mathcal{L}(R) \tag{6.34}$$

This equation is solved numerically and results in $\bar{\mathrm{R}} = 9.54 \times 10^{-3}$ for the BMD likelihood function and $\bar{\mathrm{R}} = 9.45 \times 10^{-3}$ for the BMI likelihood function.

6.4 Results

The 90% confidence level (C.L.) limits on the $\bar{\nu}_e$ appearance parameters obtained from the above analysis are given in Table 6.6. The 90% C.L. contours on $\bar{\nu}_\mu \rightarrow \bar{\nu}_e$,

$\bar{\nu}_\mu \rightarrow \bar{\nu}_e$	BMD	$\delta m^2_{\bar{\mu}\bar{e}} \leq 0.128\mathrm{eV}^2$	for $\sin^2(2\theta_{\bar{\mu}\bar{e}}) = 1$
		$\sin^2(2\theta_{\bar{\mu}\bar{e}}) \leq 1.91 \times 10^{-2}$	for large $\delta m^2_{\bar{\mu}\bar{e}}$
	BMI	$\delta m^2_{\bar{\mu}\bar{e}} \leq 0.132\mathrm{eV}^2$	for $\sin^2(2\theta_{\bar{\mu}\bar{e}}) = 1$
		$\sin^2(2\theta_{\bar{\mu}\bar{e}}) \leq 1.89 \times 10^{-2}$	for large $\delta m^2_{\bar{\mu}\bar{e}}$
$\nu_e \rightarrow \bar{\nu}_{eL}$	BMD	$\alpha\delta m^2_{e\bar{e}} \leq 0.143\mathrm{eV}^2$	for $\sin^2(2\theta_{e\bar{e}}) = 1$
		$\alpha^2 \sin^2(2\theta_{e\bar{e}}) \leq 2.90 \times 10^{-2}$	for large $\delta m^2_{e\bar{e}}$
	BMI	$\alpha\delta m^2_{e\bar{e}} \leq 0.156\mathrm{eV}^2$	for $\sin^2(2\theta_{e\bar{e}}) = 1$
		$\alpha^2 \sin^2(2\theta_{e\bar{e}}) \leq 3.20 \times 10^{-2}$	for large $\delta m^2_{e\bar{e}}$
$\nu_\mu \rightarrow \bar{\nu}_{eL}$	BMD	$\alpha\delta m^2_{\mu\bar{e}} \leq 0.159\mathrm{eV}^2$	for $\sin^2(2\theta_{\mu\bar{e}}) = 1$
		$\alpha^2 \sin^2(2\theta_{\mu\bar{e}}) \leq 6.17 \times 10^{-2}$	for large $\delta m^2_{\mu\bar{e}}$
	BMI	$\alpha\delta m^2_{\mu\bar{e}} \leq 0.191\mathrm{eV}^2$	for $\sin^2(2\theta_{\mu\bar{e}}) = 1$
		$\alpha^2 \sin^2(2\theta_{\mu\bar{e}}) \leq 8.78 \times 10^{-2}$	for large $\delta m^2_{\mu\bar{e}}$
$\mu^+ \rightarrow e^+\bar{\nu}_e\nu_\mu$	BMD	$\mathrm{R} \leq 9.54 \times 10^{-3}$	
	BMI	$\mathrm{R} \leq 9.45 \times 10^{-3}$	

Table 6.6: The 90% confidence level (C.L.) limits on the $\bar{\nu}_e$ appearance parameters obtained from this experiment (LAMPF E645).

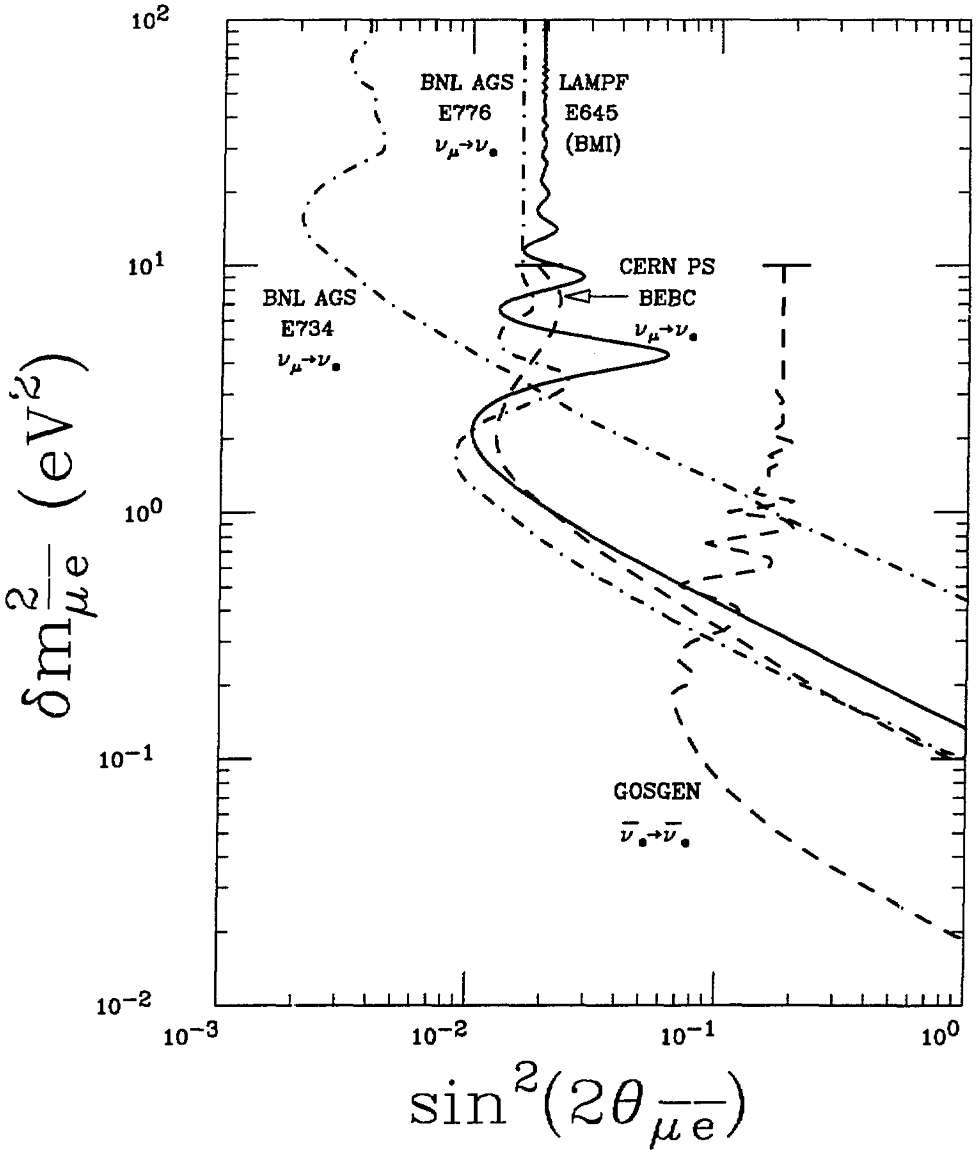

Figure 6.14: The 90% confidence level (C.L.) limits on the $\bar{\nu}_\mu \to \bar{\nu}_e$ oscillation parameters from this experiment (LAMPF E645) with the BMI likelihood function. Both the BMD and BMI likelihood functions give similar limits. For comparison, we include recent limits on $\nu_\mu \to \nu_e$ oscillations from BNL AGS E732 [74], CERN PS BEBC [75], and BNL AGS E776 [76]. We also include limits on $\bar{\nu}_e \to \bar{\nu}_e$ ($\bar{\nu}_e$ disappearance) from Gösgen [78]. All of the above curves exclude the region to the right.

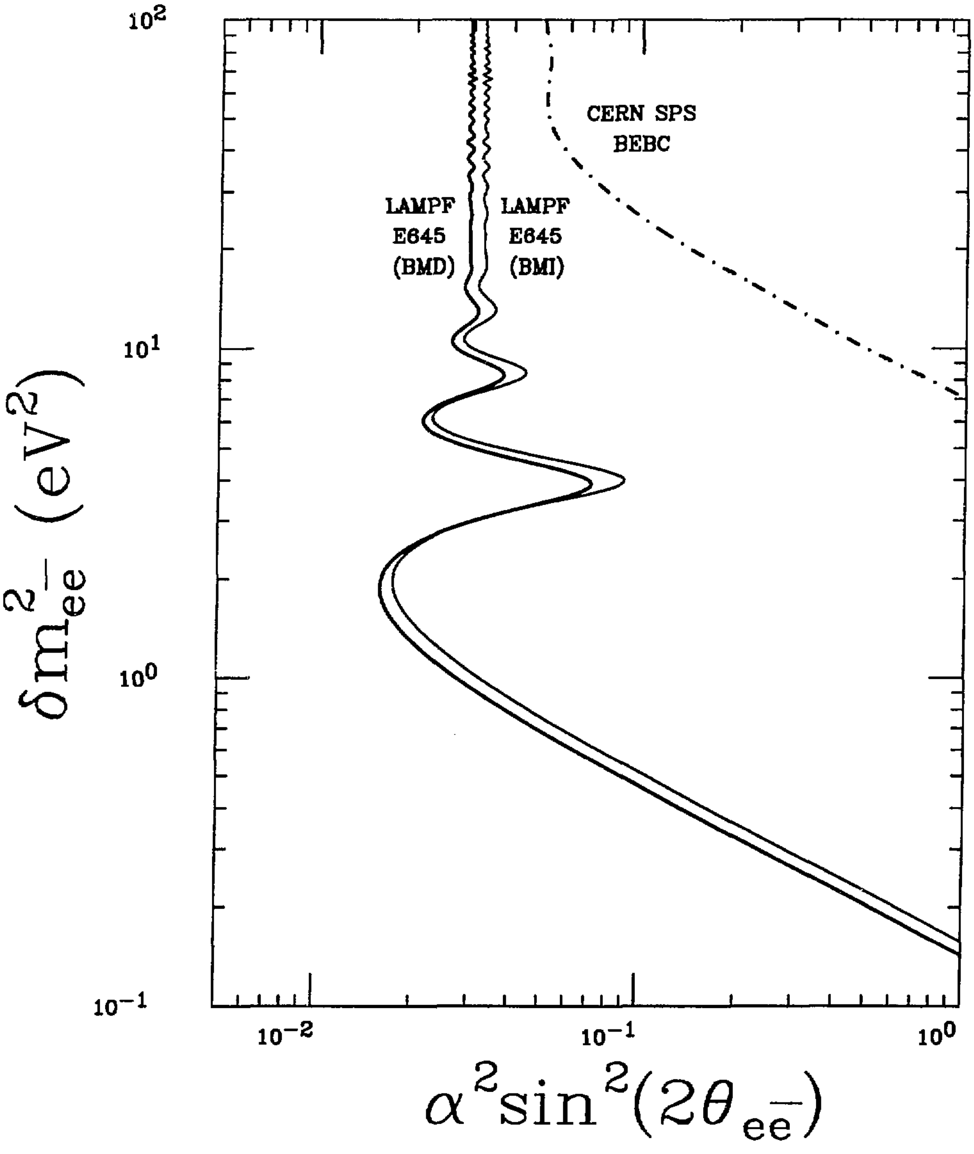

Figure 6.15: The 90% confidence level (C.L.) limits on the $\nu_e \rightarrow \bar{\nu}_{eL}$ oscillation parameters from this experiment (LAMPF E645). The limits obtained from the BMD and BMI likelihood functions are displayed separately. For comparison, we include previous limits on $\nu_e \rightarrow \bar{\nu}_{eL}$ oscillations from CERN SPS BEBC [77]. All of the above curves exclude the region to the right.

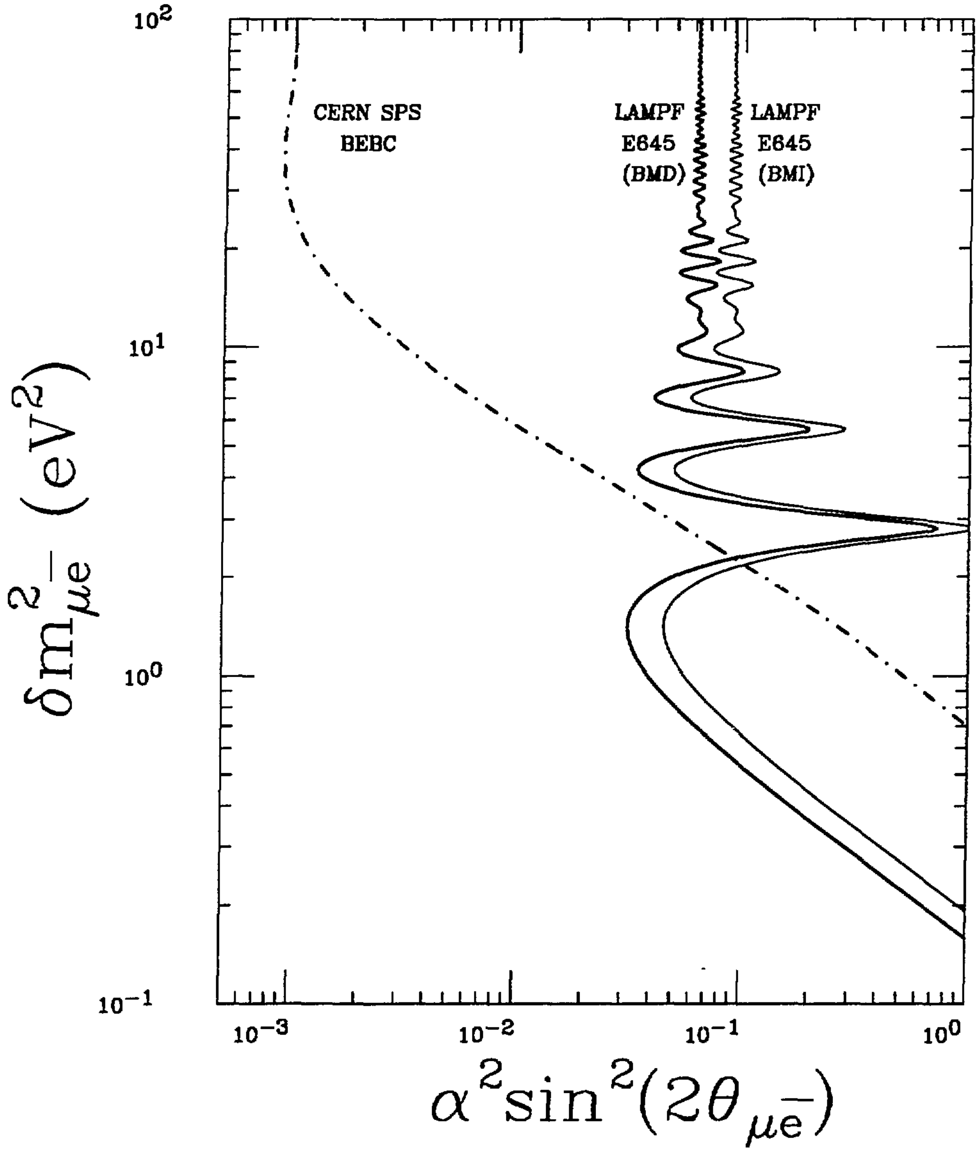

Figure 6.16: *The 90% confidence level (C.L.) limits on the* $\nu_\mu \rightarrow \bar{\nu}_{eL}$ *oscillation* parameters from this experiment (LAMPF E645). The limits obtained from the BMD and BMI likelihood functions are displayed separately. For comparison, we include previous limits on $\nu_\mu \rightarrow \bar{\nu}_{eL}$ oscillations from CERN SPS BEBC [77]. All of the above curves exclude the region to the right.

$\nu_e \rightarrow \bar{\nu}_{eL}$, and $\nu_\mu \rightarrow \bar{\nu}_{eL}$ oscillations are given in Figures 6.14, 6.15, and 6.16 respectively. Limits on $\nu_\mu \rightarrow \nu_e$ oscillations, which are equivalent to $\bar{\nu}_\mu \rightarrow \bar{\nu}_e$ oscillations in the two neutrino mixing hypothesis, from the Brookhaven experiment E734 [74], BEBC collaboration at CERN [75], and the Brookhaven experiment E776 [76] are included in Figure 6.14 for comparison. Recent limits on $\bar{\nu}_e \rightarrow \bar{\nu}_e$ oscillations ($\bar{\nu}_e$ disappearance), from Gösgen [78], are also shown in Figure 6.14. Previous limits on $\nu_e \rightarrow \bar{\nu}_{eL}$ and $\nu_\mu \rightarrow \bar{\nu}_{eL}$ oscillations from the BEBC collaboration at CERN [77] are shown in Figures 6.15 and 6.16 respectively.

We have obtained limits on $\bar{\nu}_\mu \rightarrow \bar{\nu}_e$ oscillations, which are comparable to the $\bar{\nu}_\mu \rightarrow \bar{\nu}_e$ oscillations limits from BEBC collaboration at CERN [75] and the Brookhaven experiment E776 [76]. The limits on $\nu_e \rightarrow \bar{\nu}_{eL}$ oscillations show an improvement, for both large and small $\delta m^2_{e\bar{e}}$, over previous limits from the BEBC collaboration at CERN [77]. However, the excluded region has been previously rejected by ν_e disappearance experiments [79,80,81]. If CP is conserved, then the excluded region is also rejected by the $\bar{\nu}_e$ disappearance experiment at Gösgen [78]. In addition, the experimental searches for neutrinoless double beta decay [23,24], with or without majoron emission, indicate that the parameter $\alpha^2 \sin^2(2\theta_{e\bar{e}})$ is very small. The limits on $\nu_\mu \rightarrow \bar{\nu}_{eL}$ oscillations show an improvement, for small $\delta m^2_{\mu\bar{e}}$, over previous limits from the BEBC collaboration at CERN [77]. However, the excluded region has been previously rejected by ν_μ disappearance experiments [82,83]. The limit on the rare $\mu^+ \rightarrow e^+\bar{\nu}_e\nu_\mu$ decay branching ratio: R $< 9.5 \times 10^{-3}$ (90% C.L.), is an order of magnitude improvement over the previous limits of R $< 9.8 \times 10^{-2}$ (90% C.L.) from the LAMPF experiment E31 [32] and a factor of five improvement over limits of R $< 5 \times 10^{-2}$ (90% C.L.) for the inverse reaction $\bar{\nu}_\mu e^- \rightarrow \mu^-\bar{\nu}_e$ from the CHARM collaboration at CERN [33].

Chapter 7

Summary and Conclusions

We have performed an experiment to search for $\bar{\nu}_e$ appearance from stopped π^+ and μ^+ decay at LAMPF. The appearance of $\bar{\nu}_e$ may occur from $\bar{\nu}_\mu \rightarrow \bar{\nu}_e$ oscillations, $\nu_e \rightarrow \bar{\nu}_{eL}$ oscillations, $\nu_\mu \rightarrow \bar{\nu}_{eL}$ oscillations, or rare $\mu^+ \rightarrow e^+\bar{\nu}_e\nu_\mu$ decay. No evidence for $\bar{\nu}_e$ appearance was observed and new limits on the $\bar{\nu}_\mu, \nu_e, \nu_\mu \rightarrow \bar{\nu}_e$ oscillation parameters and the rare $\mu^+ \rightarrow e^+\bar{\nu}_e\nu_\mu$ decay branching ratio are obtained. The limits on $\bar{\nu}_\mu \rightarrow \bar{\nu}_e$ oscillations are comparable to recent limits on $\nu_\mu \rightarrow \nu_e$ oscillations from the BEBC collaboration at CERN [75] and from the Brookhaven experiment E776 [76]. The limits on $\nu_e \rightarrow \bar{\nu}_{eL}$ oscillations show an improvement, for both large and small $\delta m^2_{e\bar{e}}$, over previous limits from the BEBC collaboration at CERN [77]. However, the excluded region has been previously rejected by ν_e disappearance experiments [79,80,81]. If CP is conserved, then the excluded region is also rejected by the $\bar{\nu}_e$ disappearance experiment at Gösgen [78]. In addition, the experimental searches for neutrinoless double beta decay [23,24], with or without majoron emission, indicate that the parameter $\alpha^2 \sin^2(2\theta_{e\bar{e}})$ is very small. The limits on $\nu_\mu \rightarrow \bar{\nu}_{eL}$ oscillations show an improvement, for small $\delta m^2_{\mu\bar{e}}$, over previous limits from the BEBC collaboration at CERN [77]. However, the excluded region has been previously rejected by ν_μ disappearance experiments [82,83]. The limit on the rare $\mu^+ \rightarrow e^+\bar{\nu}_e\nu_\mu$ decay branching ratio: R $< 9.5 \times 10^{-3}$ (90% C.L.), is an order of magnitude improvement over the previous limits of R $< 9.8 \times 10^{-2}$ (90% C.L.) from the LAMPF experiment E31 [32] and a factor of five improvement over limits on the inverse reaction $\bar{\nu}_\mu e^- \rightarrow \mu^- \bar{\nu}_e$ from the CHARM collaboration at CERN [33].

There is a deficiency of -20.8 ± 10.1 events in the number of observed beam excess neutrino candidates compared to a prediction which assumes that the beam excess is due to ν_en CC and νe^- elastic scattering events. An independent analysis performed on the same data sample results in a similar beam excess deficiency of -10.2 ± 6.0 events [73]. This deficiency may indicate that the neutrino acceptance or the neutrino flux may be overestimated, which calls into question the above limits. Neutrino data from 1988 and 1989, which remain to be analyzed, will reveal whether the deficiency is a statistical fluctuation or a real problem with the neutrino acceptance or the neutrino source. Calibration experiments are being planned to investigate the acceptance of the E645 detector. The normalization of the neutrino flux is currently being investigated by LAMPF experiment E866 [85].

Finally, we have found evidence of ground shine neutrons incident upon the detector. The data analysis, which took advantage of the particle identification capabilities of the detector, was successful in preventing the contamination of the ground shine into the sample of neutrino candidates. However, the ground shine background may be a major problem for future neutrino experiments [84] planned for the existing E645 neutrino tunnel.

Appendix A

Muon Lifetime

The mean lifetime of cosmic ray muons that stop in the E645 central detector is less than the free muon mean lifetime. This is due to the competition of muon decay with μ^- capture. We estimate the muon mean lifetime in the central detector using measured μ^- mean lifetimes [38] and the detector composition given in Table A.1. Assuming a cosmic ray muon flux constituent of approximately 56% μ^+ and 44% μ^- [39], the muon mean lifetime in the central detector $\tau_\mu^{(E645)}$, is equal to

$$\frac{1}{\tau_\mu^{(E645)}} = (0.56)\frac{1}{\tau_{\mu^+}} + (0.44)\sum_Z f^{(Z)}\frac{1}{\tau_{\mu^-}^{(Z)}} \tag{A.1}$$

where $\tau_{\mu^+} = 2.197\mu s$ is the μ^+ mean lifetime, $\tau_{\mu^-}^{(Z)}$ is the μ^- mean lifetime in element "Z" from Reference [38], and $f^{(Z)}$ is the relative number of atoms of element "Z". Numerical evaluation of Equation A.1 results in a muon mean lifetime of $\tau_\mu^{(E645)} = 2.15\mu s$.

Element (Z)	Number of Atoms	$f^{(Z)}$
H	1.54×10^{30}	0.610
C	8.29×10^{29}	0.327
O	1.49×10^{29}	0.058
Al	6.35×10^{27}	0.003
Gd	2.05×10^{26}	$< 10^{-4}$

Table A.1: The E645 detector composition used in the estimation of the muon mean lifetime.

Appendix B

Point Estimation

A common problem encountered in this experiment is the estimation of a signal given a measurement of signal plus background and an independent measurement of only the background. For example, given an observation of n Beam Gate events and n_0 Pre-Beam Gate events, we wish to estimate the beam excess. The number of Beam Gate events n and the number of Pre-Beam Gates events n_0 are assumed to be drawn from Poisson distributions,

$$P(n|y)=\frac{y^n}{n!}e^{-y} \tag{B.1}$$

$$P(n_0|y_0)=\frac{y_0^{n_0}}{n_0!}e^{-y_0} \tag{B.2}$$

with unknown means y and y_0, respectively. The unknown means y and y_0 are related by

$$y = y_1 + \beta y_0 \tag{B.3}$$

where y_1 is the beam excess and β is the ratio of the Beam Gate live time to the Pre-Beam Gate live time. For $n, n_0 \gg 1$, it is standard practice to approximate the Poisson distributions with Gaussian distributions [39]. For Gaussian distributions the estimation of the beam excess $\bar{y}_1$ is equal to

$$\bar{y}_1 = n - \beta n_0 \tag{B.4}$$

and the 68.3% confidence region is defined by

$$n-\beta n_0-\sqrt{n^2+\beta^2 n_0^2}\le y_1\le n-\beta n_0+\sqrt{n^2+\beta^2 n_0^2} \tag{B.5}$$

However, such an approximation is not appropriate when $y, y_0 < 7$ [39], which is the common situation in this experiment.

We employ the method of Helene [86] to estimate the beam excess when the Gaussian approximation is inappropriate. This method uses Bayes theorem [71], which is

$$P(y_1|n,n_0,\beta)=\frac{\int_0^\infty dy_0 P(n,n_0|y_1,y_0,\beta)P(y_1,y_0)}{\int_0^\infty dy_1\int_0^\infty dy_0 P(n,n_0|y_1,y_0,\beta)P(y_1,y_0)} \tag{B.6}$$

where $P(n, n_0|y_1, y_0, \beta)$ is the posterior probability and $P(y_1, y_0)$ is prior probability. Because n and n_0 are observed independently, the posterior probability is simply equal to

$$P(n,n_0|y_1,y_0,\beta)=P(n|y_1,y_0,\beta)\cdot P(n_0|y_0) \tag{B.7}$$

$$=\frac{(y_1+\beta y_0)^n}{n!}e^{-y_1}\frac{y_0^{n_0}}{n_0!}e^{-(1+\beta)y_0} \tag{B.8}$$

The choice of the prior probability is not unique and is a source of controversy. Helene chooses a uniform prior probability $P(y_1, y_0) = 1$. The use of divergent prior probabilities is discussed elsewhere [87]. The estimation of the beam excess $\bar{y}_1$ is equal to

$$\bar{y}_1=\int_0^\infty dy_1 y_1 P(y_1|n,n_0,\beta) \tag{B.9}$$

and 68.3% confidence interval $y_{1lb} \le y_1 \le y_{1ub}$ is defined by

$$0.683=\int_{y_{1lb}}^{y_{1ub}} dy_1 P(y_1|n,n_0,\beta) \tag{B.10}$$

which is solved numerically. Unfortunately, the choice of y_{1lb} is somewhat arbitrary. We choose y_{1lb} so that the quantity $y_{1ub} - y_{1lb}$ is minimum.

Bibliography

[1] S. J. Freedman and J. J. Napolitano (Argonne National Laboratory); B. K. Fujikawa and R. D. McKeown (California Institute of Technology); K. T. Lesko (Lawrence Berkeley Laboratory); R. D. Carlini, J. B. Donahue, G. T. Garvey, and V. D. Sandberg (Los Alamos Meson Physics Facility); W. C. Choi, A. Fazely, R. L. Imlay, and W. J. Metcalf (Louisiana State University); L. S. Durkin, R. W. Harper, T. Y. Ling, J. W. Mitchell, T. A. Romanowski, E. Smith, and M. Trimpot (The Ohio State University).

[2] S. L. Glashow, Nucl. Phys. **22**, 579, (1961).

[3] S. Weinberg, Phys. Rev. Lett. **19**, 1264, (1967).

[4] A. Salam and J. C. Ward, Phys. Rev. Lett. **13**, 168, (1964)
A. Salam, in *Proceedings of the Eight Nobel Symposium*, edited by N. Svartholm, Almqvist and Wiksell, Stockholm, 367, (1968).

[5] E. D. Commins and P. H. Bucksbaum, *Weak Interactions of Leptons and Quarks*, Cambridge University Press, (1983).

[6] R. Bolton, *et al.*, Phys. Rev. Lett. **56**, 2461, (1986).

[7] B. Pontecorvo, Zh. Eksp. Teor. Fiz. **33**, 549, (1957) [Sov. Phys.–JETP **6**, 429, (1958)].

[8] Z. Maki, M. Nakagawa, and S. Sakata, Prog. Theor. Phys. **28**, 870, (1962).

[9] M. Nakagawa, *et al.*, Prog. Theor. Phys. **30**, 727, (1963).

[10] B. Pontecorvo, Zh. Eksp. Teor. Fiz. **53**, 1717, (1967) [Sov. Phys.-JETP **26**, 989, (1967)].

[11] S. Glashow, J. Iliopoulos, and L. Maiani, Phys. Rev. **D2**, 1285, (1970).

[12] G. Danby, *et al.*, Phys. Rev. Lett. **9**, 36, (1962).

[13] B. Kayser, Phys. Rev. **D24**, 110, (1981).

[14] M. Kobayashi and T. Maskawa, Prog. Theor. Phys. **49**, 652, (1973).

[15] J. Bahcall and H. Primakoff, Phys. Rev. **D18**, 3463, (1978).

[16] M. Fritschi, *et al.*, Phys. Lett. **173B**, 485, (1986).

[17] R. Abela, *et al.*, Phys. Lett. **146B**, 431, (1984).

[18] F. Boehm and P. Vogel, *Physics of Massive Neutrinos*, Cambridge University Press, (1987).

[19] S. M. Bilenky and S. T. Petcov, Rev. Mod. Phys. **59**, 671, (1987).

[20] A. Zee, Phys. Lett. **93B**, 389, (1980).

[21] M. A. Beg, *et al.*, Phys. Rev. Lett. **38**, 1252, (1977).

[22] A. Jodidio, *et al.*, Phys. Rev. **D37**, 237(E), (1988)
A. Jodidio, *et al.*, Phys. Rev. **D34**, 1967, (1986).

[23] D. O. Caldwell, *et al.*, Phys. Rev. Lett. **59**, 419, (1987).

[24] P. Fisher, *et al.*, Phys. Lett. **192B**, 460, (1987).

[25] Y. Chikashige, R. N. Mohapatra, and R. D. Peccei, Phys. Lett. **98B**, 265, (1981).

[26] G. B. Gelmini and M. Roncadelli, Phys. Lett. **99B**, 411, (1981).

[27] H. M. Georgi, S. L. Glashow, and S. Nussinov, Nucl. Phys. **B193**, 297, (1981)

[28] R. S. Raghavan, Xiao-Gang He, and S. Pakvasa, Phys. Rev. **D38**, 1317, (1988).

[29] V. Barger, W. Y. Keung, and S. Pakvasa, Phys. Rev. **D25**, 907, (1982).

[30] G. Feinberg and S. Weinberg, Phys. Rev. Lett. **6**, 381, (1961).

[31] E. Derman, Phys. Rev. **D19**, 317, (1979).

[32] S. E. Willis, *et al.*, Phys. Rev. Lett. **44**, 522, (1980)
S. E. Willis, *et al.*, Phys. Rev. Lett. **45**, 1370(E), (1980).

[33] F. Bergsma, *et al.*, Phys. Lett. **122B**, 465, (1983).

[34] D. R. F. Cochran, *et al.*, Phys. Rev. **D6**, 3085, (1972).

[35] M. M. Sternheim, *et al.*, Phys. Rev. **D6**, 3117, (1972).

[36] J. F. Crawford, *et al.*, Phys. Rev. **C22**, 1184, (1980).

[37] Neutrino Facility, *LAMPF Users Handbook*, LAMPF Report MP-DO-3-UHB, (1984), unpublished.

[38] T. Suzuki, *et al.*, Phys. Rev. **C35**, 2212, (1987).

[39] *Review of Particle Properties*, Particle Data Group, Phys. Lett. **204B**, 1, (1988).

[40] R. C. Allen, *et al.*, Phys. Rev. Lett. **55**, 2401, (1985).

[41] S. E. Willis, *et al.*, Phys. Rev. Lett. **44**, 522, (1980)
S. E. Willis, *et al.*, Phys. Rev. Lett. **45**, 1370(E), (1980).

[42] F. Bergsma, *et al.*, Phys. Lett. **122B**, 465, (1983).

[43] B. Kayser, *et al.*, Phys. Lett. **52B**, 385, (1974).

[44] C. M. Hoffman, Phys. Lett. **208B**, 149, (1988).

[45] L. V. Groshev, *et al.*, Nucl. Data Tables **A5**, 1, (1968).

[46] S. J. Freedman, *et al.*, Nucl. Inst. Meth. **215**, 71, (1983).

[47] J. Fitch, *et al.*, Nucl. Inst. Meth. Phys. Res. **226**, 373, (1984).

[48] J. J. Napolitano, *et al.*, Nucl. Inst. Meth. **A274**, 152, (1989).

[49] L. S. Durkin, *et al.*, Nucl. Inst. Meth. **A277**, 386, (1989).

[50] L. Landau, J. Phys. (USSR) **8**, 201, (1944).

[51] H. A. Bethe, Ann. Physik **5**, 325, (1930).

[52] F. Bloch, Z. Physik **81**, 363, (1933).

[53] R. M. Sternheimer and R. F. Peierls, Phys. Rev. **B3**, 3681, (1971).

[54] R. M. Sternheimer, *et al.*, Phys. Rev. **B26**, 6067, (1982).

[55] R. M. Sternheimer, *et al.*, Atomic Data and Nuclear Data Tables **30**, 261, (1984).

[56] J. W. Boldeman, Nucl. Sci. Eng. **55**, 188, (1974).

[57] W. R. Nelson, *et al.*, *The EGS4 Code System*, SLAC Report SLAC-265, (1985), unpublished.

[58] D. I. Garber and R. R. Kinsey, *Neutron Cross Sections, Volume II, Curves*, BNL Report BNL-325, Third Edition, (1976), and references therein.

[59] E. Segrè, *Nuclei and Particles, Second Edition*, p. 496, Benjamin/Cummings Publishing Company, Inc., Reading, Massachusetts, (1977).

[60] L. V. Groshev, *et al.*, *Atlas of $\gamma-$Ray Spectra from Radiative Capture of Thermal Neutrons*, pgs. 139-146, Pergamon Press Ltd., London, (1959).

[61] L. A. Ahrens, *et al.*, Phys. Rev. **D35**, 785, (1987).

[62] L. W. Johnson and R. D. Riess, *Numerical Analysis*, Addison-Wesley Publishing Company, (1977).

[63] J. S. O'Connell, *Proceedings of the Los Alamos Neutrino Workshop June 8-12, 1981*, 43, (1981) unpublished.

[64] T. K. Gaisser and J. S. O'Connell, Phys. Rev. **D34**, 822, (1986).

[65] T. W. Donnelly, Phys. Lett. **43B**, 93, (1973).

[66] E. S. Smith, *Neutrino Backgrounds to Searches for the Appearance of $\bar{\nu}_e$ at LAMPF*, E645 internal memo, unpublished.

[67] B. Kaiser, *et al.*, Phys. Rev. **D20**, 87, (1979).

[68] F. James, Rep. Prog. Phys. **43**, 1145, (1980).

[69] J. B. Donahue, *Alignment for Operations in the LAMPF Beam Stop Area*, LAMPF Report MP-7-TN-21, (1985), unpublished.

[70] J. B. Donahue, private communication.

[71] W. T. Eadie, D. Drijard, F. E. James, M. Roos, and B. Sadoulet, *Statistical Methods in Experimental Physics*, North-Holland Publishing Company, (1971).

[72] P. R. Bevingtion, *Data Reduction and Error Analysis for the Physical Sciences*, McGraw-Hill Book Company, (1969).

[73] L. S. Durkin, *et al.*, Phys. Rev. Lett. **61**, 1811, (1988).

[74] L. A. Ahrens, *et al.* (BNL AGS E734), Phys. Rev. **D31**, 2732, (1985).

[75] C. Angelini, *et al.* (CERN PS BEBC), Phys. Lett. **179B**, 307, (1986).

[76] B. Blumenfeld, *et al.* (BNL AGS E776), Phys. Rev. Lett. **62**, 2237, (1989).

[77] A. M. Cooper, *et al.* (CERN SPS BEBC), Phys. Lett. **112B**, 97, (1982).

[78] V. Zacek, *et al.* (Gösgen), Phys. Lett. **164B**, 193, (1985).

[79] P. Némethy, *et al.*, Phys. Rev. **D20**, 262, (1981).

[80] O. Erriquez, *et al.*, Phys. Lett. **102B**, 73, (1981).

[81] N. J. Baker, *et al.*, Phys. Rev. Lett. **47**, 1576, (1981).

[82] F. Dydak, *et al.*, Phys. Lett. **134B**, 281, (1984).

[83] I. E. Stockdale, *et al.*, Phys. Rev. Lett. **52**, 1384, (1984).

[84] W. C. Louis, *et al.*, *A Proposal to Search for* $\bar{\nu}_\mu \rightarrow \bar{\nu}_e$ *Oscillations with High Sensitivity at LAMPF*, (1989), unpublished.

[85] R. Allen and J. B. Donahue, spokespersons, *Calibration of the Neutrino Flux at the LAMPF Beam Stop*, LAMPF Research Proposal 866, unpublished.

[86] O. Helene, Nucl. Inst. Meth. Phys. Res. **228**, 120, (1984).

[87] H. B. Prosper, Phys. Rev. **D37**, 1153, (1988).